ISSN 1349-6832

JEOL

JEOL NEWS

June 2025
Vol.60
No.1

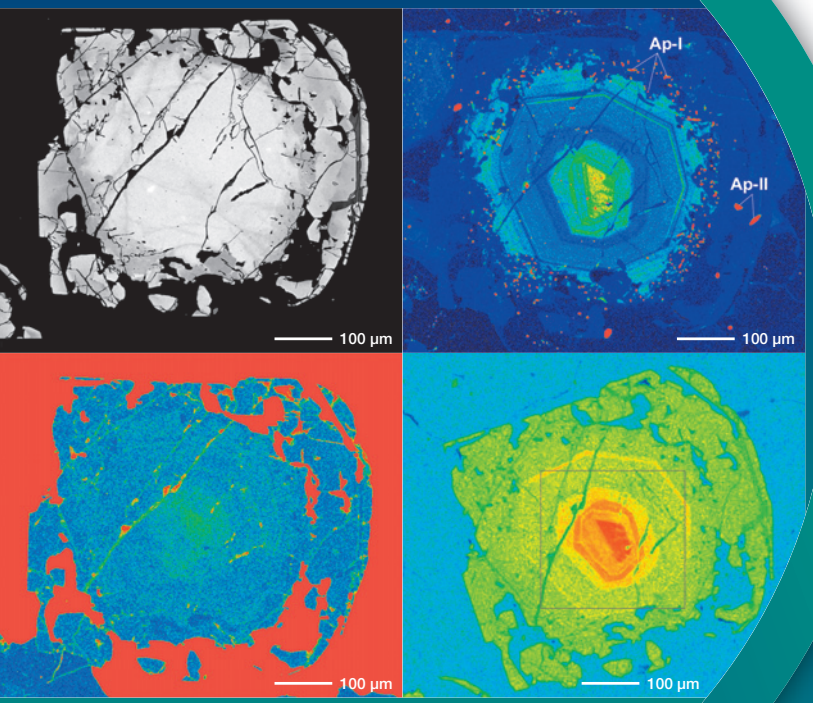

Contents

JEOL NEWS June 2025 Vol.60 No.1

- The Crucial Role of the Electron Microprobe in Solving Micro-Analytical Problems in Earth Sciences and Archaeometry ····· 2
  Jürgen Konzett, Bastian Joachim-Mrosko, Roland Stalder, Peter Tropper, Martina Tribus
  University of Innsbruck, Institute of Mineralogy and Petrography
- Three-Dimensional Digital Structural Analysis of Olfactory Neural Circuits ~ Exploring possibilities of biological analyses by electron microscopy ~ ····· 7
  Kazunori Toida[1, 2] Haruyo Yamanishi[1], Emi Kiyokage[3]
  [1] Department of Anatomy, Kawasaki Medical School
  [2] Research Center for Ultra-High Voltage Electron Microscopy, Osaka University
  [3] Department of Medical Technology, Kawasaki University of Medical Welfare
- Novel Cellular Structures and Physiological Traits of Novel Phyla Bacteria Revealed by Cryo-Electron Microscopy ····· 15
  Taiki Katayama
  Research Institute for Geo-Resources and Environment, National Institute of Advanced Industrial Science and Technology
- X-ray and Electron-Beam Analyses for Teeth of Chiton Accumulating Iron at High Concentrations ····· 20
  Chiya Numako[1], Seiichi Takami[2], Shiori Kamijo[3], Takeshi Otsuka[3], Yusuke Sakuta[3], Shunsuke Asahina[3]
  [1] Chiba University, Graduate School of Science, [2] Nagoya University, Graduate School of Engineering, [3] JEOL Ltd.
- Time-Resolved ESR Method for Observing Rapid Radical Reactions ····· 28
  Atsushi Kajiwara Nara University of Education
- JEM-120i, a 120 kV Transmission Electron Microscope with Compact Appearance and Ease of Use –Its Features and Applications– ····· 37
  Haruka Aoki EM Business Unit, JEOL Ltd.
- Progressing From Easy to Automatic – Overcoming Challenges of Automation with the Latest FE-SEM JSM-IT810 – ····· 41
  Hironobu Niimi, Tatsuro Nagoshi, Noriyuki Inoue EP Business Unit, JEOL Ltd.
- Development of a Large Solid-Angle Windowless EDS Detector "Gather-X" Used with a Field Emission Scanning Electron Microscope (FE-SEM) ····· 46
  Kota Yanagihara EX Business Unit, JEOL Ltd.
- Introduction of the New Cryo-FIB-SEM "CryoLameller" ····· 53
  Rintaro Kawano[1], Wataru Shigeyama[2], Hideki Matsushima[1], Naoki Hosogi[3], Chikako Nakayama[4], Katsuyuki Suzuki[4], Noriaki Mizuno[1]
  [1] EP Business Unit, JEOL Ltd. [2] JEOL USA, Inc. [3] EM Business Unit, JEOL Ltd. [4] Solution Development Center, JEOL Ltd.
- Advancement of Technological Development of an Electron Beam Metal 3D Printer JAM-5200EBM ····· 57
  Masahiko Iida, Ayumi Miyakita, Kozo Koiwa, Nari Tsutagawa, Yohei Daino, Satoshi Ono, Takashi Sato
  IS Business Unit, JEOL Ltd.
- Introduction of JEOL Products ····· 64

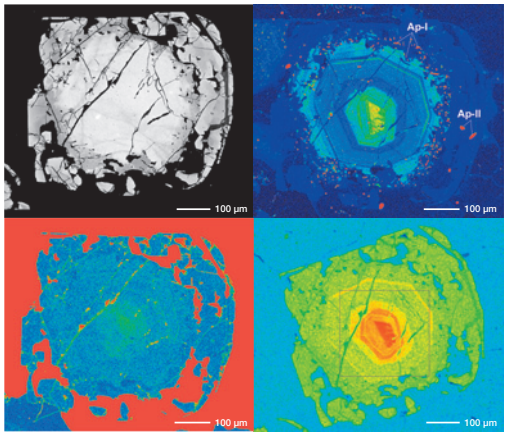

Cover micrograph

Backscattered electron photomicrograph (upper left) and distribution of trace amounts of phosphorus (upper right), sodium (lower left) and tin (lower right), acquired with a JXA-iSP100 electron microprobe, in a garnet crystal from a rare metal-bearing pegmatite emplaced in crystalline basement rocks of the Eastern Alps (Southern Tyrol, Italy). (see page 3)

The Crucial Role of the Electron Microprobe in Solving Micro-Analytical Problems in Earth Sciences and Archaeometry

Jürgen Konzett, Bastian Joachim-Mrosko, Roland Stalder, Peter Tropper, Martina Tribus
University of Innsbruck, Institute of Mineralogy and Petrography

Introduction

The electron microprobe is one of the most important tools for electron optical imaging and chemical analysis of solid phases in Earth and Planetary Sciences. It is also widely applied to solid-state analytical problems in various scientific fields, including materials science and engineering, forensic sciences, solid-state physics and chemistry, archaeometry, and life sciences. Its versatile applicability stems from its unique combination of features, which few, if any, alternative micro-analytical instruments can offer: (1) extremely high spatial resolution for analyses at the micrometer to sub-micrometer scale; (2) the ability to use different analytical modes (WDX-EDX), enabling rapid phase identification as well as quantitative analysis of nearly all natural elements (Be-U) down to concentrations as low as <100 µg/g; (3) the capacity to utilize multiple signals (SE-BSE-CL) to image sample surfaces, allowing the study of solid-phase textures and the detection of compositional zoning in individual grains, also at the micrometer to sub-micrometer scale.

This report summarizes selected studies conducted over the past three years using a JEOL JXA-iSP100 Superprobe at the University of Innsbruck's Institute of Mineralogy and Petrology. These studies encompass diverse topics in mineralogy, geochemistry, and archaeometry, illustrating how the electron microprobe contributes to solving analytical challenges in these research fields.

Anatectic formation of granitic pegmatites in the crystalline basement of the Eastern Alps – evidence from compositional zoning and mineral inclusion patterns of pegmatite garnets

Pegmatites are among the most complex magmatic rocks and have fascinated Earth scientists for centuries due to their exceptionally diverse mineral inventories and the presence of crystals that sometimes reach spectacular sizes. They are not only of scientific interest for understanding melt formation and evolution in the Earth's crust but also hold significant economic value as primary sources of metals such as Li, Be, Nb, Ta, Sn, Sc, and REE, as well as industrial minerals for glass and ceramics manufacturing and colored gemstones.

The genesis of pegmatites is highly complex, involving multiple processes during the crystallization of a pegmatitic parent melt. Early formed magmatic minerals may undergo replacement by late-stage hydrothermal phases, often obscuring the initial formation and evolution of the parent melt. The crystalline basement rocks of the Eastern Alps host numerous granitic pegmatites that formed during a Permian (~240-280 Ma) metamorphic event, some of which exhibit significant Li enrichment of economic importance [1]. Recent studies [2, 3] indicate that these pegmatites have an anatectic origin via partial melting of Al-rich metapelites rather than fractional crystallization from a fertile granitic parent body.

Here, we present electron microprobe data on the compositional zoning of garnet from one of these pegmatites. These data can be used to reconstruct the early evolution of the pegmatite parent melt and further support an anatectic origin. We focus on the zoning of P, Na, and Sn, as these elements are involved in coupled substitutions, significantly reducing their diffusivity compared to elements such as Fe, Mn, Ca, or Mg, which typically undergo homovalent substitutions. P and Sn may also serve as indicators for the degree of pegmatite melt fractionation.

The analyzed garnets exhibit discontinuous zoning in P, Na, and Sn, with high concentrations and pronounced oscillatory zoning in the cores, while the rims have lower concentrations and lack oscillatory zoning (**Figs. 1** and **2**). The P-rich cores show a distinct positive Na-P correlation and feature highly irregular boundaries that, in some cases, discontinuously cut across the oscillatory Na-P zoning (Figs. 1b, c). The garnet rims immediately outside the core-rim boundary contain numerous apatite micro-inclusions forming a halo (Fig. 1b). Some garnets also contain micrometer-sized inclusions in their cores, identified via EDX as Ta-rich columbite and Ta-U-rich pyrochlore-group oxides.

The compositional zoning and inclusion patterns of the garnets suggest the following conclusions.

- Garnet formation started in a melt enriched in Nb, Ta, U and Sn with Nb, Ta and U concentrations high enough to allow crystallization of U-rare metal-bearing oxides, whereas Sn contents were insufficient for cassiterite crystallization.
- Early garnet crystals incorporated high P concentrations, as the melt had not yet reached apatite saturation, making garnet the primary P-storage phase at this stage. Upon reaching apatite saturation during progressive crystallization, P-rich garnet became unstable due to the preferential partitioning of P into apatite and underwent partial resorption. Subsequent

〉〉 Innrain 52f, 6020 Innsbruck, Austria | E-mail: juergen.konzett@uibk.ac.at

garnet growth in the presence of apatite resulted in P-Na poor garnet rims. P re-introduced into the magmatic system in the wake of garnet resorption formed the apatite grains now present as halo enclosed in the garnet rims. This interpretation is consistent with results of high pressure-temperature experiments which show that partial melts formed from likely source rock compositions of the Permian pegmatites are indeed apatite-undersaturated.

- The positive P-Na correlation evident from elemental mappings can be explained by a coupled substitution mechanism: 2 $^{[8]}R^{2+}$ + 3 $^{[4]}Si^{4+}$ = $^{[8]}Na^{+}$ + $^{[8]}vac$ + 3 $^{[4]}P^{5+}$, introducing a vacancy on the eight-coordinated garnet site.

Chemical zonation of phenocrysts in basaltic magmas

Phenocrysts in basaltic melts frequently exhibit distinct chemical zoning, reflecting the evolving composition of the magma during their formation. Additional insights into the formation conditions of phenocryst can be gained through element partitioning between different minerals or mineral and melt, which allows to distinguish phenocrysts (crystals grown from the magma) from xenocrysts (fragments incorporated from surrounding mantle rock) based on compositional homogeneity.

Here, we present analytical results from a volcanic breccia of the Konradfels, one of more than 300 diatremes of the Urach-Kirchheim volcanic area. BSE (back-scattered electron) images (**Fig. 3**) revealed the chemical heterogeneity of olivine, while the chemical composition of olivine phenocrysts (**Fig. 4**), coexisting minerals, and melt was determined using an electron microprobe with an acceleration voltage of 15 kV and a sample current of 10 nA.

Results show documents a strong Fe, Mn, and Ca enrichment toward the rims, with Mg enrichment toward the cores. Based on Mg/Fe ratios and zoning patterns, all analyzed olivines were identified as phenocrysts. Ca and Al incorporation in olivine and co-genetic minerals (clinopyroxene, spinel) suggests genesis conditions of 13-15 kbar and 1,150-1,200 °C.

Fig. 1

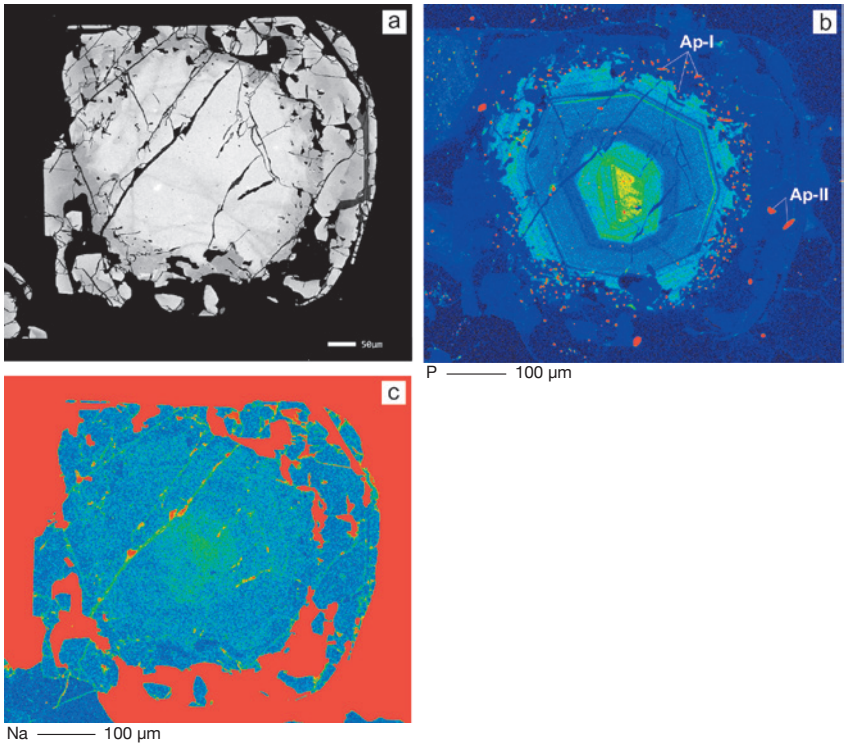

(a) BSE-image and (b)+(c) element distribution maps for P and Na for garnet from a Permian pegmatite of the Eastern Alpine crystalline basement; warm and cold colors denote high and low element concentrations, respectively; note halo of tiny apatite crystals (Ap-I) in (b) along boundary between P-Na-rich core and P-Na-poor rim of the garnet; large apatite grains enclosed in the rim (Ap-II) have formed as a result of apatite-saturation of the melt.

Fig. 2

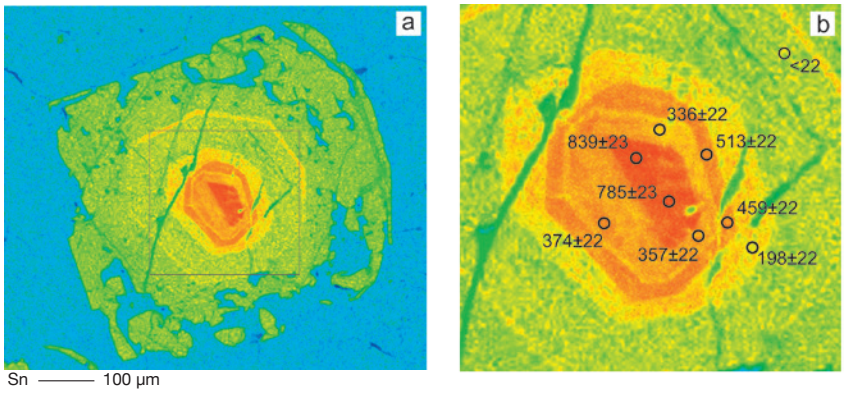

(a) Sn distribution map for garnet shown in Fig. 1; analytical conditions for Sn mapping: 15 kV acceleration voltage; 500 nA beam current; stage drive uni-directional; acquisition of Sn-Lα radiation using PETH crystal; (b) Sn concentrations in garnet within black frame shown in (a); open circles denote locations of analyses; numbers are Sn concentrations in µg/g with 2s-errors; analytical conditions: 15 kV acceleration voltage; 300 nA beam current; Sn-Lα radiation simultaneously acquired with PETH and PETH crystals, using the multi crystal addition mode; counting times for peak and backgrounds of Sn-Lα radiation: 200 sec./100 sec.; detection limit: 20 µg/g; 2σ-errors: 2.7% for 839 µg/g and 11.0% for 198 µg/g; Sn-standard: pure synthetic SnO_2; Sn concentrations calculated from raw counts using PRZ correction and major element composition of garnet previously determined.

Fig. 3

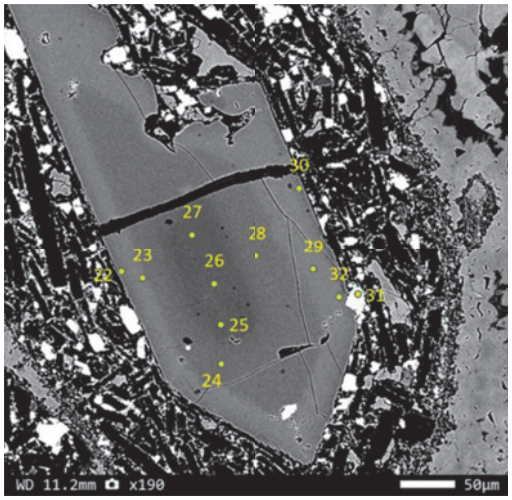

BSE image of a zoned olivine crystal in a matrix consisting of melt, plagioclase, and spinel. The different shades of grey are caused by chemical zonation, with darker colors representing lower average atomic numbers. Numbers in yellow correspond to the analysis spots plotted in Fig. 2.

The effect fluorine on metamorphic and metasomatic reaction dynamics

Understanding the role of fluorine in mineral reactions and microstructural development is crucial for interpreting metamorphic and metasomatic processes. To investigate this, we conducted a series of piston-cylinder experiments in the ternary CaO-MgO-SiO_2 system, growing reaction rims between periclase and wollastonite at controlled pressure-temperature-time (P-T-t) conditions (1.5 GPa, 1273 K, 20 minutes). Full experimental details are provided in [4].

Electron probe microanalysis (EPMA) was employed to determine the phase compositions of both starting materials and all reaction products. Reaction rims were analyzed at 15 kV and 10 nA, while starting materials were analyzed at 15 kV and 50 nA. EPMA calibration was performed using well-established standards. A combination of EPMA data and backscattered electron (BSE) imaging enabled the correlation of phase compositions with textural features. The JEOL JXA-iSP100 microprobe provided exceptionally high resolution, allowing for the interpretation of sub-micrometer structures.

Experimental results demonstrate that fluorine may significantly affect the overall rim thickness, the phase assemblage, and the layer sequence in a reaction rim (**Fig. 5**).

Fig. 4

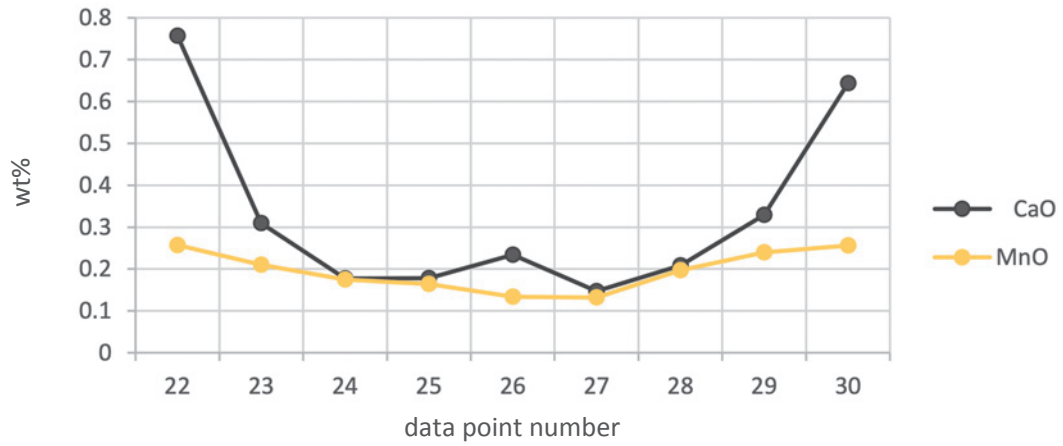

Chemical analyses of spots 22-30 (see Fig. 3) showing the increase of Ca and Mn towards the rim of the crystal.

Fig. 5

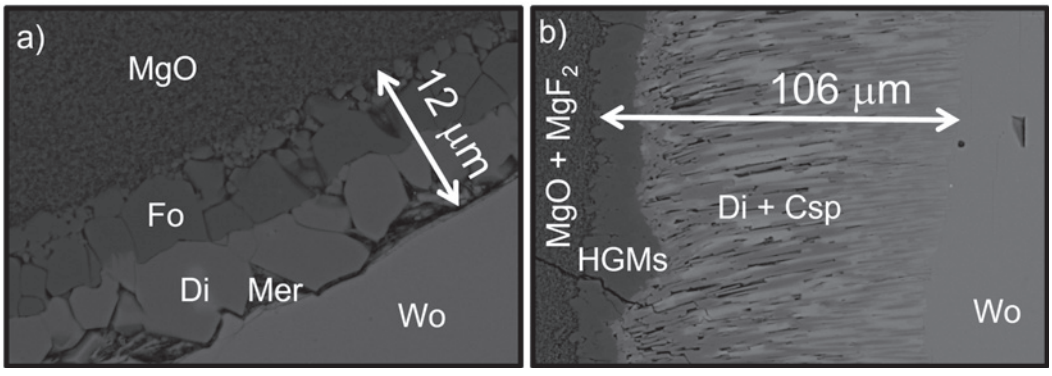

Backscatter electron (BSE) image of reaction rims grown between wollastonite and a) fluorine free MgO and b) MgO+MgF_2 matrix. The bulk fluorine content of the experiment shown in b) was 10 wt% F. All experiments were performed at identical *P-T-t* conditions of 1,000 °C and 1.5 GPa for 20 min. Fo = forsterite, Di = diopside, mer = mewinite, Wo = wollastonite, HGMs = humite group minerals, Csp = cuspidine. Figure is modified after Franke and Joachim-Mrosko (2022).

These effects highlight the challenges of applying existing thermodynamic datasets for phase equilibrium modeling in fluorine-bearing systems. Furthermore, fluorine alters both absolute and relative component mobilities, which are critical for understanding net-transfer reaction dynamics. In this particular example, fluorine enhances MgO mobility across the reaction rim, thus accelerating overall rim growth rates. At high fluorine concentrations (>1 wt% bulk F content), humite-group minerals are stabilized. Additionally, the segregation of diopside ($CaMgSi_2O_6$) and cuspidine ($Ca_8(Si_2O_7)_2F_4$) indicates that fluorine affects relative component mobilities.

Element mapping of a reaction rim from an experiment with 5 wt% F reveals significant fluorine enrichment in the diopside + cuspidine layer and at distinct phase and grain boundaries (**Fig. 6**). This suggests that fluorine strongly influences component mobilities at these boundaries.

These findings underscore the necessity of incorporating fluorine and other volatile components into models reconstructing the P-T-t histories of metamorphic and metasomatic rocks. Moreover, they suggest that reaction rims formed in fluorine-rich environments carry valuable information about their formation conditions. Fluorine-induced variations in rim thickness, layer sequences, relative layer proportions, and microstructures can serve as indirect indicators of fluid composition, even in the absence of direct evidence such as fluid inclusions. Consequently, natural reaction rims hold significant potential as "geofluidometers," providing insights into the chemical properties of metasomatic fluids, particularly in samples where direct fluid evidence has been obliterated. This study highlights the broader significance of investigating fluorine and other volatiles in mineral reaction dynamics to refine our understanding of fluid-mediated processes in metamorphic and metasomatic systems.

Fig. 6

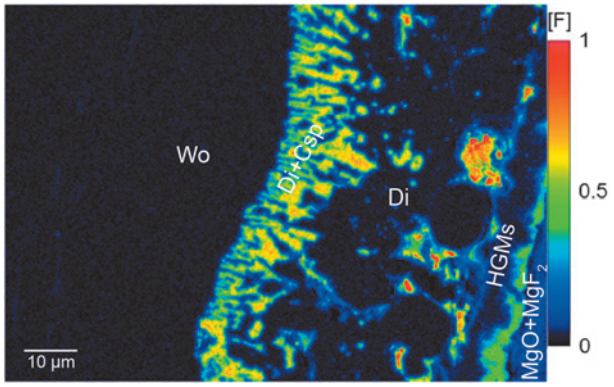

Fluorine distribution across a reaction rim showing a local enrichment in the diopside + cuspidine palisade structure, at selected grain boundaries in the diopside and layer, as well as at the diopside-humite group minerals and the rim-wollastonite interfaces.

Geochemical evidence for prehistoric mining activities: heavy metal distribution in a bone sample from a Bronze Age mining waste heap from Rotholz (lower Inn valley, Tyrol, Austria)

Copper deposits in the Eastern Alps were extensively mined from the Copper Age to the Late Bronze Age. Mining in the Late Bronze Age focused mainly on the fahlore minerals (tennantite-tetrahedrite solid solution). During the Late Bronze Age, mining primarily targeted fahlore minerals (tennantite–tetrahedrite solid solution), as evidenced by numerous mines and metallurgical remains such as furnaces and slag deposits. In addition to smelting residues, organic materials like animal bones and teeth from mining waste dumps provide valuable insight into ore utilization and post-mortem heavy metal mobility within these deposits.

This study examines an animal bone (likely from a goat) recovered from a Late Bronze Age (12th–11th century BC) mining waste heap at the Rotholz copper smelting site (Buch in Tirol) [5]. The bone was analyzed for its chemical and petrographic properties using a polarization microscope and an electron probe microanalyzer (EPMA).

Petrographic investigations reveal a highly porous bone structure, with Haversian canals containing mineralized accumulations clearly visible under both the polarization microscope and in backscattered electron (BSE) images (**Fig. 7**).

EPMA-EDS analyses determined phase compositions, while WDS elemental mapping identified heavy metal alteration phases within the bone. Analyses were conducted at 15 kV and 10 nA. BSE images illustrate the textural relationships between different phases. Elemental maps indicate a pronounced Cu-Sb-As-Mn enrichment along Haversian canals and cavities with variations in grayscale intensity confirming these enrichments (**Fig. 8**).

Fig. 7

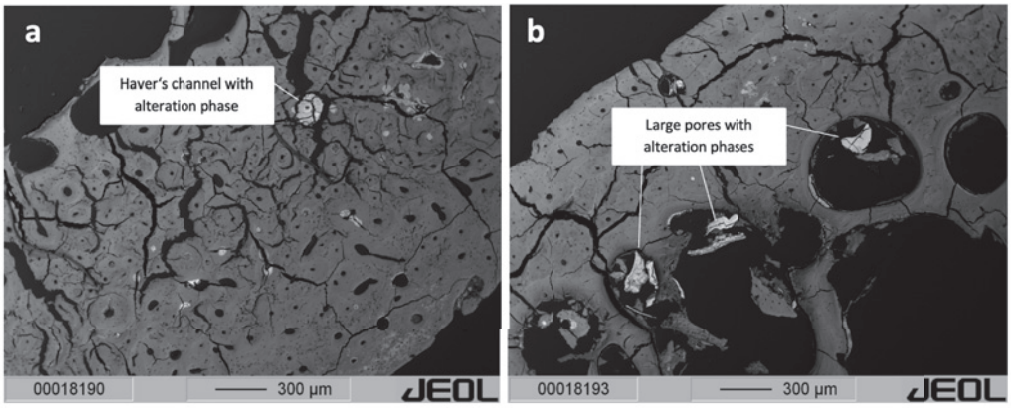

BSE images showing an alteration phase in a Haversian canal (a) and in bone cavities (b).

Fig. 8

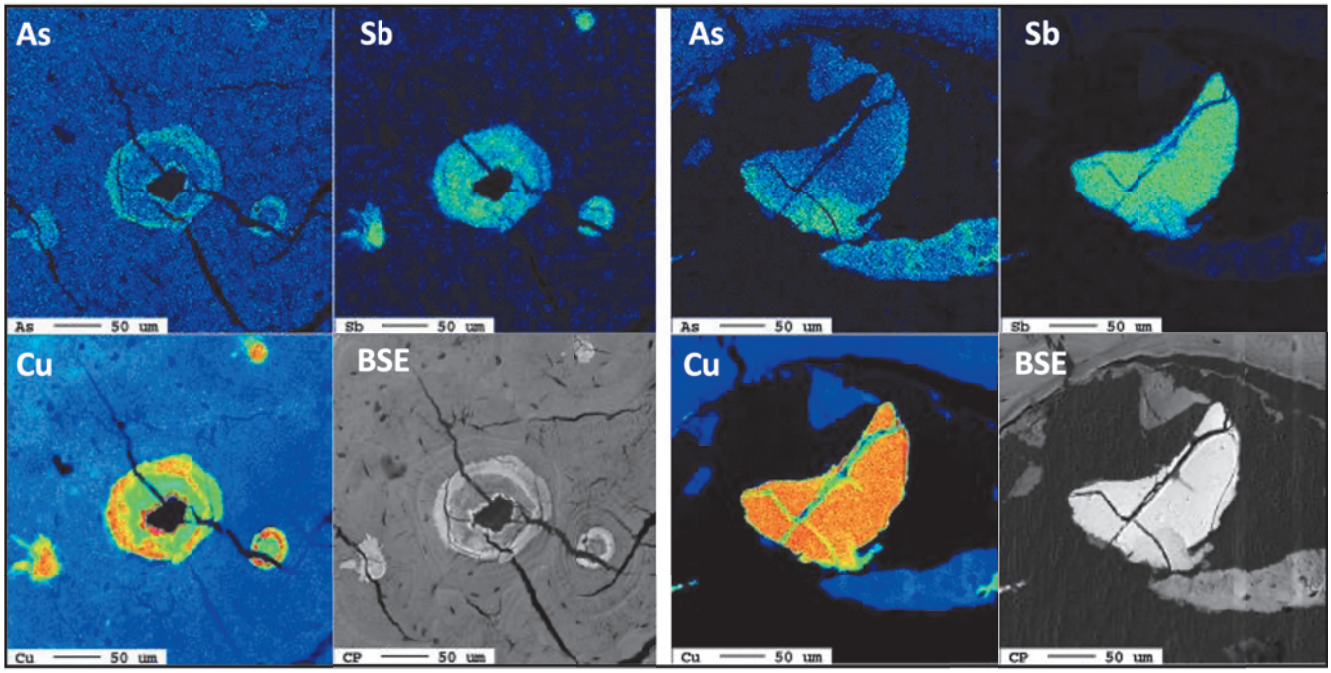

Elemental distribution maps of As, Sb and Cu and backscatter electron (BSE) images of alteration phases growing within the Haversian canals (group of four images left) and bone cavities (group of four images right)

EDS analyses further demonstrate heavy metal incorporation into bone apatite, with arsenic concentrations reaching up to 2 wt.% As_2O_3 and copper up to 20 wt.% Cu_2O. In alteration phases within the Haversian canals, even higher concentrations were measured—up to 50 wt.% Cu_2O and 40 wt.% MnO (Fig. 7a). Antimony (up to 5 wt.% Sb_2O_5) was found exclusively in Cu-Sb-As-rich alteration phases within the bone pores (Fig. 7b).

These heavy metal concentrations are characteristic of fahlore smelting. The elements were incorporated into the bone postmortem, as the remains interacted with metal-enriched pore waters. These solutions either crystallized as alteration deposits in the Haversian canals or were incorporated into the crystal lattice of bone apatite. The enrichment of heavy metals in bone apatite likely resulted from an ion-exchange reaction, where Cu-containing pore waters facilitated the substitution of calcium in hydroxylapatite.

Conclusion

The electron microprobe is an indispensable tool for microchemical analysis and electron optical imaging in Earth Sciences and archaeometry, as it is instrumental in providing data on the composition and textures of geological and anthropogenic materials. In an Earth science context, these data are vital for an in-depth understanding of processes controlling the formation and evolution of magmatic and metamorphic rocks and the distribution of metals in the Earth's interior. Electron microprobe analytical data thus help to secure access to metal resources critical for green technologies. In the context of archeology/archaeometry, electron microprobe data help to reconstruct ancient techniques of metal smelting and processing that expand our knowledge of the technological progress of European Societies and the establishment of trade routes during the Copper and Bronze Age.

Acknowledgments

The authors wish to thank the management of the University of Innsbruck in office in 2020 for speedily and unbureaucratically making available the funds for purchasing the electron microprobe used in this study.

References

[1] R. Göd, "The spodumene deposit at "Weinebene", Koralpe, Austria," *Mineralium Deposita* **24**, 270-278 (1989).

[2] J. Konzett, T. Schneider, L. Nedvalkova, C. Hauzenberger, F. Melcher, A. Gerdes, M. Whitehouse, "Anatectic granitic pegmatites from the Eastern Alps: a case study of variable rare-metal enrichment during high-grade regional metamorphism-I: mineral assemblages, geochemical characteristics and emplacement ages," *The Canadian Mineralogist* **56**, 555-602 (2018).

[3] T. Knoll, B. Huet, R. Schuster, H. Mali, T. Ntaflos, C. Hauzenberger, "Lithium pegmatite of anatectic origin – a case study from the Austroalpine Unit Pegmatite Province (Eastern European Alps): Geological Data and geochemical modeling," *Ore Geology Reviews* **54**, 105298 (2023).

[4] M.G. Franke, B. Joachim-Mrosko, "The effect of fluorine on reaction rim growth dynamics in the ternary CaO-MgO-SiO_2 system," *American Mineralogist* **107**, 1477-1486 (2022).

[5] P. Tropper, D. Leo, G. Degenhart, T. Angerer, M. Staudt, „Schwermetalleinbau in Tierknochen als geochemischer Indikator für die prähistorische Kupferverhüttung: Mineralogische und mikro – Computertomographische Untersuchungen von As-Sb kontaminierten Tierknochen und Tierzähnen," *Metalla Sonderheft* **11**, 86-88 (2021).

Three-Dimensional Digital Structural Analysis of Olfactory Neural Circuits ~ Exploring possibilities of biological analyses by electron microscopy ~

Kazunori Toida[1, 2] Haruyo Yamanishi[1], Emi Kiyokage[3]

[1] Department of Anatomy, Kawasaki Medical School

[2] Research Center for Ultra-High Voltage Electron Microscopy, Osaka University

[3] Department of Medical Technology, Kawasaki University of Medical Welfare

The olfactory bulb, the primary center of the olfactory system, is an attractive model for analyzing the basic brain neural circuit structure due to its neuronal composition containing abundant chemicals in a clear-layered structure. Here we summarize and explain the results of our research on the olfactory bulb, which we have been working on consistently for more than 30 years, and introduce the results by digital electron microscopy (EM) with recent rapid advancement of analysis in newly selective labeling of neurons at the individual animal and genetic levels, and further development of our comprehensive morphological analyses by directly correlated laser and volume EM analyses, which has been established through numerous efforts. Then we would like to discuss the above mainly from a technical perspective and consider the important significance and potential development of EM analysis in the fields of biomedical sciences.

Introduction

We have been conducting integrated structural analyses of the olfactory bulb (OB), the primary olfactory center of the olfactory system in the brain, since 1993, by combining various microscopes, mainly electron microscopes, regarding the OB as a basic structural model for analyzing the brain neural circuit [1]. The OB has anatomical characteristics in which input and output by nerve fibers are clearly distinguished, histological characteristics showing a clear layered structure in which a wide variety of chemical substances are localized in a relatively simple neuronal composition, and phylogenetic characteristics in which these structures are similar across species, making it easy to conduct a variety of experiments under a microscope, including specific tissue and cell staining and physiology and pharmacology. In this article, we at first introduce overall our research results on the OB neural circuit structure by integrated structural analysis from combined laser microscopy and electron microscopy (EM) with serial-sectioning three-dimensional reconstruction, and then provide an overview of recent findings on the structural analyses of various regulatory mechanisms of the olfactory system, which has been accelerated by the improvement of analytical equipment due to the digitalization of EM and the progress of specimen preparation by newly selective labeling of neurons at the animal and genetic levels. Finally, we would like to discuss the technological developments particularly in the EM combined with laser microscopy, that is, directly correlated laser and volume EM analyses, producing these results. In addition, we would be delighted to consider together with the readers the future possibilities for medical and biological applications by EM.

The olfactory bulb as the primary center of olfaction

At the end of the 19th century, Ramon y Cajal of Spain proposed “neuron theory”, which states that the brain is constructed by the connection of independent nerve cells called “neurons” and is no exception to the “cell theory”, and was awarded the Nobel Prize in Physiology or Medicine in 1906. One of the subjects of the silver staining analysis that served as the basis for this theory was the OB (**Fig. 1**). Since then, brain research has focused on elucidating specific functions localized in various areas, while in biology, molecular cell biology has made great strides since elucidating gene structure. Among them, Prof. Axel R. and Dr. Buck L. of Columbia University in the United States were given the Nobel Prize in Physiology or Medicine in 2004 for exhibiting the molecular mechanism of olfactory reception centered on and converge into the OB glomeruli. This brought the olfactory system, an unexplored area of brain function so far, back into the spotlight

〉〉 577 Matsushima, Kurashiki, Okayama, 701-0192, Japan | E-mail: toida@med.kawasaki-m.ac.jp

for the first time in 100 years since Cajal, and triggered many researchers to study the olfactory system, ushering in an era of enlightenment that could be called the "olfactory bulb renaissance" [1-3].

Previous knowledges that a single neuron contains a specific type of transmitter and synaptic morphology classified into two types (excitatory or inhibitory) have been based on classical criterion at the time of neurocytology based on classical silver staining and conventional EM. It has become accepted that odor information is processed in the OB in simple neural circuits organized by relatively small number of neuron types in simpler layers than those in other brain regions, and the molecular mechanism for which the 2004 Nobel Prize in Physiology or Medicine (Prof. Axel R. et al.) was awarded was also based on this simple theory. Under such circumstances, we have continuously demonstrated by multiple immunocytochemical staining using various antibodies that the composition of the OB neurons is more diverse than previously believed [4]. Specifically, using a laser microscope, the OB glomerular interneurons were classified as type 1 or type 2 based on their chemical coexistence [5] and their spatial relationship with the olfactory nerve input [6]. Neurons stained by immunocytochemistry were then used to elucidate the neural circuit configuration with their characteristic synaptic connections using serial-sectioning reconstruction by EM using 50,000 film images and 10,000 digital images taken over a period of earlier eight years (**Fig. 2**) [7-11], resulting in a significant revision of the previously accepted theory (**Fig. 3**) [1, 2].

Digitalization of electron microscopes and new cell labeling ~ Directly Correlative Laser & Volume EM Analyses ~

Considering each area of the brain from the viewpoint of structure and function, they can be broadly divided into three types: input neurons that bring information to the area, output neurons that send information out, and interneurons that remain within the area and are involved in information processing. The existence patterns of the three elements of input, output, and interneurons in each area vary depending on the part of the brain, and clarifying the details becomes a basis of brain research. Input to the OB is the olfactory nerve (ON), and output from the OB is the mitral/tufted cell (M/T), which synapse with each other at the glomerulus in the superficial layer of the OB. The glomerulus, which was determined to be the structural unit of odor discrimination based on the molecular analysis by Axel et al., contains a variety of interneurons, such as GABA-immunopositive and -negative, and is considered to regulate odor reception and transmission (Fig. 3) [2]. On the other hand, input is disturbed by rhinitis allergy, which changes the neural organization and circuit, such as the existence pattern of interneurons [12]. The most notable effect of input deprivation is on tyrosine hydroxylase (TH)-containing neurons. Based on the findings of serial and reciprocal synapses obtained by the author's serial-sectioning EM three-dimensional (3D) reconstruction analysis, TH neurons were thought to be involved in odor discrimination functions such as feed-forward inhibition and

Fig. 1 Mouse brain cross section (C57BL6/J, 10 weeks old)

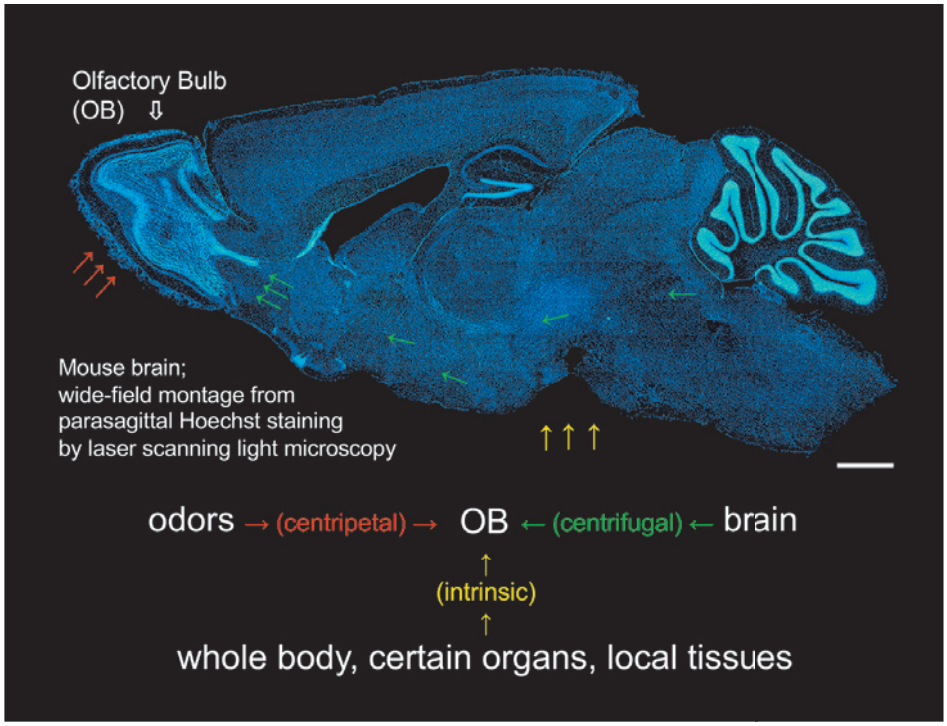

50 μm-thick parasagittal slices were prepared, and a slice 0.9 mm lateral to the midline was stained with Hoechst. The entire area was photographed as a montage using a confocal laser microscope (Carl Zeiss LSM 700) with a 20× objective lens, allowing individual cells to be identified. The bar is 1,000 μm [3]. The olfactory bulb neural circuit is regulated by centripetal inputs (odors; red arrows), centrifugal inputs (projections from other higher brain regions; green arrows), and intrinsic inputs (influences from the whole body, organs, and tissues, such as hormones; green arrows) (see text: [3]).

Fig. 2 Multi-stained laser microscopic images showing the chemical coexistence and mutual proximity of interneurons in the glomerular layer of the olfactory bulb of a rat (Wistar strain, 6 weeks old)

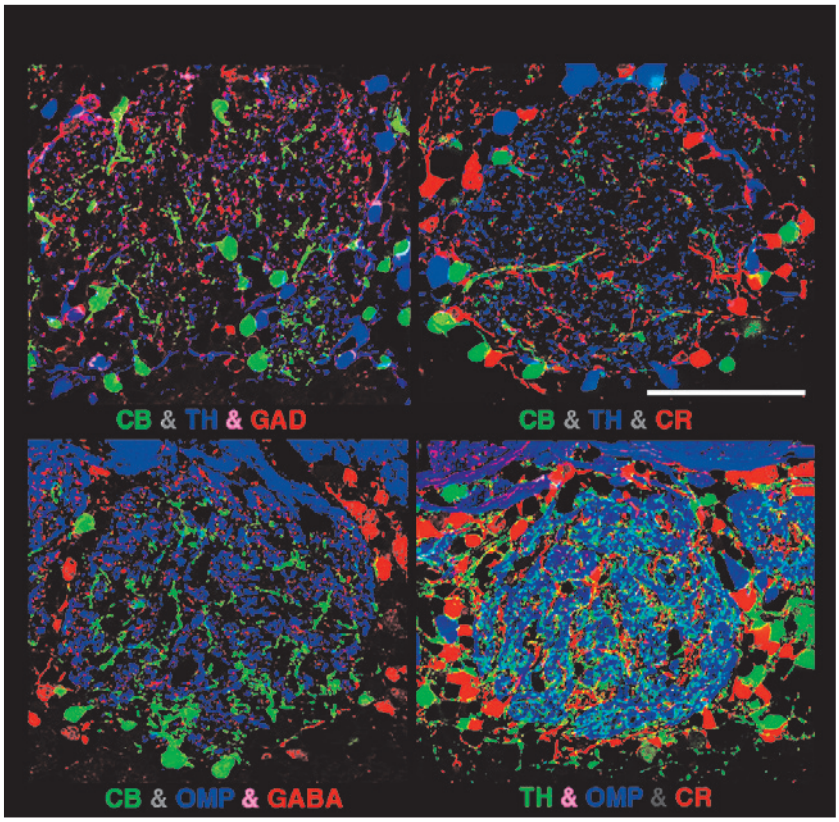

Serial slices 50 μm thick in coronal direction were prepared to show the chemical colocalization (A, B) and their proximity to the olfactory nerve (labeled with OMP olfactory marker protein) (C, D). CB; calbindin and CR; calretinin neurons are independent neuronal groups from TH; tyrosine hydroxylase and GABA neurons (A, B), and are characterized by low proximity to ONs. A-D are the same magnification, Bar is 50 μm [2].

Fig. 3

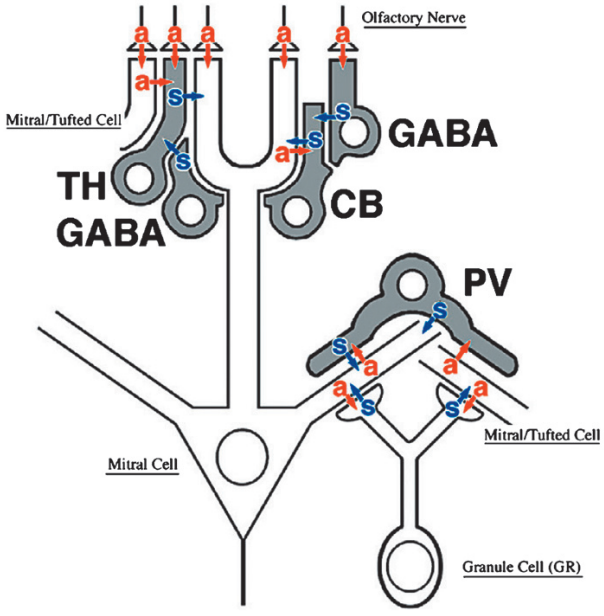

Synaptic neural circuit diagram showed by a schematic diagram of the synaptic neural circuitry of chemically identified neurons, based on electron microscopy analysis of film obtained up until 2004 [2]. PV neuron is a subtype of GABA neurons located in the outer plexiform layer [7, 8]. TH neurons form serial synapses in the glomerular layer, and CB neurons form reciprocal synapses. CB; calbindin, PV: parvalbumin.

lateral inhibition (Fig. 3) [2, 10]. However, the processes of TH neurons are too complex, and film imaging was too limited in its ability to be analyzed all of the synapses on the processes within the glomeruli, which are 50-100 μm in diameter in mice and rats.

In 2009, the authors introduced a new equipment, digital transmission electron microscope (JEOL JEM-1400). This equipment is still in stable operation at present 16 years after its introduction, and the software allows automatic montage photography using a CCD camera. Taking advantage of this performance, we attempted to label TH neurons specifically and record by a laser microscope, and then converted to be stained in order to identify by EM the same neuron, which could be reliably referred to the neuronal images pre-recorded by a laser microscope. We thus could directly correlate the laser microscopic results with serial sectioning-EM 3D-reconstruction [13]. Labeling was performed by genetically modifying TH to label it with GFP, which eliminated the limitations of the staining penetration of immunostaining. Then, the area corresponding to the optical serial sections (200 μm × 200 μm × 50 μm) of the highest resolution oil immersion lens of the laser microscope (× 63 or × 40 magnification × 1.5 optical zoom) was taken with a CCD camera (1K) at a resolution (8.5 nm/pixel) that allows synaptic vesicles and clefts (20 nm) to be identified with certainty. 666 serial sections in total with a thickness of each 75 nm were photographed, with 625 images per section (25 × 25 = 180 μm × 180 μm), for a total of 200,000 images taken every other section (**Fig. 4**). It took 120 minutes per section for montaged image, and three months to complete the entire images (Fig. 3). However, it would take about 20 years to perform a

Fig. 4-1 Correlative Laser & Volume EM Analysis: Correlation between optical and electron microscopic images.

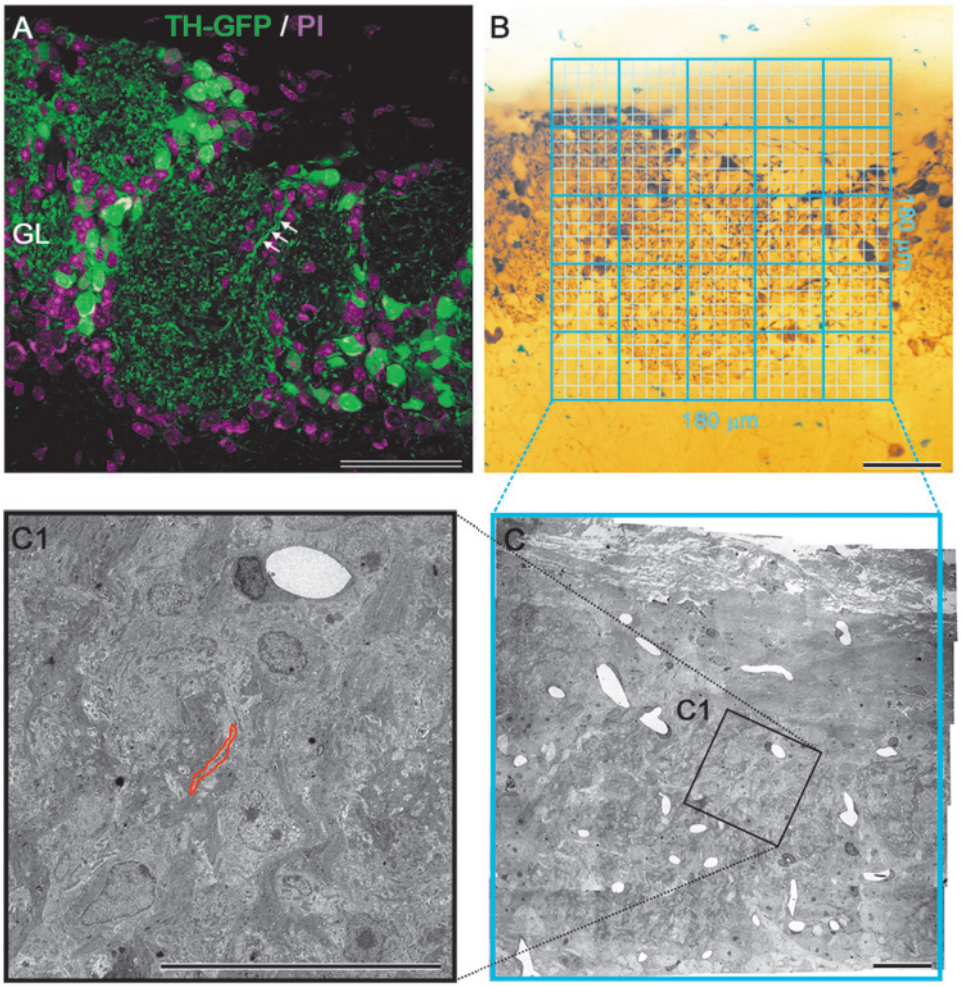

A: PI staining (magenta) of the nucleus of a TH-GFP (green) transgenic mouse. The arrows indicate processes of GFP-positive cells. B: Light microscopy image converted to bright-field labeling with anti-GFP antibody. This corresponds to the laser microscope optical section image in A. A: 25 × 25 blue box covers one glomerulus (approximately 180 µm × 180 µm). C: Auto-montage image by EM corresponds to the light microscopy photograph (B). The lower left panel C1 is an enlargement of C1 in the lower right panel C, and the red outline corresponds to the TH-GFP-positive process indicated by the arrow in A. TH; tyrosine hydroxylase, GFP: green fluorescent protein, GL, glomerular layer. Bar: 50 µm for A and B, 25 µm for C and C1 (reprinted with permission from Fig. 3 in [13]).

Fig. 4-2 Analysis by Directly Correlative Laser & Volume EM: 3D reconstruction of extracted neurons.

Reconstructed image including synapses of a TH-expressing neuron (cell #3) from serial-sectioning EM combined with laser microscopy. Pink indicates asymmetric synapses from the ON terminal to a TH-expressing neuron, red indicates asymmetric synapses from non-ON neurons to a TH-expressing neuron. Light blue indicates symmetric synapses from a GABA neuron to a TH-expressing neuron. A: TH-expressing neuron forms symmetric synapses with other neurons (dark blue). Black and white arrows indicate serial synapses of TH processes. A process of a TH neuron receives an asymmetric synapse from a process of a mitral/tufted (M/T) cell (black arrow) and then forms a symmetric synapse with another M/T cell process (white arrow). This reconstructed neuron appears in the serial sections of the laser microscope in Fig. 4-1A (A-1), and when partially enlarged, it can be seen to correspond to the reconstructed neuron image (A-2). TH; tyrosine hydroxylase. Bars are 25 µm at A1 and 20 µm at A2 (Reprinted with permission from Fig .5 in [13]).

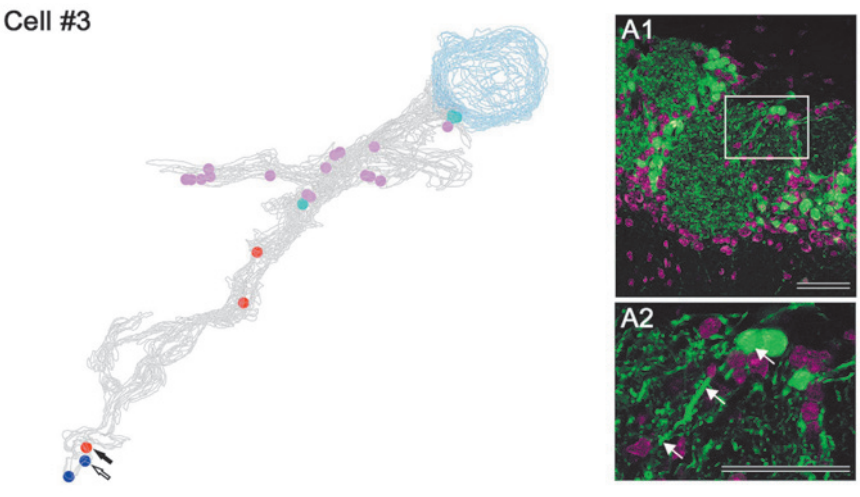

similar analysis on film, so the benefits of digitalization felt by the senior author of us, who experienced the film era, are immeasurable. Initially, automatic montage was performed by manually positioning 5 × 5 montage groups and then expanding the montage, but now it is possible to perform automatic montage over a wider area (see below). This confirmed the senior author's findings in the film era. A similar analysis was also used to analyze the spatial distribution of synapses in neurons whose synapses had not previously been identified [14].

For neurons that were not labeled in immunostaining or genetically modified (transgenic) animals, we used a gene transfer method using a viral vector to analyze single-labeled output neurons (M/T) [15]. Due to the large size of the analyzed neurons, we required several times as many images as for TH neurons, but by using a laser microscope and Neurolucida (MBF Bioscience) tracing images, we were able to more efficiently analyze individual cell locations, such as the cell body and dendrites (**Fig. 5**). In addition, we were able to compare and verify whether synapses identified by EM level on single-labeled neurons by gene transfer were labeled with various synaptic immunostaining markers at the laser microscope level (Fig. 5). Directly Correlative Laser & Volume EM Analyses of structures less than one micrometer in size can only be made reliable with more accurate cell labeling and solid basic EM techniques [15].

Serial block face-scanning electron microscopy (SBF-SEM) and/or focused ion beam-scanning electron microscopy (FIB-SEM) have been recently introduced and developed, which can replace serial-sectioning EM 3D-reconstruction. These new techniques with reliably axial alignment are advantageous for measurements and display of reconstructed images, but have the disadvantage that the sample disappears after observation and analysis. The fact that the sample still exists after imaging allows us to confirm synapses and intracellular fine structures later (see below), and the attractive findings can be obtained with transmitted electrons at higher resolution.

The combination of genetically modified transgenic mice and gene transfer methods using viral vectors enable us to visualize the projection of serotonin [16], acetylcholine [17], noradrenaline [18], and histamine [19] neurons from other brain regions to the OB, suggesting that olfactory information is regulated by other brain functions such as arousal, learning and memory, gaze, and hypothalamic function, and therefore providing a reliable guide for future functional analyses.

Furthermore, double immuno-EM analysis combined with a laser microscope revealed for the first time the interesting finding that estradiol increased the expression of TH, the inhibitory transmitter GABA synaptic marker, and the number of synapses in the TH neurons, which are involved in odor discrimination, revealing the possible role of female hormones in regulating odor discrimination in TH neurons (**Fig. 6**) [20].

By directly correlating laser microscopy with EM and further accumulating applications of basic EM techniques, it has become clear that the olfactory neural circuits may have at least three different types of intrinsic regulatory mechanisms:

Fig. 5 Correlative Laser & Volume EM analysis: Single labeled neuron by gene transfer.

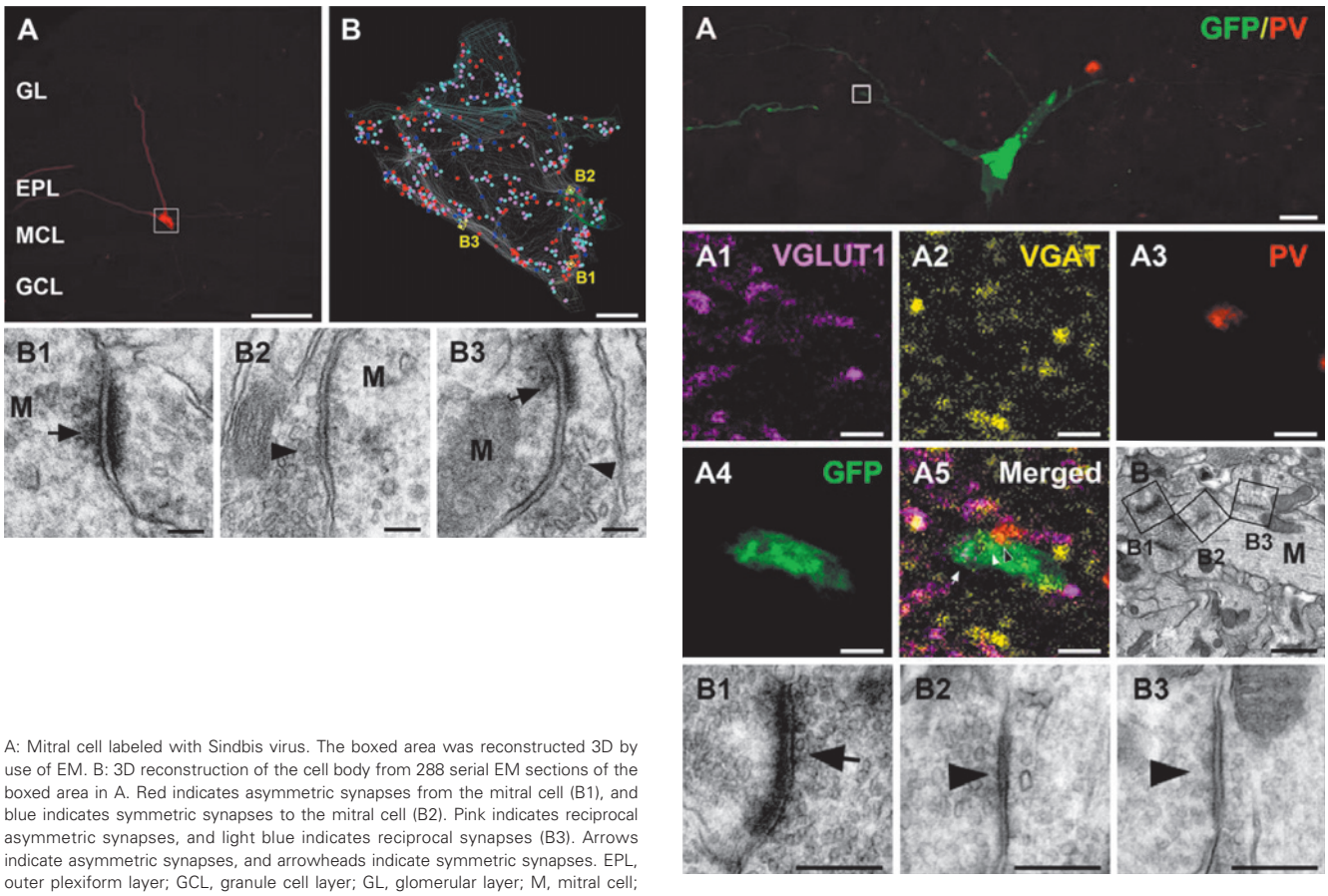

A: Mitral cell labeled with Sindbis virus. The boxed area was reconstructed 3D by use of EM. B: 3D reconstruction of the cell body from 288 serial EM sections of the boxed area in A. Red indicates asymmetric synapses from the mitral cell (B1), and blue indicates symmetric synapses to the mitral cell (B2). Pink indicates reciprocal asymmetric synapses, and light blue indicates reciprocal synapses (B3). Arrows indicate asymmetric synapses, and arrowheads indicate symmetric synapses. EPL, outer plexiform layer; GCL, granule cell layer; GL, glomerular layer; M, mitral cell; MCL, mitral cell layer. Bars: 100 μm (A), 5 μm (B), 100 nm (B1-B3) (reproduced with permission from Fig. 3 in [15]).

1) afferent regulation by odor input, 2) centrifugal regulation by higher brain regions, and 3) endogenous regulation by the internal environment. These findings are summarized in Fig. 1.

Biomedical applications of digital electron microscopy: electron tomography and full-range montage

Once performing serial-sectioning EM 3D-reconstruction and wide-field montage analysis using new cell labeling, images of synapse morphology that do not fit conventional classifications such as "type 1 or type 2", "symmetric or asymmetric", and "spherical or flat vesicles" are captured. Therefore, we performed electron tomography analysis by taking serially tilted images of ultrathin sections with a standard thickness of about 70 nm (JEM-1400). As a result, the criteria for synapse identification, such as synapses formed by neurons projected from other brain regions and TH neurons influenced by estradiol, become more diverse, including synaptic vesicles, synaptic clefts, and postsynaptic membrane thickening (**Fig. 7**). The functional significance of these findings has been currently analyzed, but if structure and function are mutually correlated and structure changes well in a plastic manner due to function, future analyses will be even more exciting.

Electron tomography of biological ultra-thin sections can be performed not only at the synapse structure (magnification of 10,000 to 20,000 times) but also at the cell membrane and organelle level (magnification of 50,000 to 100,000 times). However, we feel that this also requires basic technical knowledge and constant practice in staining, specimen preparation, and maintenance of electron microscope as equipment.

Wide-field montage using electron microscopes are essential for Directly Correlative Laser & Volume EM Analyses. Recently, a software function called Limitless Panorama (LLP) was started on the electron microscopes (JEM-1400 and JEOL JEM-1400Flash) that we use, which has made it possible to perform full-area automatic montages. As an example, we photographed an area (**Fig. 8**A) that corresponds to an image taken with a wide-area, high-resolution oil immersion lens (40 × objective, further reduced digital magnification) of a laser microscope with a 3K camera (JEM-1400Flash; magnification ×6,000), which has a resolution that allows more detailed synaptic images to be obtained than in the analysis of TH neurons mentioned above. The stitching of the montage images by EM is relatively good, and in fact the 100 × 100 montage images taken over three consecutive days of operation look like a single ultra-low magnification image overall (Fig. 8B). However, when enlarged on a PC, the synapse image can be confirmed (Fig. 8C). This is like a map on a PC, and once the image is taken, the image can be checked at leisure later. Even with the same type of electron microscope, the CCD camera of the Kawasaki Medical School equipment (JEM-1400) is 1K, so by simple calculation, it would take nine times as many shots to obtain the same data as that obtained with the latest equipment (JEM-1400Flash) at the Osaka University Research Center for Ultra-High Voltage Electron Microscopy, which has a 3K resolution CCD camera. We feel that a rapid progress is remarkable. This analysis is usually performed for electron micrography, where "the electron microscope to observer photographer = one-to-one", but now

Fig. 6 Confirmation of localization of vesicular GABA transporter (VGAT)-immunoreactivity using correlated laser & volume EM and serial section double immunoelectron microscopy.

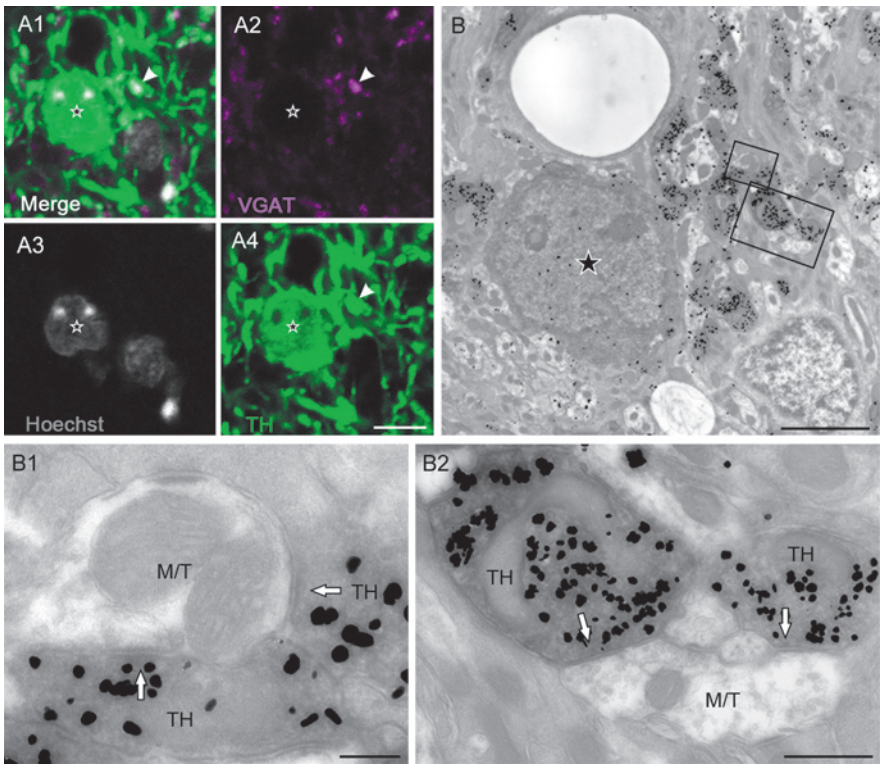

A1-A4: Immunofluorescent staining for TH (green), VGAT (magenta), and Hoechst (nuclei, grey). White arrows indicate colocalization of TH and VGAT. Each star indicates the same TH neuron in A and B. B: Electron microscopy images correspond to laser microscopy images (a). B1 and B2 are high magnification images of the boxed area in B. VGAT immunoreactivity is labeled with gold particles, and TH immunoreactivity with 3, 3'-diaminobenzidine tetrahydrochloride(DAB). TH-labeled neurons form symmetric synapses onto unlabeled mitral/tufted (M/T) cell dendrites (white arrows). TH; tyrosine hydroxylase. Bars: 5 μm in A4, 2 μm in B, 200 nm in B1, and 500 nm in (B2) (reproduced with permission from Fig. 9 in [20]).

Fig. 7 Electron tomography analysis of acetylcholine neuron synapses.

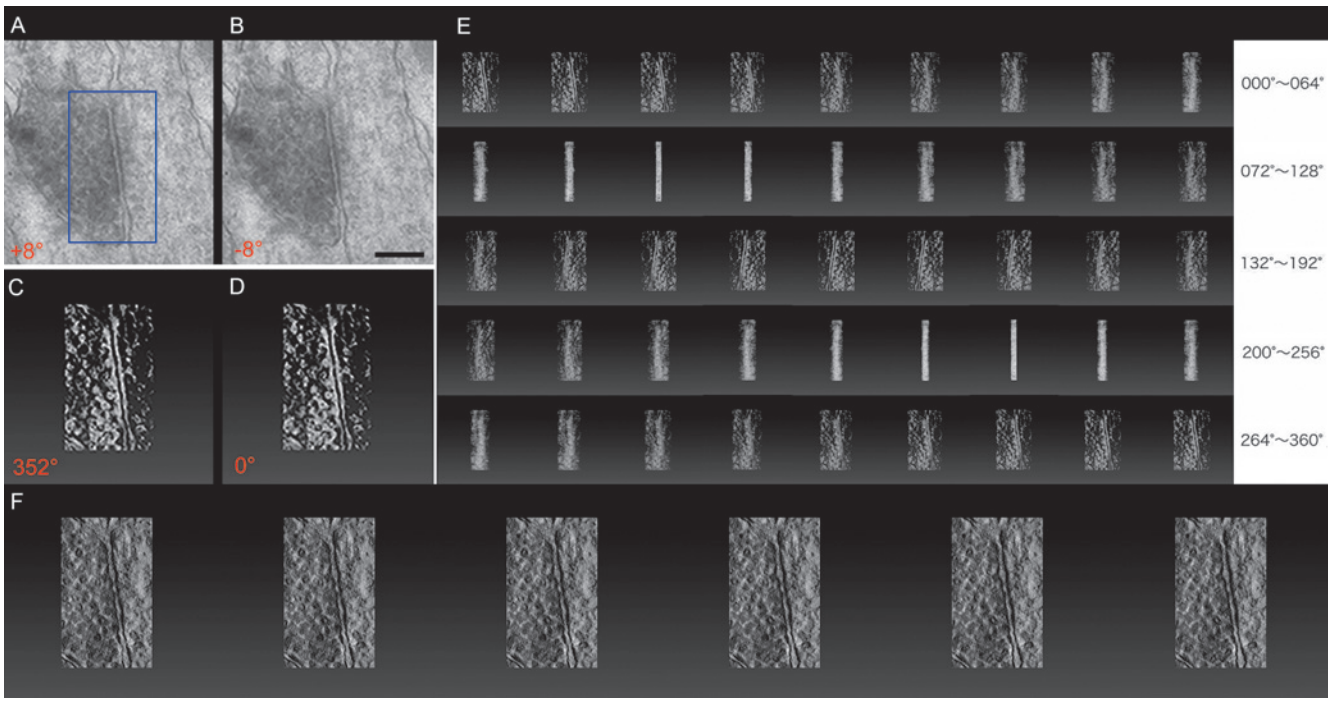

A and B are photomicrographs of synapses of acetylcholine neurons in the mouse olfactory bulb, taken by immuno-EM.
A and B are stereo images of (±8°; anti-vesicular acetylcholine transporter antibody). The composite photographs in C and D show a synapse reconstructed by tomography (corresponding to the square area in A). The bar is 0.2 µm. E shows a 3D reconstructed rotational image by tomography. The square area in A and B was photographed in 1° increments in the ±8° direction, and a 3D tomography image was reconstructed from these images, from which a ±0° to ±360° tomography image was generated. A total of 45 images are shown, in 8° increments, from a total of 360 reconstructed images. Since the tomographic reconstruction is 3D voxel data, it is possible to reproduce 360° rotational videos, which deepens understanding. It is possible to view in 1° increments from directions that would not normally be observable. The slices A and B, which are actually 80 nm thick, are converted and accumulated by tomography to reconstruct six ultrathin slice-like cross-sectional images from the voxel data, which are calculated to be in 2 nm increments, and fine morphology such as cross-sectional images of synaptic vesicles with a diameter of about 20 nm that cannot be seen in the original slice images (A and B) can be observed (F). Careful specimen preparation and instrument operation are required [17, 21].

Fig. 8 Correlated Laser & Volume EM Analysis: Wide-field Montage.

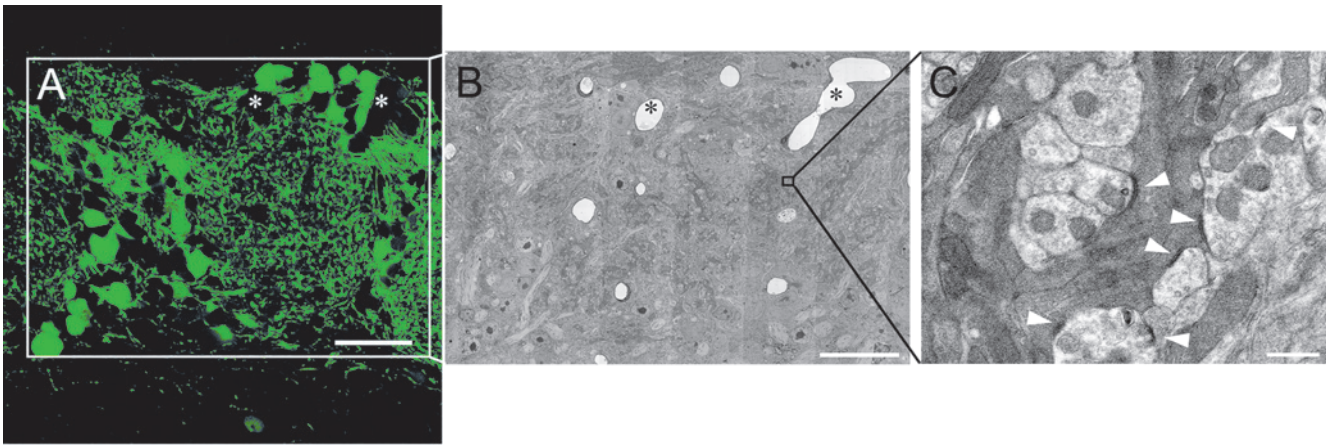

A: The analysis area of TH neurons of TH-GFP mice observed with a laser microscope at 40× objective (scan zoom ×0.8) is 200.05 µm × 200.05 µm. B: To analyze the same tissue slice with an electron microscope at a resolution that allows synapse identification, analysis must be performed at a minimum of ×6,000 (3,312 pixels × 3,312 pixels, 0.75 nm/pixel). This requires a total of 10,856 images (approximately 100 images ×100 images: 84.5 GB) taken over 13 hours. A portion of these images corresponding to the laser microscope image (A) has been cropped. C: A synapse image is confirmed in one of the images. Bar: 20 µm (A, B), 100 nm (C); Original electron micrographs by one of us, Dr. Haruyo Yamanishi, taken at Osaka University Center for Ultra-High Voltage Electron Microscopy (JEM-1400Flash).

we are in an era of "one-to-many," or "virtual-multiple-to-real", so-called "virtual electron microscopes." In addition, Directly Correlative Laser & Volume EM Analyses, which directly corresponds to and observes a wide area that can be analyzed with a laser microscope image with a high resolution that cannot be analyzed with a laser microscope, enables more reliable analysis of the localization, distribution, and quantification of intracellular organelles and synapses, and by patiently and carefully repeating bidirectional corresponding observations (differential ⇄ integral) between microscopic (finer) and macroscopic (wider), it leads to a deeper understanding of the structure of living organisms [13-15, 20].

In addition to the recent digitalization, the spread of social networks by internet and technological innovation led the authors to establish the "Network Tele-Microscopy Research Group" at The Japanese Society of Microscopy, which applies networks, and hold a number of study meetings. (http://www.uhvem.osaka-u.ac.jp/network_tele-microscopy_jsm/archive.pdf) Rapidly developing network technology has made it possible to remotely check the status of the wide-area montage (Fig. 8) taken over three days using not only a PC but also a cellphone, making it possible to carry out a variety of multidimensionally temporal & spatial analyses that allow multiple people to participate in the same image at different times and in different locations. The analysis that was once ideal goal has become a reality, and we are seeing even more unexpected developments. As such, we are very much looking forward to the development of future research, as electron microscope analysis will continue to develop and diversify in the future.

Conclusion

As described above, we have looked back overall on my research to date, focusing on the findings obtained using the digital EM we have used in the last 15 years. We hope this will be of use to the reader. Electron microscopes can be used as critically precise analyses in physics and material engineering, but we feel that the application of this high-performance equipment to biomedical sciences still holds unlimited possibilities that exceed our expectations so far. It has been 45 years since one of authors first experienced electron microscope observations when he was a second-grade student at the medical school in 1980, but what still fascinates him and other authors is the "beautiful image of life" or "Beauty is Truth". We have felt this in optical microscopes, physiological experiments, and even math formula & statistical analysis results. In the future, from now on, we will continue to work with our colleagues and collaborators to obtain more elegant and sometimes greedy analysis results in order to obtain more beautiful results than in the past, or even yesterday. We believe sophisticated EM, spending hard but very enjoyable days, would be able to withstand the winds and snows even unexpectedly caused from technological innovation that accompanies the times in the future.

Acknowledgments

The above research was started with the guidance of Professor Yasuo Uehara (Ehime University, Kumamoto University), Professor Toshio Kosaka (Kyushu University), and Professor Kiyoshi Hama (Institute of Physiological Sciences, University of Tokyo), and was supported by Professor Katsuko Kosaka (Kyushu University, International University of Health and Welfare), Assistant Professor Sawa Horie (National Defense Medical College), Assistant Professor Keita Sato, Assistant Professor Eiji Nozu, and Technical Staff Nobuaki Matsuda (all from the Department of Anatomy, Kawasaki Medical School), and I have been working with former graduate students; Dr. Yoshinori Suzuki (Lecturer, Plastic Surgery), Dr. Shinichi Hamamoto (Lecturer, Otorhinolaryngology, Head and Neck Surgery), Dr. Takeshi Matsuno (Lecturer, Pathology), Dr. Yukari Minami (Lecturer, Neurosurgery), and Dr. Shinya Ozaki (Otorhinolaryngology, Nagoya City University); and outside the university, with Professor Kaoru Mitsuoka, Specially Appointed Professor Satoshi Ichikawa, Technical Staff Tetsuya Yasuda, Technical Staff Atsuko Saito (all from Osaka University), Professor Takeshi Kaneko (Kyoto University), and Professor Hiroyuki Hioki (Juntendo University). I was also taught the basic techniques of operating a transmission electron microscope by Mr. Muneji Nagata (JEOL) 25 years ago at the time of post-doctoral training supervised by Professor Uehara. I would like to thanks all the people who have helped me with expressing my deep gratitude.

This research was supported by grants from the Japan Society for the Promotion of Science (KAKENHI; 24K09664, 19K06932, 15K06748, 24500418, 23500419, 19500295, 15500239, 11680741, 08780730, 06044237), a subsidy for the improvement of facilities at private schools, and a research grant from the Kazato Research Foundation, for which we would like to express our gratitude.

References

[1] Toida K. *Anatomical Science International*, **83**; 207-217 (2008).
[2] Toida K., Kenbikyo, **40**; 20-26 (2005).
[3] Toida K. et al *Clinical Neuroscience*, **34**; 1312-1315 (2016).
[4] Kosaka K. et.al. *Neuroscience Research*, **30**; 101-110 (1998).
[5] Kosaka K. et al. *Neuroscience Research*, **23**; 73-88 (1995).
[6] Kosaka K. et al. *Neuroscience*, **76**; 775-786 (1997).
[7] Toida K. et al. *Brain Research*, **650**; 347-352 (1994).
[8] Toida K. et.al. *Neuroscience*, **72**; 449-466 (1996).
[9] Toida K. et.al. *Journal of Comparative Neurology*, **392**; 179-198 (1998).
[10] Toida K. et.al. *Neuroscience*, **101**; 11-17 (2000).
[11] Toida K. et.al. *Advance in Behavioral Biology*, vol. **53**; 289-292 (2002).
[12] Ozaki S, et al. *Auris Nasus Larynx*, **37**; 575-583 (2010).
[13] Kiyokage E. et al. *Journal of Comparative Neurology* **525**; 1059-1074 (2017).
[14] Notsu E, et al. *Microscopy*, **68**; 316-329 (2019).
[15] Matsuno T, et al. *Journal of Comparative Neurology* **525**; 1633-1648 (2017).
[16] Suzuki Y, et al. *Journal of Comparative Neurology* **523**; 262–280 (2015).
[17] Hamamoto M, et al. *Journal of Comparative Neurology* **525**; 574-591 (2017).
[18] Horie S, et al. *Journal of Comparative Neurology* **529**; 2189-2208 (2021).
[19] Minami-Ogawa Y et al. *Journal of Comparative Neurology* **532**; 1-13 (2024).
[20] Kiyokage E et al. *Journal of Comparative Neurology* **531**; 528-547 (2023).
[21] Toida K. and Kiyokage E. *Clinical Neuroscience*, **38** (1) to (12) (2020). "Series: Invitation to Stereology"
The corresponding author of this paper is also the corresponding author of all papers listed above except for [4-6] and [12].

Novel Cellular Structures and Physiological Traits of Novel Phyla Bacteria Revealed by Cryo-Electron Microscopy

Taiki Katayama
Research Institute for Geo-Resources and Environment, National Institute of Advanced Industrial Science and Technology

In bacterial taxonomy, "phylum" represents the highest hierarchical rank. More than 100 uncultivated phyla of bacteria may live on Earth, for which no representatives have been characterized. Recently, we have successfully cultured two bacteria of novel phyla from natural gas reservoirs, deep subsurface environments. Interestingly, these bacteria exhibit unique characteristics that challenge conventional prokaryotic paradigms. One possesses an intracellular membrane that surrounds its genomic DNA, while the other relies on other bacterial species for the synthesis of its essential cell wall components. This article introduces the research journey of these strains of novel bacterial phyla, with a particular focus on their structural and physiological characteristics as elucidated by cryo-electron microscopy.

Introduction

Microscopy has continuously evolved as an indispensable tool for uncovering the hidden world of microorganisms—specifically, bacteria and archaea—that are invisible to the naked eye. Early studies focused on observing cell morphology and motility using optical microscopy. Over time, microscopy techniques expanded to include fluorescence and non-fluorescent staining methods, allowing researchers to track the localization and dynamics of specific biomolecules, ultimately contributing to our understanding of cellular functions. Furthermore, electron microscopy has played a crucial role in microbiology by enabling the detailed observation of microbial ultrastructure. In recent years, cryo-electron microscopy (Cryo-EM) has also gained increasing attention in microbiological research. Unlike traditional chemical fixation techniques, Cryo-EM involves rapid freezing of samples in vitreous ice, preserving them in a near-native state for imaging. Additionally, by capturing images while continuously tilting the specimen, Cryo-EM enables three-dimensional reconstruction, making it a powerful tool for structural analysis of microbial cells and macromolecular components.

Leveraging the unique advantages of Cryo-EM, we have investigated novel microbial species isolated from environmental samples. In this article, we focus on two particularly intriguing novel bacteria: *Atribacter laminatus* RT761, which possesses an intracellular membrane surrounding its genomic DNA [1], and *Fidelibacter multiformis* IA91, which lacks the ability to synthesize its own cell wall and depends on other species for survival [2]. We discuss the research background, Cryo-EM-based observations, and newly acquired insights regarding these organisms. Notably, these findings were selected as highlights in the respective academic journals where they were published [3], and the discovery of RT761 has also been featured in high school biology textbooks.

Culturing unknown microorganisms in deep subsurface environments

To understand the characteristics of microorganisms, it is essential to obtain pure cultures and cultivate them under controlled conditions. However, the majority of microorganisms inhabiting Earth's environments remain uncultivable by conventional laboratory techniques. When analyzing microbial genes directly from environmental samples, numerous gene sequences distinct from those of known species are detected. Based on the highest taxonomic rank, the phylum, prokaryotic life on Earth is estimated to consist of approximately 200 phyla [4]. However, less than 30% of these phyla contain cultured representatives, while the vast majority are only known from genetic sequences and remain uncultured. Cultivating and characterizing these unknown and uncultured microorganisms is fundamental to understanding the roles of environmental microbes and contributes to the conservation of Earth's ecosystems and the sustainable utilization of natural resources. In particular, the cultivation of novel, high-rank uncultured microorganisms are of great significance, as they are evolutionarily distant from known microbes and may exhibit entirely novel biological traits.

Our research has focused on microbial communities in subsurface environments, particularly those involved in natural gas formation. Methane, the primary component of natural gas, is considered to originate from either thermal or microbial degradation of organic matter in marine sediments. Notably, methane hydrate deposits in Japanese coastal waters and recently discovered gas reservoirs in the Eastern Mediterranean

〉〉 Higashi 1-1-1, Tsukuba 305-8567, Japan | E-mail: katayama.t@aist.go.jp

and offshore Myanmar are all considered to be of microbial origin, drawing significant attention. Thus, elucidating microbial ecology in subsurface sedimentary environments is directly linked to optimizing natural gas resource utilization and accurately assessing gas reserves. Additionally, the subsurface harbors a diverse array of uncultured microorganisms, making it a promising site for the discovery of novel microbial resources. The Minami-Kanto Gas Field in Chiba Prefecture contains vast reserves of microbially produced methane, which has been sustaining local energy needs as a natural gas resource. Given its importance, we have undertaken efforts to culture and isolate previously uncultivated microorganisms from this environment. As a result, we successfully isolated *Atribacter laminatus* strain RT761 and *Fidelibacter multiformis* strain IA91 from sediment and formation water samples of the Minami-Kanto Gas Field. Each of these strains was obtained as a pure culture over a period of 3 and 4 years, respectively, despite the immense microbial diversity present in environmental samples, which contain tens of thousands of microbial species.

Discovery of the novel phylum bacterium *Atribacter laminatus* RT761 that possesses an intracellular membrane enclosing genomic DNA

The group to which strain RT761 belongs had previously been detected as DNA sequences in anaerobic environments such as deep-sea sediments, hot springs, oil fields, and methane fermentation tanks. In particular, this group has been recognized as a dominant population in deep subseafloor sediments associated with methane hydrate deposits, drawing attention for its ecological role in methane formation [5]. On the other hand, this group is highly novel from a taxonomic perspective and has been classified as a new phylum, necessitating further investigation of its biological characteristics.

When examining novel bacterial species under a microscope, it is standard practice to analyze cell morphology, membrane structures, morphological changes during the growth cycle, and the presence or absence of endospore formation. Optical microscopy of strain RT761 revealed an unusual feature: unlike typical bacteria, its genomic DNA was not dispersed throughout the cell but was instead localized in the central region (**Fig. 1**). Cryo-electron microscopy (Cryo-EM, JEOL CRYO ARM™ 300) provided a clear explanation for this observation. In addition to possessing an outer membrane and cytoplasmic membrane similar to Gram-negative bacteria, RT761 cells contained an additional intracellular membrane (**Fig. 2**). Fluorescence staining microscopy confirmed that this intracellular membrane enclosed the genomic DNA (**Fig. 3**). While structurally distinct from the nuclear membrane of eukaryotic cells, these findings indicate that RT761 possesses a unique feature not found in prokaryotes. A three-dimensional reconstruction of RT761 cells using cryo-electron tomography revealed the presence of ribosome-like particles (20–30 nm in size) not only in the cytoplasm enclosed by the intracellular membrane (i.e., the same space as the genomic DNA) but

Fig. 1 Cells and genomic DNA of *A. laminatus* strain RT761.

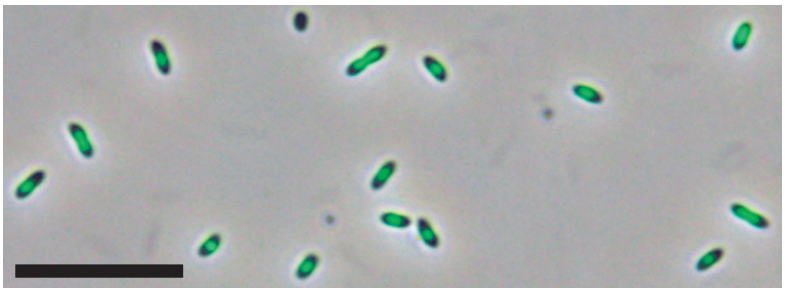

Nucleic acids were stained with SYBR Green and observed using a light microscope. While prokaryotic cells are generally stained uniformly, in strain RT761, genomic DNA remains localized at all cell division phases. (Bar, 10 μm)

Fig. 2 Cellular structure of strain RT761.

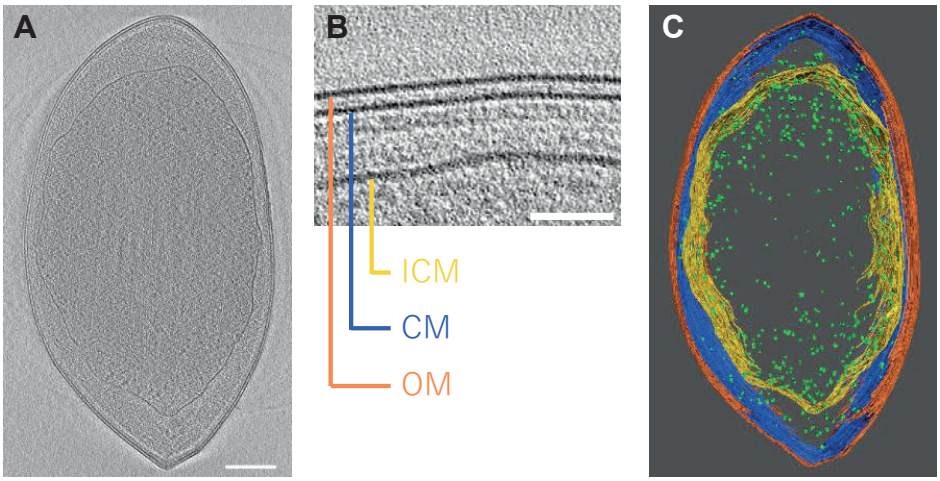

Cross-sectional images (A, B) reconstructed from a tilt-series obtained by cryo-electron tomography and a three-dimensional structural model (C). Intracytoplasmic membrane (ICM, yellow), cytoplasmic membrane (CM, blue), outer membrane (OM, orange), and ribosome-like particles (green). (Bar, 200 nm (A), 50 nm (B))

also, albeit in smaller numbers, in the cytoplasm outside the intracellular membrane (Fig. 2). This suggests the possibility of translation occurring in separate cytoplasmic compartments.

The unique characteristics of RT761 extend beyond the intracellular membrane enclosing its genomic DNA. Cryo-EM observations further revealed (i) a large indentation in the intracellular membrane (**Fig. 4**①), (ii) a thin layer between the cytoplasmic membrane and the intracellular membrane (Fig. 4②), and (iii) a periodic zip-like surface structure on the outer membrane (Fig. 4③). While the biological relevance of these structures remains unknown, their direct visualization represents an important first step toward uncovering their functional roles.

On the other hand, detailed Cryo-EM observations have also raised fundamental questions regarding the very existence of the "third membrane." The periodic structure on the outer membrane (Fig. 4③) closely resembles an S-layer, a proteinaceous surface layer found in some bacteria and archaea. If the outermost layer is indeed an S-layer rather than a lipid membrane, then what was initially thought to be the cytoplasmic membrane would actually be the outer membrane, and the innermost intracellular membrane would correspond to the cytoplasmic membrane. This would mean that RT761 does not possess a third intracytoplasmic membrane at all. Cryo-EM imaging has revealed that all three membranes in RT761 exhibit a characteristic bilayer structure, strongly suggesting that they are composed of lipid bilayers. However, the biochemical composition of the outermost membrane has not yet been determined, leaving open the possibility that it could be an S-layer [6]. Additionally, the tilt-angle limitations inherent in tomography restrict the observable range in three-dimensional reconstructions, creating potential "blind spots." In these unobservable regions, the intracellular membrane may be continuous with the cytoplasmic membrane, meaning that the intracellular membrane could simply be an extension of the cytoplasmic membrane rather than a distinct structure [6].

The discussion surrounding this third membrane became a crucial point in the exchange with reviewers of the research paper on strain RT761. Overturning the existing definition of prokaryotes requires the accumulation of further evidence through additional observations and analyses. Recently, strain M15, a close relative of RT761, was cultivated from formation water in a domestic gas field distinct from the Southern Kanto Gas Field. Similar to RT761, M15 possesses an intracellular membrane that localizes genomic DNA, suggesting that this feature is a conserved trait within the group that includes both strains [7]. Moving forward, key challenges include not only confirming the identity of this third membrane and elucidating its biological significance but also identifying related genetic traits and clarifying their evolutionary origins and ecological functions.

The ecological characteristics of RT761 are outlined below. In general, organisms obtain energy through redox reactions in their metabolic processes. RT761 oxidizes sugars under anaerobic conditions, reducing protons in the process to generate energy, ultimately releasing hydrogen gas. This hydrogen is then oxidized by methanogenic archaea, which reduce carbon dioxide to methane, serving as their energy source. In environments where RT761 coexists with methanogens, the hydrogen released by RT761 is efficiently consumed by methanogens, allowing RT761 to obtain more energy. Evidence suggesting such a mutualistic relationship includes the fact that the DNA sequences of the group to which RT761 belongs are predominantly detected in environments where methanogens are present. In natural environments, RT761 is likely to form an ecosystem in which both itself and methanogens secure a stable energy supply through symbiosis. Such microbial interactions are considered a crucial survival strategy in subsurface sedimentary environments, where energy sources are extremely limited.

Fig. 3 Cellular structure of strain RT761 based on confocal laser microscopy.

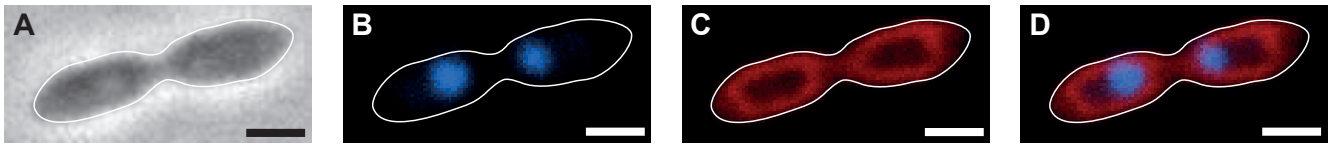

White lines indicate cell outlines. (A) Bright-field image, (B) DNA stained with Hoechst, (C) Membrane lipids stained with FM4-64, and (D) Overlay of (B) and (C). The DNA is enclosed by membrane lipids present inside the cell. (Bar, 1 μm)

Fig. 4 Unique subcellular structures of strain RT761 observed by Cryo-EM.

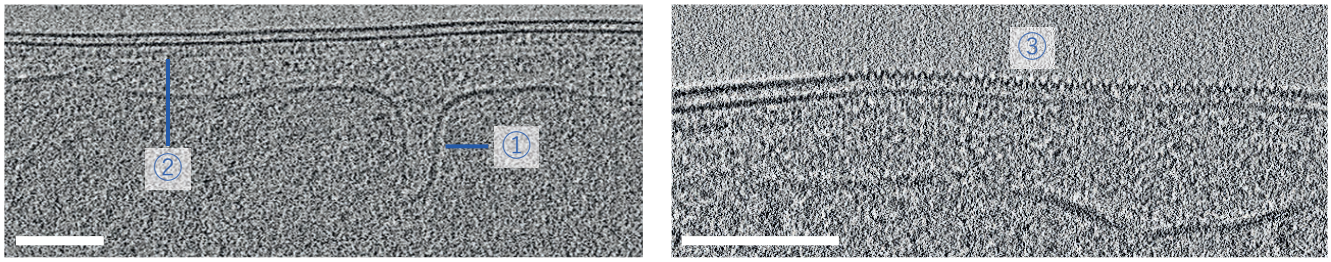

(1) Invagination of the intracytoplasmic membrane into the cell interior, (2) a thin layer located inside the cytoplasmic membrane, and (3) a periodic 4 nm surface pattern on the outer membrane. (Bar, 100 nm)

Discovery of *Fidelibacter multiformis* strain IA91, a novel phylum bacterium that synthesizes its own cell wall by acquiring cell wall components from other bacteria

Saving energy is a key factor in culturing previously uncultured microorganisms from subsurface sedimentary environments. We re-evaluated cultivation strategies and devised a novel method focusing on interactions mediated by cell wall components. During cell division, bacteria partially degrade their peptidoglycan cell walls and release muropeptides (MPs). These MPs are taken up by cells and reused as materials for new cell wall synthesis (**Fig. 5**). Based on this, we hypothesized the existence of bacteria that utilize MPs released by other bacteria to survive while minimizing their own energy expenditure (Fig. 5). By applying a cultivation method designed to promote the growth of such MP-scavenging bacteria, we successfully obtained a pure culture of strain IA91 (for details, see the original research paper [2]).

Surprisingly, IA91 was not merely scavenging exogenous MPs but was found to be an MP-dependent bacterium that could not synthesize its cell wall without MPs. When culture supernatants containing MPs from other bacterial species were added, IA91 exhibited a rod-shaped morphology and grew. In contrast, when MPs were not supplied, the cells became irregularly spherical and ceased to grow (**Fig. 6**). Peptidoglycan, a major component of the bacterial cell wall, serves as a structural framework determining cell shape. Bacteria lacking a cell wall are known to assume a spherical shape due to turgor pressure. Indeed, fluorescent staining of IA91 cells revealed the presence of a cell wall only in rod-shaped cells, suggesting that IA91 incorporates MPs from other bacteria as building materials for its own cell wall. To investigate the nature of the peptidoglycan constructed using MPs from other species, we attempted to observe its texture using cryo-electron microscopy (Cryo-EM). However, we were unable to identify a distinct cell wall-like layer in either rod-shaped or spherical cells (**Fig. 7**). Since IA91 is a Gram-negative bacterium, it is likely that its thin peptidoglycan layer falls below the detection limit. Similarly,

Fig. 5 Bacterial interactions mediated by cell wall components.

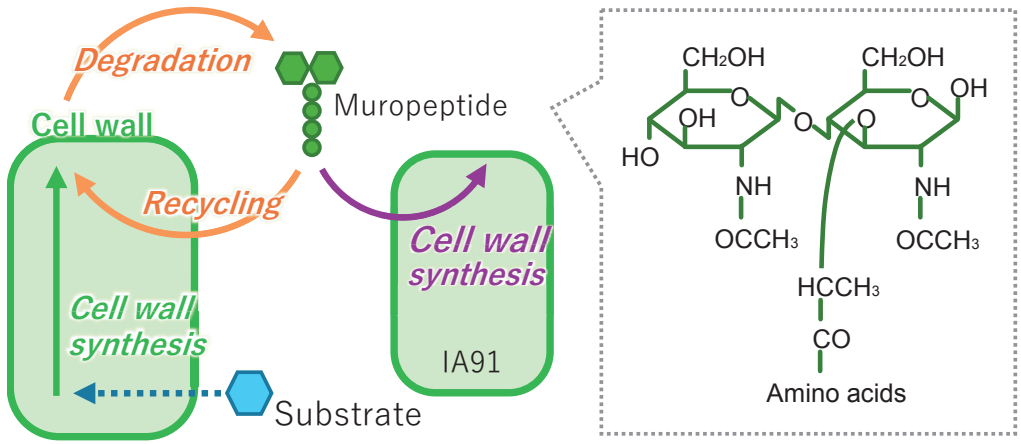

During cell division, bacteria undergo significant morphological changes alongside continuous remodeling of their peptidoglycan-based cell wall. Cell wall fragments are degraded, released, and recycled into muropeptides, which consist of sugars and peptides.Strain IA91 harnesses these muropeptides to synthesize its own cell wall, bypassing the need for de novo synthesis from primary substrates.

Fig. 6 Morphological changes in IA91 cells.

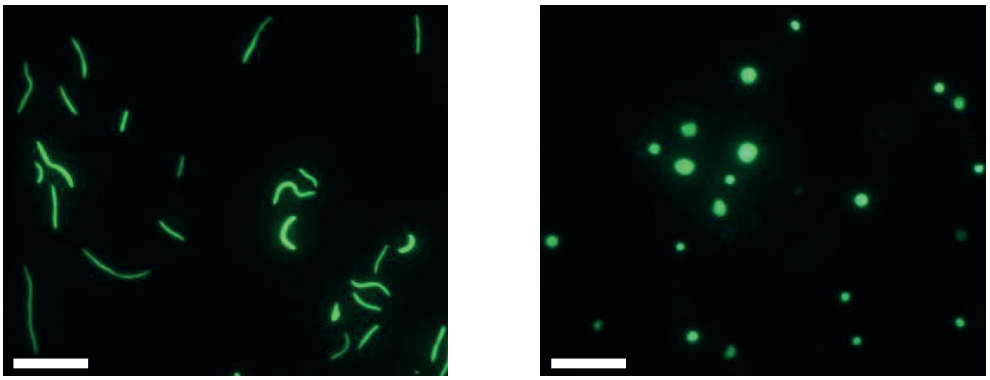

Nucleic acids were stained with SYBR Green and observed using a light microscope. When cultured with the supernatant of other bacterial cultures, IA91 grows in a rod-shaped form (left); in the absence of such supernatant, it transforms into a coccoid shape (right) and eventually dies. (Bar, 5 μm)

Fig. 7 Membrane structures of strain IA91 observed by Cryo-EM.

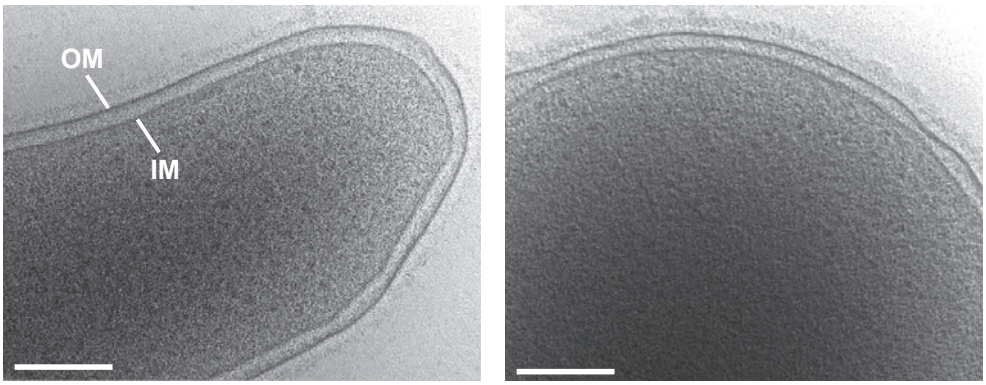

The cell wall, which is expected to exist between the outer membrane (OM) and the cytoplasmic membrane (IM), was not observed in either rod-shaped (left) or coccoid (right) cells. (Bar, 200 nm)

in Cryo-EM observations of another Gram-negative bacterium, strain RT761, the peptidoglycan layer was barely visible (Fig. 2).

When we attempted to supply individual components of MPs—such as sugars, amino acids, or even whole cell walls, simulating dead bacteria—IA91 did not grow. This demonstrated that IA91 requires MPs specifically released by living bacteria for its growth. This finding implies that IA91 can only survive in close proximity to actively growing bacterial populations. Evolutionary analysis suggested that the MP-dependent metabolic trait originated in the common ancestor of the group to which IA91 belongs and has been inherited by its descendants, including IA91, which inhabit anaerobic environments. This indicates that reducing the energy cost of cell wall synthesis by scavenging MPs was an evolutionarily advantageous survival strategy, outweighing the lethal risk of MP depletion.

Conclusive Remarks

My fundamental motivation for cultivating unknown, uncultured microorganisms from subsurface environments stems from pure intellectual curiosity about the unknown. Extending from this curiosity, the scientific and societal significance of such endeavors becomes evident. Through the power of science, making "first contact" with organisms that no one in the world has ever seen and unraveling their ecology is an unparalleled thrill. In the studies of strains RT761 and IA91 introduced in this article, the moment of successfully obtaining a pure culture and observing their cellular structures using Cryo-EM was particularly moving. The process, which began with environmental sample collection and took several years to achieve pure culture of a single species, culminated in the extraordinary experience of finally encountering an unknown life form in its near-natural state through Cryo-EM. What once appeared as mere black specks under an optical microscope was now revealed in intricate detail.

The serendipitous discovery of the intracellular membrane surrounding the genome of strain RT761 was a fortunate event, made possible solely by advances in microscopy technology. As a researcher using this technology, I have a further aspiration—to integrate high-resolution cellular structure imaging with chemical identification of cellular components. If such a technique becomes feasible, it could resolve debates surrounding the lipid membrane and S-layer of strain RT761, providing a powerful tool not only for microbiology but for all life sciences. Regardless of how technological innovations unfold, I strongly hope that they will continue to support the foundation of microbiology and contribute to its advancement.

Acknowledgements

I would like to express my sincere gratitude to Dr. Naoki Hosoki of JEOL Ltd. for his cooperation in observing the bacterial cells of strains RT761 and IA91 using the CRYO ARM™ 300 and CRYO ARM™ 300 II cryo-electron microscopes. I am also deeply grateful to Dr. Nobu K. Masaru of the Japan Agency for Marine-Earth Science and Technology, as well as Dr. Hideyuki Tamaki and Dr. Yoichi Kamagata of the National Institute of Advanced Industrial Science and Technology, for their dedicated efforts in the ecological study and publication of these microbial strains.

References

[1] Katayama T, Nobu MK, Kusada H, Meng XY, Hosogi N et al. Isolation of a member of the candidate phylum 'Atribacteria' reveals a unique cell membrane structure. *Nature Communications* 2020, **11**, 6381.

[2] Katayama T, Nobu MK, Imachi H, Hosogi N, Meng X-Y et al. A Marine Group A isolate relies on other growing bacteria for cell wall formation. *Nature Microbiolology* 2024, **9**, 1954-1963.

[3] A year of microbiology. *Nature Microbiology* 2024, **9**, 3079-3080.

[4] Parks DH, Chuvochina M, Rinke C, Mussig AJ, Chaumeil P-A et al. GTDB: an ongoing census of bacterial and archaeal diversity through a phylogenetically consistent, rank normalized and complete genome-based taxonomy. *Nucleic Acids Research* 2021, **50**, D785-D794.

[5] Nobu MK, Dodsworth JA, Murugapiran SK, Rinke C, Gies EA et al. Phylogeny and physiology of candidate phylum 'Atribacteria' (OP9/JS1) inferred from cultivation-independent genomics. *The ISME journal* 2016, **10**, 273-286.

[6] van Teeseling MCF, Jogler C. Cultivation of elusive microbes unearthed exciting biology. *Nature Communications* 2021, **12**, 75.

[7] Kawamoto H, Watanabe M, Mochimaru H, Nakahara N, Meng X-Y et al. *Atrimonas thermophila* gen. nov., sp. nov., a novel anaerobic thermophilic bacterium of the phylum Atribacterota isolated from deep subsurface gas field and proposal of *Atrimonadaceae* fam. nov. within the class *Atribacteria* in the phylum *Atribacterota. Systematic Applied Microbiology* 2024, **47**, 126515.

X-ray and Electron-Beam Analyses for Teeth of Chiton Accumulating Iron at High Concentrations

Chiya Numako[1], Seiichi Takami[2], Shiori Kamijo[3], Takeshi Otsuka[3], Yusuke Sakuta[3], Shunsuke Asahina[3]

[1] Chiba University, Graduate School of Science, [2] Nagoya University, Graduate School of Engineering, [3] JEOL Ltd.

Chitonidae is known to form teeth composed mainly of inorganic iron compounds such as Magnetite (Fe_3O_4) and Goethite (α-FeOOH). Magnetite is a complex oxide and ferromagnetic material, whose physical properties vary greatly depending on its magnetic structure. In this study, we considered sample preparation methods and carried out measurements with X-ray analyses using a scanning soft X-ray microscope at BL14U, Nano Terasu, and several analyses by an electron beam using SEM/EPMA of JEOL for the same sample of the teeth of chiton, in order to elucidate the distribution of these iron species and magnetic properties of the magnetite in the teeth of chiton.

Introduction

Chitonidae (**Fig. 1**(a)) belonging to Polyplacophora in Mollusca is known for their eight aragonitic shell plates (Fig. 1(a)) and their ability to curl up like a dung beetle, and their hard teeth (Fig. 1(b)), which are mainly composed of magnetite. Some Molluscs use a radula as a file for feeding, which is a tongue-like organ lined with teeth. Several tooth cusps form a horizontal line, called a teeth row, and several teeth rows are lined up longitudinally on a chitinous base membrane in a radula, e.g., a teeth row is made up of 17 tooth cusps (a teeth row is within the rectangle in Fig. 1 (d)), and there are approximately 80 teeth rows on a radula in about 2 cm long in the case of *Acanthopleura japonica* (Fig. 1 (a)).

In addition, there is a pair of black large lateral teeth composing of iron compounds in a teeth raw (Fig. 1 (b); in this paper, these are referred to as teeth), which is a specific feature of Chitonidae in Mollusca. Only the 5-7th teeth rows on the mouth side (Fig. 1 (d), side (B)) are used for feeding in a radula, scraping algae from intertidal rock surfaces, and are worn away by contacting with the rocks. With a similar speed of the consumption of teeth, new teeth are produced on an opposite side of the radula (Fig. 1(d), side (A)), and then sent to the mouth side like a conveyor belt. During this transport of teeth, they gradually get a maturation and their color and composition change significantly. At the beginning of the formation of the radula, the teeth are made up of a colorless chitinous frame without any inorganic components (Fig. 1 (d), right side of (A)), however, iron deposition starts to the inside of the frame forming soft reddish teeth around the 8-10th teeth rows, and then, the feeding surface of the teeth is filled with magnetite, forming a harder, gray teeth after the 11th teeth row. Around the 30-40th teeth rows, the back of the teeth is filled with transparent calcium phosphate, which supports increasing mechanical strength, and makes the teeth mature enough to be used for feeding. The radulae of Molluscs are good subjects for studying the formation process of teeth, the biological hard tissue, because the all maturation stages of the teeth are arranged in a radula in the order of formation and maturation process.

It is also interesting to note that iron is the main component of the teeth of Chitonidae. Iron is an essential element for vertebrates, as they use iron-based hemoglobin to transport oxygen, whereas Mollusca use copper-based hemocyanin to transport oxygen and iron is not so an important element commonly. It is also not easy for marine-dwelling creatures to accumulate iron from the environment into their bodies. There is a lot of iron on the Earth's surface, and some of them are dissolved in the hydrosphere as Fe(II) and/or Fe(III) ions. Freshwaters such as rivers and lakes with low pH levels can contain dissolved iron in relatively high concentration, however, most of the Fe(III) ions would be hydrolysed to form precipitations such as iron oxide or iron hydroxide, e.g. FeOOH, because of high pH of seawater (ca. pH = 8). The dissolved oxygen from the atmosphere on the Earth has a significant effect to the dissolved iron ions changing into Fe(III) ions, so that, it is known that the concentration of iron ions in seawater is very low, almost at the ppt level. Iron content of magnetite (Fe_3O_4), which is the main component of the teeth of the chiton, is about 70 wt%. If it would be produced from the dissolved iron ions in seawater, iron accumulation with a billion times greater than normal seawater is required. Chitonidae is unique marine organisms that have developed such an incredible ability to accumulate iron in order to form magnetite teeth.

The inorganic components of the teeth of chitons are also

〉〉 1-33, Yayoicho, Inage-ku, Chiba-shi, Chiba, 263-8522 Japan | E-mail: numako@chiba-u.jp

characteristic. The longitudinal section of the mature teeth of chiton was prepared by polishing the chiton embedded in polyethylene resin with a sandpaper and alumina abrasive. The obtained section showed that there are two components with completely different properties; the hard black feeding surface composing iron and the soft transparent back side composing calcium phosphate (Fig. 1 (c)).

The teeth of vertebrates are made up of two tissues, dentin and enamel, both of which are composed mainly of hydroxyapatite. On the other hand, the inorganic components with different chemical compositions, such as iron compounds and calcium phosphate, are arranged in different parts of a tooth in the case of Chitonidae. It is interesting to see how the formation and arrangement of these inorganic components are controlled within a single tooth.

Powder X-ray diffraction measurements (XRD) of the teeth of chiton revealed that only magnetite (Fe_3O_4) was detected in the teeth in the early maturation stage (Fig. 1(d) (A)), and there were multiple crystalline components such as Goethite (α-FeOOH), Lepidocrocite (γ-FeOOH), and hydroxylapatite ($Ca_{10}(PO_4)_6(OH)_2$) in the mature teeth (Fig. 1(d)(B)). The X-ray diffraction profiles of the magnetite in the early maturation stage was sharp with high intensity like natural magnetite. However, the peak intensities of the other components were low indicating their low crystallinities. It is also interesting that the iron components with different chemical compositions, such as magnetite and FeOOH, are produced separately. Therefore, in order to elucidate formations and arrangements of these components in the teeth of chiton, high-sensitivity, high-spatial-resolution elemental analysis with Scanning Electron Microscope; SEM (JSM-IT800<SHL>: JEOL Ltd.) and Electron Probe Micro Analyzer; EPMA (JXA-iHP200F: JEOL Ltd.) were applied to a thin section of teeth of chiton. Electron Backscatter Diffraction; EBSD (Symmetry S3 Oxford Instruments) was used for crystal orientation state analysis to elucidate crystalline property of the inorganic components of the teeth of chiton.

Magnetite is a complex oxide containing both of Fe(II) and Fe(III) while FeOOH contains only Fe(III), so that, it is possible to visualize how they mix together in the feeding surface of a tooth of chiton by distribution analysis of Fe(II). Furthermore, although magnetite is a ferromagnetic substance, it might be also possible to distinguish and detect these components by magnetic imaging with high spatial resolution. For these purposes, measurements of X-ray absorption spectra for iron and X-ray magnetic circular dichroism (XMCD) using a synchrotron radiation nano-beam were performed for the teeth of chiton at BL14U in 3 GeV high-brilliance synchrotron radiation facility Nano Terasu.

X-ray analyses at BL14U in Nano Terasu

When electrons are accelerated to almost the same speed as light and the direction of the straight-ahead electrons is

Fig. 1 Chiton (*A. japonica*) and its radula.

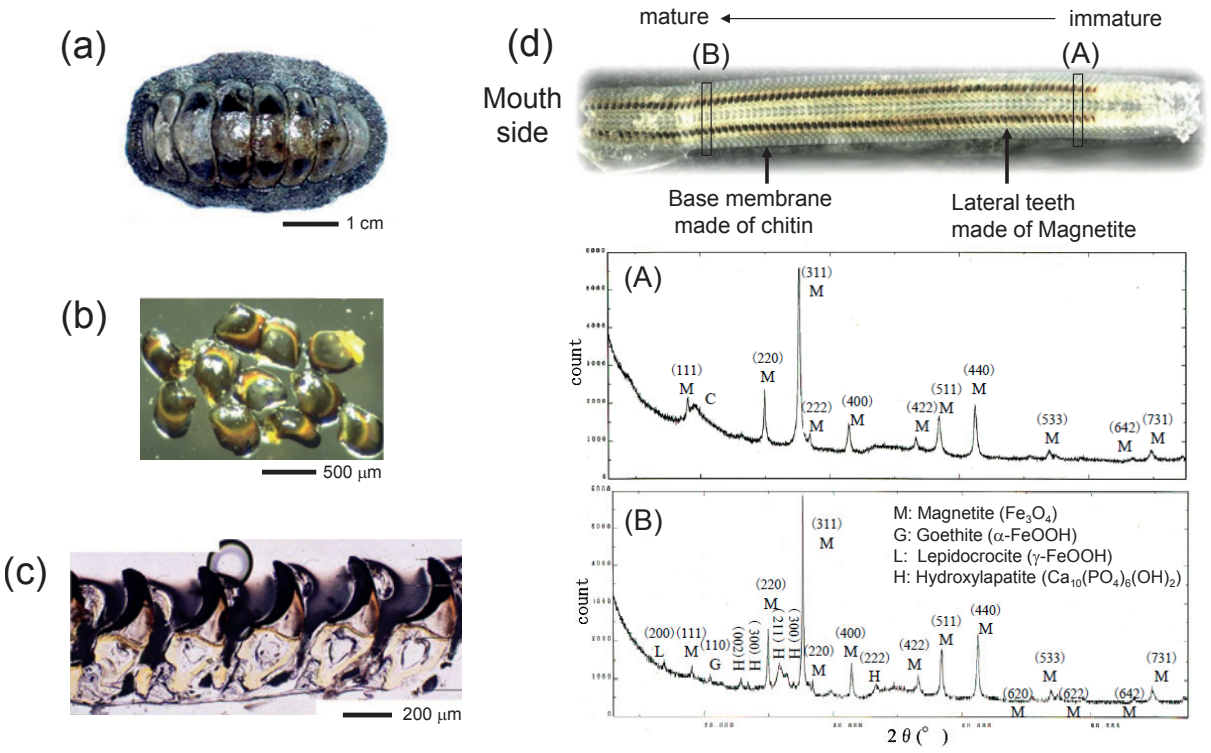

(a) External appearance of chiton, (b) an optical microscopic image of iron-enriched teeth of chiton, (c) optical microscopic image of a longitudinal section of radula of chiton fixed in polyethylene resin and polished to reveal the interior surface, (d) optical microscopic image of entire of a radula of chiton, and powder X-ray diffraction profiles measured for a tooth of chiton ((a) teeth in the early stages of maturation; (b) mature teeth using for feeding).

bent with powerful electromagnets, synchrotron radiation (SR) is generated in the tangential direction. SR is a continuous electromagnetic wave with a wide range of wavelength components from infrared to hard X-rays and has the characteristics of extremely high intensity, laser-like directionality, and emission in short pulses on the order of nanoseconds. In synchrotron radiation facilities, the generated SR is split into multiple beamlines, where various measurements such as X-ray diffraction, photoelectron spectroscopy and X-ray absorption spectroscopy, etc., are conducted simultaneously. Japan has been a leader in pioneering research on synchrotron radiation technology along with the USA and Europe, and has built many synchrotron radiation facilities since the 1960s. Nano Terasu is the latest synchrotron radiation facility built next to Tohoku University and operated from 2024. One of the main features of SR of Nano Terasu is highly brilliance around soft X-ray region.

BL14U at Nano Terasu is a beamline using soft X-rays in 200 to 1400 eV, where quasi-monochromatic X-ray with small source size and angular divergence obtained by an undulator as an insertion source is further focused by a Fresnel zone plate into a nanobeam of about 30 nm. A scanning soft X-ray microscopy system can be used at BL14U, in which a nanobeam is irradiated onto the sample with moving a sample stage, and the transmitted X-ray intensity is detected for imaging. A scanning range of the sample stage is up to 60 × 60 μm^2. The system is also capable of applying a magnetic field of up to 8 T by means of a superconducting magnet, and features imaging of magnetic domain and magnetic circular dichroism imaging for magnetic materials. The size of the teeth of chiton is ca. 200 × 500 μm^2, so that the beam size of BL14U has sufficient spatial resolution for the specimen to be utilized complementary to SEM and EPMA. Considering their features, we applied the following measurements on the same sample; classification imagings of Fe(II) and Fe(III) and XMCD mapping at Nano Terasu, SEM and EPMA measurements at JEOL.

Experimental procedure

Radula specimens were extracted from the chiton, *A. japonica*, collected at coast of Katsuura, Chiba Prefecture, and placed into micro vials with distilled water to prevent drying-up, and stored in a refrigerator. A pair of matured large lateral teeth were cut from a radula of chiton using a utility knife, and cut in half as shown in **Fig. 2** (a). When the cross-section of the tooth was observed using a high-resolution SEM, there were some contaminations attached on the cross-section. This might be due to the organic matter from soft tissue of chiton. Because it was difficult to analyze this sample with the surface-sensitive scanning soft X-ray microscope at BL14U, Nano Terasu, a JEOL CROSS SECTION POLISHER™ (CP), which can prepare cross sections by argon ion milling with cooling the sample, was applied to preparation of the measurement specimen on the teeth of chiton. As a result, no contamination and smooth cross section surface could be observed (Fig. 2 (b)).

In order to improve the working efficiency at BL-14U, two teeth were embedded with epoxy resin on a silicon substrate for cross and longitudinal directions simultaneously. After mechanical polishing of about 1/3 of the tooth thickness, CP processing with argon ion irradiation at 40 mA, 4 kV was performed for 8 hours while the sample was cooled at -100 °C (**Fig. 3** (a)). The specimen was mounted on the sample stage of the scanning soft X-ray microscope at BL14U. As the system did not have a camera system to check the sample position in a sample chamber, a tungsten wire was attached next to the specimen on the sample holder in order to check the sample position by the transmitted X-ray image. SEM observations were performed in advance to record the spacial relationship between two teeth of chiton and the wire (Fig. 3 (b)). No coating was applied on the surface of the specimen in order to prevent any effect from the coating material to the X-ray measurements. The SEM image indicated a high contrast of the secondary electrons between the feeding surface and a darker contrast on the back. This contrast allows us to confirm the position of the Fe-based feeding surface in the sample.

Fig. 2 Longitudinal-sectional specimen preparation of the teeth of chiton.

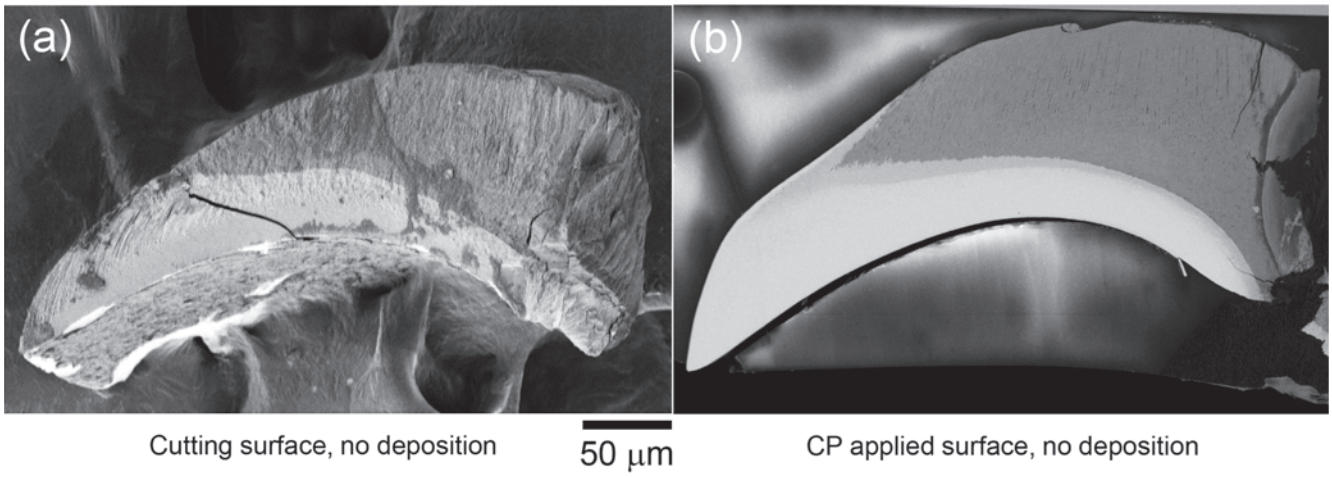

(a) SEM image of a tooth of chiton, split longitudinally with a utility knife and held intact on carbon tape; (b) SEM image of a specimen of a tooth of chiton embedded and fixed in epoxy resin on a silicon substrate and subsequently subjected to mechanical polishing and CP milling.

X-ray analyses in Nano Terasu

The specimen of teeth of chiton described above was brought to BL14U, Nano Terasu, and introduced into the sample chamber of the scanning soft X-ray microscope. Since the tungsten wire was spanned in the Y direction, the position of the wire was determined by scanning the sample stage roughly in the X direction while monitoring the intensity of the transmitted X-rays. Next, the sample stage was moved in the X direction for a predetermined distance by the SEM observation. The sample stage was then scanned in the Y direction to find the specimen. Due to the small scanning range of 60 × 60 μm^2, compared to the size of the tooth of chiton (ca. 200 × 500 mm^2), the stage was moved by a coarse movement and two-dimensional X-ray absorption imaging was performed, and then the acquired X-ray absorption images were combined to obtain an overall view of the feeding face of teeth of chiton. Step size of X-ray absorption imaging was 300 nm in each X and Y direction.

The energy of the L_3 absorption edge of iron is 708.2 eV for Fe(II) and 709.5 eV for Fe(III). When the X-ray absorption image is obtained with the incident X-rays in 708.2 eV, the image strongly reflects the distribution of Fe(II) because Fe(II) mainly contributes to X-ray absorption. On the other hand, the X-ray absorption image at 709.5 eV mainly reflects the distribution of Fe(III) because Fe(III) mainly contributes to X-ray absorption. X-ray absorption images of a cross and longitudinal section of a tooth of chiton, respectively, using the incident X-rays at 708.2 eV and 709.5 eV are shown in **Fig. 4**. In both cross (Fig. 4 (a), (b)) and longitudinal (Fig. 4 (c), (d)) sections, it was clear that X-ray absorption was high at the feeding surface, where iron was the main component, while almost no absorption occurred at the back. It was also found that there were two areas indicating high X-ray absorption and relatively low X-ray absorption within the feeding surface where iron is a main ingredient. In the Fe(II) image (Fig. 4 (a), (c)), the low X-ray absorption area was observed between the outer feeding surface and the back, named the intermediate region. In the Fe(III) image (Fig. 4 (b), (d)), the intermediate region indicated stronger X-ray absorption than the outer feeding surface. The teeth of chiton have magnetite containing Fe(II) and Fe(III) and FeOOH containing Fe(III) (Fig. 1(d)). These images of Fe(II) and Fe(III) show that magnetite existed in the outer feeding surface areas with high absorption intensity in Fe(II) image, while FeOOH existed in the intermediate region with high absorption intensity in Fe(III) image (Fig. 3 (b), (d)), respectively.

Next, MCD measurements were performed on the longitudinal section of the tooth of chiton at 60 × 60 μm^2 area in the outer feeding surface, where ferromagnetic magnetite was a main component. MCD measurements were performed for both in the original state and after applying an external magnetic field of 1 T (Fig. 4 (d), bottom right). The MCD images after the application of 1 T also showed a uniform distribution of X-ray absorption in the measurement area, indicating that the magnetite crystals were not magnetically oriented in the tooth of chiton. Although the imaging was carried out in 300 nm step in this study, the results suggest that magnetite crystals in the teeth of chiton are tiny and randomly agglomerated different from natural mineral magnetite, so that magnetic domains could not be observed at this spatial resolution. Alternatively, if the magnetic orientation of magnetite is in the in-plane direction of this measurement plane, it will be difficult to detect using this measurement

Fig. 3 SEM image for a measurement specimen of teeth of chiton prepared for scanning soft X-ray microscopy at BL14U, Nano Terasu, and SEM/EPMA measurements at JEOL.

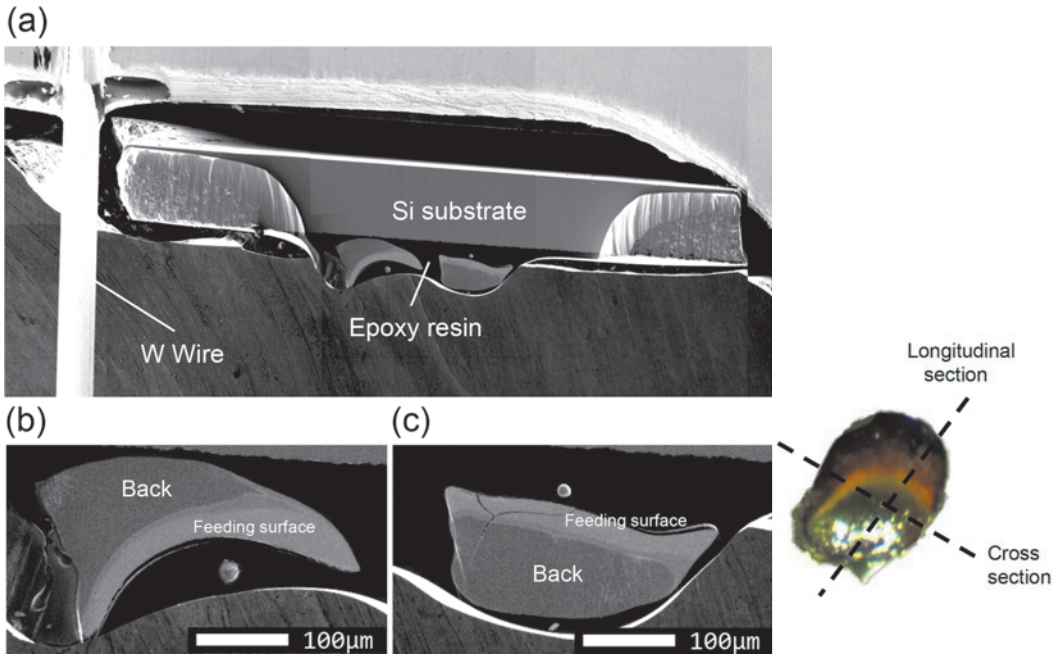

(a) Low magnification image of the specimens; the teeth of chiton were encased and fixed in epoxy resin on a silicon substrate and sectioned by mechanical polishing and CP milling. To confirm the sample position for the measurement at BL14U, a tungsten wire was attached to the left side of the sample and the distance in the X-direction between the wire and the two teeth of chiton was measured in advance by SEM observation. (b) Longitudinal section specimen, and (c) Cross section specimen of a tooth of chiton.

Fig. 4 X-ray absorption images of the specimens of teeth of chiton, taken with a scanning soft x-ray microscope at BL14U.

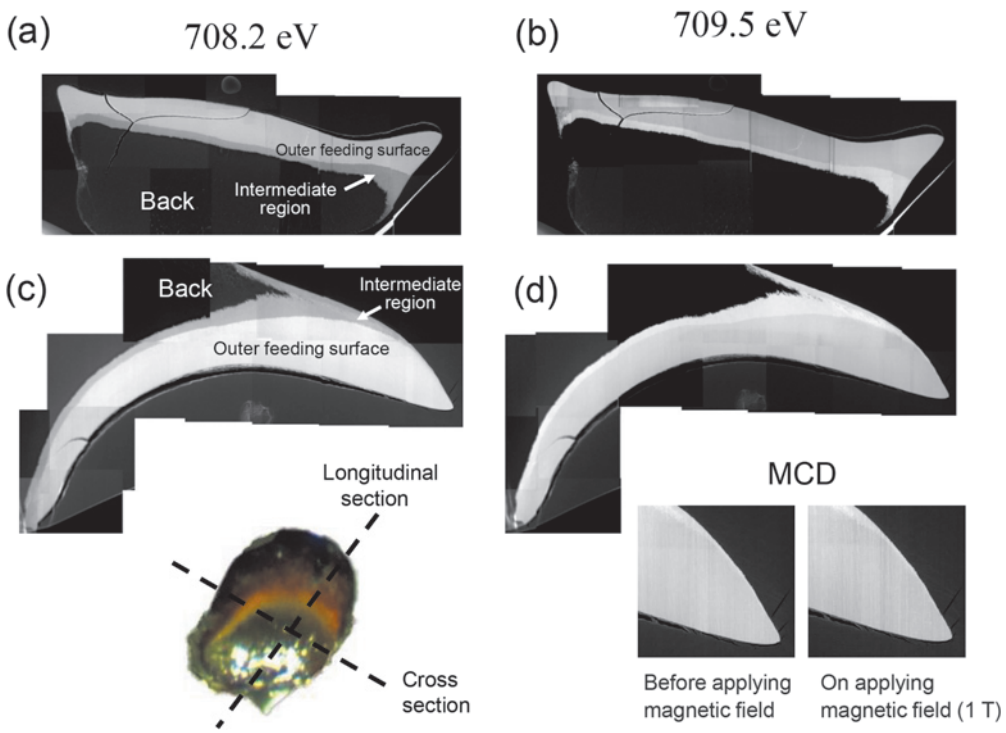

(a) (b) X-ray absorption image for a cross-section, and (c) (d) a longitudinal section of a tooth of chiton.
(a) (c) X-ray absorption image at 708.2 eV; indicating Fe(II) distribution, and (b) (d) at 709.5 eV; indicating Fe(III) distribution in a tooth of chiton.

system, which detects X-rays in the vertical direction. To confirm this, we thought it would be necessary to perform the same measurement on a cross-section obtained by rotating the measurement surface by 90° in the future.

Analysis by an electron beam

Backscattered electron images were observed on a longitudinal section of the tooth of chiton using SEM. In this measurement, a different longitudinal section of the tooth of the chiton was used to check damages to the specimen caused by the electron beam. Since the tooth of chiton is almost inorganic hard tissue but also biological sample, an osmium coating in 3 nm was applied on the surface of the specimen in order to prevent charging and damage from the electron beam.

The entire sample was scanned with an electron beam at high speed to see the effect of the electron beam on the sample, and good secondary electron images were obtained without charge-up and damages on the surface of the specimen. Then secondary electron image observation at low scanning speed was also carried out for the same specimen, a higher resolution secondary electron image could be obtained with no charge-up. Based on the above conditions, high-resolution backscattered electron image observation was carried out for the specimen of the tooth of chiton.

In the backscattered electron images for the entire tooth of chiton, three areas with different backscattered electron intensities could be observed (**Fig. 5** (a)). Similar to the classification imaging of Fe(II) and Fe(III) in Fig. 4, two regions with different backscattered electron intensities existed in the feeding surface, and one of them indicating lower electron intensity seemed to correspond to the intermediate region in Fig. 4. Figure 5 (b) shows a backscattered electron image for the measurement area surrounded by the dotted line in Fig. 5(a) including the feeding surface. The magnified images for 5,000 times on the intermediate region and the back showed no border material e.g., membrane, among these three regions. The constituent materials with different backscattered electron intensities were adjacent to each other, and fibrous tissues existed in a dendritic pattern over those three regions. Since a chitinous frame is formed into the tooth shape and then inorganic components are filled into it to form the tooth, this fibrous tissue seemed to be a fibrous structure of chitinous material that was spread out in a tree-like pattern to support the shape of the tooth. It was also found that three materials with different backscattered electron contrast were filled into the space among the fibrous chitin uniformly while controlling the arrangement in three dimensions.

The classification imaging of Fe(II) and Fe(III) (Fig. 4) indicated that both constituents of the intermediate region and outer feeding face contained iron respectively. The boundary of those constituents was clear in a backscattered electron image magnified 30,000 times (Fig. 5 (c)), and it was observed that each component was formed and filled independently rather than such as functionally gradient materials. Further observations at 100,000x revealed that the crystal grains of these components were about 100 nm in size and they intertwined and missed around the boundary of them to join the intermediate region and outer feeding surface (Fig. 5 (d)).

SEM observations and elemental analyses with EDS were

then carried out on the same specimen as using the X-ray analyses at BL14U, Nano Terasu (**Fig. 6** (a)). First, an electron beam was scanned in a region that included the outer feeding surface, the intermediate region and the back (Fig. 6 (b)) and the EDS spectra were obtained (Fig. 6 (c)). Since iron (as a main component), calcium, phosphorus, oxygen, and carbon were detected in EDS spectra, elemental mapping of iron, oxygen, calcium and phosphorus was performed on the same region as an above measurement (Fig. 6 (d)). The results indicated that iron is present in the intermediate region and outer feeding surface of the tooth of chiton but not in the back, where calcium and phosphorus are homogeneously distributed as the main components. It was also found that lower backscattered electron intensity at the back region than that of the intermediate region and outer feeding surface was due to its components, calcium and phosphorus, which have lower electron reflectance than that of iron. Furthermore, the oxygen concentration in the intermediate region was much higher than that of the outer feeding surface (Fig. 6 (d)), however, differences of concentration of iron on those two regions could not be observed clearly. The difference in oxygen concentration between the intermediate region and the outer feeding surface seemed to reflect the difference in the chemical composition of the respective iron regions. However, it was difficult to clarify from the standardless quantitative data from elemental mapping with EDS.

Therefore, a Wavelength Dispersive X-ray Spectrometer (WDS) installed in the EPMA was used for the elemental map of the entire tooth of chiton and quantitative analyses for specific measurement points of those three regions with an accelerating voltage of 15 kV and a probe current of 20 nA, in order to analyze the chemical composition of each component. The results are shown in **Fig. 7**. The map analysis confirmed that Fe and O were present at high concentration in the intermediate region and the outer feeding surface while Ca, O and P were present on the back (Fig. 7 (b)). The standardless quantitative analysis of each region showed that the weight ratio of Fe and O was 73 : 27 in the outer feeding surface, 63 : 36 in the intermediate region, and 38 : 20 : 41 for calcium, phosphorus and oxygen in the back (Fig. 7 (c)).

For further identifications of the chemical composition of these regions, a scatterplot analysis was applied under focusing on iron and oxygen, and then, they were divided into two materials with different Fe and O compositions (Fig. 7 (d)). It was shown by XRD that magnetite and FeOOH were contained in the mature teeth of chiton (Fig. 1 (d)(B)). The theoretical values for the weight ratio of iron and oxygen are 72 : 28 for magnetite and 64 : 36 for FeOOH, although hydrogen is not detectable with WDS. From these, a linear analysis of multiple measurements of WDS in the teeth of the chiton plotted on the scatterplot showed a good correlation with magnetite in the feeding surface and FeOOH in the intermediate region. Finally, these EPMA analyses indicated a distribution of three phases with different chemical compositions in the longitudinal section of the tooth of chiton, as shown in Fig. 7 (e).

In addition, EBSD measurements were carried out with the JSM-IT800<SHL> on the area composing the back, the intermediate region, and the outer feeding surface (**Fig. 8** (a)), in order to obtain information on the domain structure and orientation of the crystalline components of the teeth of chiton. 10 kV for the acceleration voltage and 500 pA for the probe current, which are lower measurement acceleration condition than usual, were used for this measurement in order to reduce sample damages to the teeth of chiton. Furthermore, a shorter working distance of 10.1 mm was used to keep the beam diameter as small as possible during analyses. The

Fig. 5 Backscattered electron image of a CP-processed specimen of teeth of chiton.

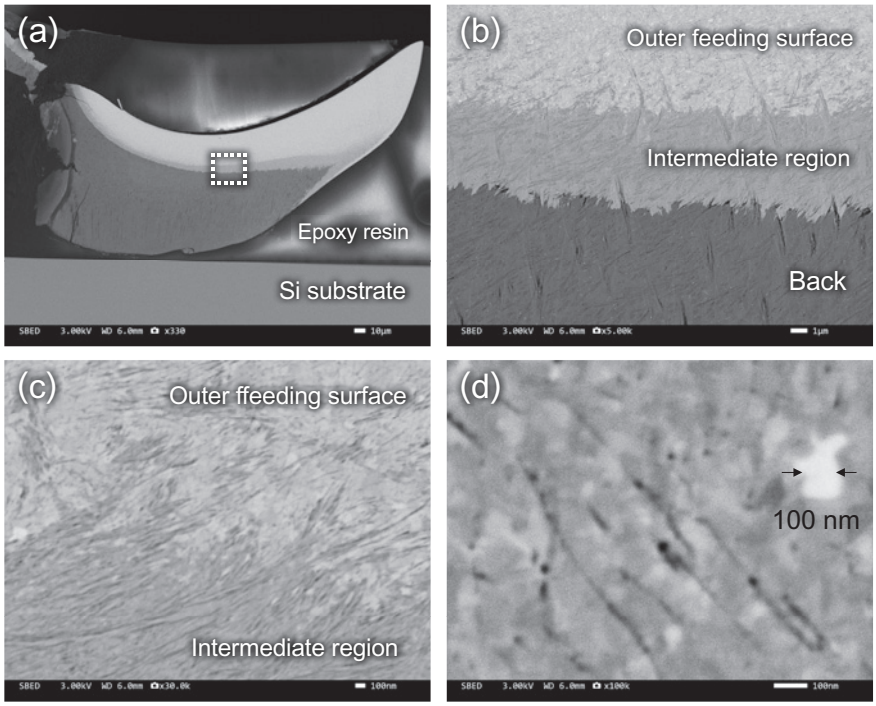

(a) Backscattered electron image of the entire tooth of chiton; (b) enclosed image by the dotted line in (a) (×5,000); (c) enlarged image in ×30,000; (d) further enlarged backscattered electron image of the boundary between the outer feeding surface and the Intermediate (×100,000).

measurements area was 10 × 18 μm^2 with a step size of 100 nm and the measurement time was 98 min.

The band contrast (BC) map is shown in Fig. 8 (b). A clear EBSD pattern was observed on the outer feeding surface, while few distinct EBSD patterns could be observed on the intermediate region and the back. From these results, it seemed to be elucidated that the components of the intermediate region and the back are very low crystalline and/or very small crystals which cannot form EBSD patterns. Although the component observed in the EBSD patterns of the outer feeding surface was identified as magnetite, it also has been revealed from inverse pole figures (IPFs) that the crystals of magnetite were oriented in the completely random directions and their domain size was less than 100 nm in the tooth of chiton (Fig. 8(c)). On the other hand, as shown in Fig. 1(d)(A), the FWHM of the XRD profile derived from Fe_3O_4 is enough sharp and cannot be judged to have a smaller size than a few tens of nm causing superparamagnetic behavior. The results of this EBSD were of great interest, because we initially thought that magnetite particle in the tooth of chiton was magnetically oriented and exhibited a domain structure according to the geomagnetic field due to its ferromagnetic property. It was considered that the magnetic orientation of the magnetite is inhibited by surface modification by organic substances during the formation of magnetite, and the fine particles of magnetite would be filled in randomly in living organism.

It was also found that there was the variation of diffraction intensity of magnetite within the outer feeding surface; the

Fig. 6 Elemental analyses by EDS carried out on the same specimen as measurement at BL14U.

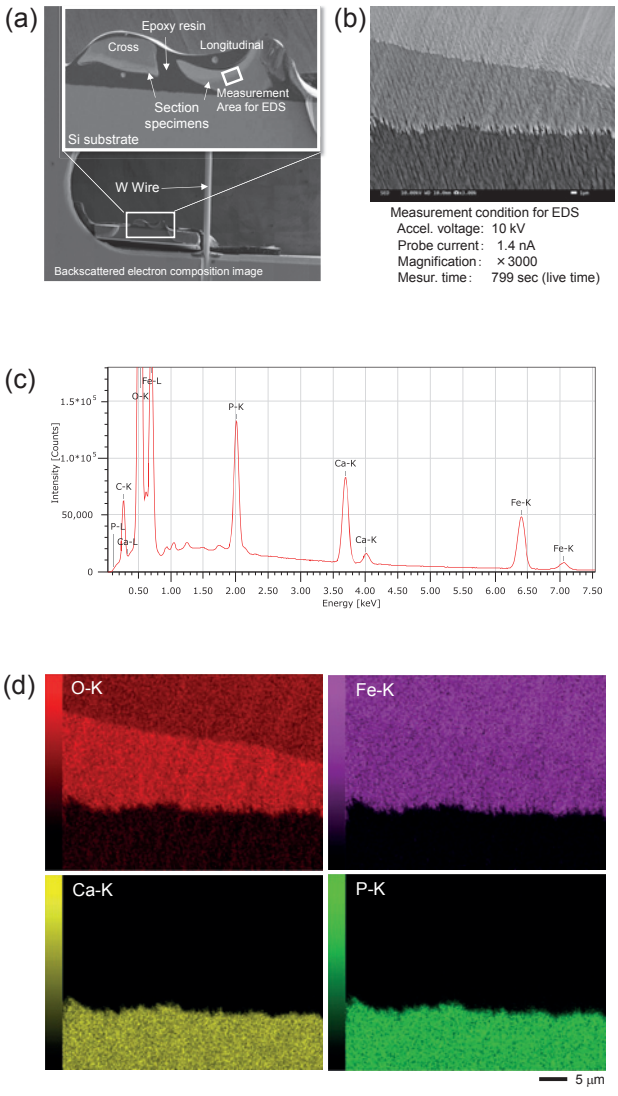

(a) Backscattered electron image of the specimen (Note that the top and bottom are reversed from Fig. 3(a).), (b) backscattered electron image of the region indicated by a rectangle in (a), (c) characteristic X-ray spectrum of the tooth of chiton measured with EDS while scanning (b), (d) elemental maps of oxygen, iron, calcium and phosphorus in the region indicated in (b) obtained by EDS.

Fig. 7 Elemental analyses by WDS carried out on the same specimen as measurement at BL14U.

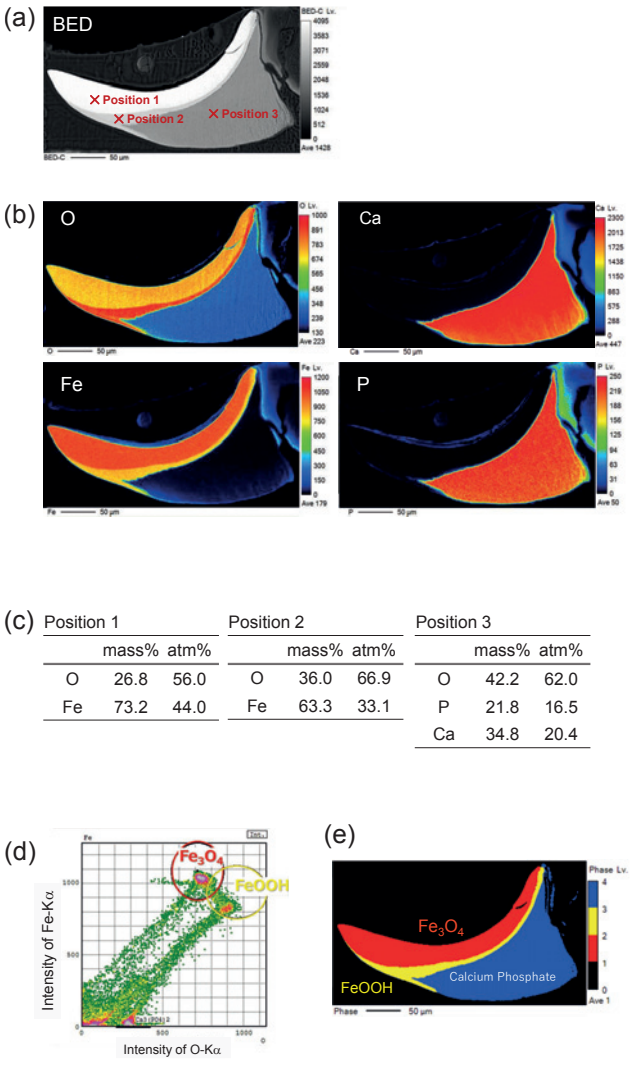

(c)

Position 1			Position 2			Position 3		
	mass%	atm%		mass%	atm%		mass%	atm%
O	26.8	56.0	O	36.0	66.9	O	42.2	62.0
Fe	73.2	44.0	Fe	63.3	33.1	P	21.8	16.5
						Ca	34.8	20.4

(a) Backscattered electron image of the whole sample (Note that the top and bottom are reversed from Fig. 3(a).), (b) elemental maps of oxygen, iron, calcium and phosphorus using WDS; (c) results of quantitative point analyses using WDS, three measurement points are shown in (a); (d) correlation plot of the O-Kα and Fe-Kα line intensities plotted from each measured point from map data; (e) Constituent maps (phase maps) in the longitudinal section of a tooth of chiton.

Fig. 8 EBSD analyses for a tooth of chiton.

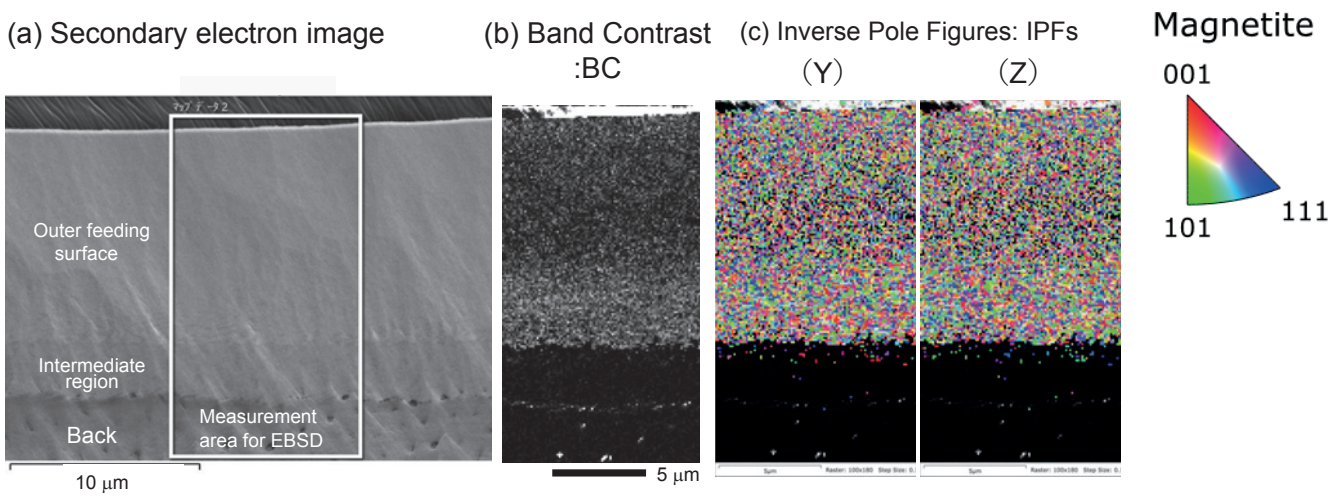

(a) Secondary electron image of a specimen of a tooth of chiton; (b) band contrast map obtained by EBSD performed on the area enclosed by the line in (a); (c) IPF diagram showing the orientation of the magnetite crystals.

diffraction intensity of about 1/3 region of the outer feeding surface close to the intermediate region was larger than that of other 2/3 region (Fig. 8 (b) (c)). It could be considered that there were differences in the domain size of magnetite crystals causing electron diffraction in the outer feeding surface. It is very interesting that elemental analysis with WDS showed that the feeding surface appeared to be homogeneous, but electron diffraction showed differences in the size of magnetite crystals. High spatial resolution domain analysis by EBSD indicated a characteristic distribution of magnetite crystal sizes in the outer feeding surface which seemed to be homogeneous by elemental analysis with WDS. In future, we would like to perform further analyses by using transmission-type EBSD in order to evaluate the formation process of magnetite in the teeth of chiton.

Summary

X-ray analyses carried out at BL14U, Nano Terasu, and several analyses by an electron beam at JEOL provided a very large amount of scientific information from the teeth of chiton, however, it would be very hard to perform them in maximum performance levels without the outstanding sample preparation techniques developed over many years by the JEOL staff. In particular, highly advanced techniques were essential for the preparation of small specimens with complex shape, such as a tooth of chiton, to fix the sample with epoxy-resin to a desirable direction to be measured manually, to hold a sample plate to collect direction during CP processing to produce the optimum sample surface. Furthermore, it is worth of mentioning that JEOL members fabricated the special sample holder for carrying out both of measurements with the scanning soft X-ray microscopy system at Nano Terasu and several analyses by an electron beam at JEOL on the same sample. The numerous devices and techniques for the sample preparations created in this study were so important not only to obtain such brilliant data but also are expected to great benefit to users of the system at BL14U in the future, which handles images in the 60 × 60 μm^2 range, having good fits for electron microscopic analytical technique.

In addition, if some devices will be installed in the sample chamber at BL14U in order to visualize the position of the sample and the synchrotron radiation, the efficiency of measurement would be increasing dramatically. With the cooperation of JEOL, the system would be more user-friendly in near future.

Acknowledgement

The authors would like to thank Professor Tetsuya Nakamura, International Synchrotron Radiation Innovation and Smart Research Centre, Tohoku University, Principal researcher Yoshinori Kotani and, Research Fellow Akiho Sumiyoshiya, Photon Science Innovation Center, Professor Masami Terauchi, Institute of Multidisciplinary Research for Advanced Materials, Tohoku University, for their valuable advice in conducting the soft X-ray scanning microscopy analysis of the nano-terrace BL14U.

We would also like to thank Mr Hirofumi Morita of Oxford Instruments Ltd. for his assistance with the EBSD measurements of the tooth tongue cross section, which has a small grain size and is susceptible to electron beam damage.

References

[1] The Iron Oxides: Structure, Properties, Reactions, Occurrences and Uses, Second Edition, Cornell and Schwertmann, Wiley-VCH Verlag GmbH (2003) ISBN.

[2] T. Ishii, K. Okoshi, T. Otake and M. Nakahara, *Nippon Suisan Gakkaishi* **58** (1992) 1285.

[3] Chiya Numako, Yoshiyuki Tsukiyama and Kichiro Koto, Characterisation of Iron Components in the Radula of the Japanese Chiton *Acanthopleura japonica, VENUS* **65** (1-2) 153-163 (2006).

Time-Resolved ESR Method for Observing Rapid Radical Reactions

Atsushi Kajiwara Nara University of Education

Time-resolved electron spin resonance (time-resolved ESR, TR ESR) is a technique for observing rapid radical reactions. In this method, the relaxation process of anomalous polarization of electron spins of radicals induced by laser pulses is directly detected as an ESR signal without magnetic field modulation and observed with a time resolution of several tens of nanoseconds. This allows for the selective observation of the initiation process of radical polymerization, which cannot be observed by ordinary ESR measurement (steady-state ESR, SS ESR). Furthermore, this method provides information on the detailed structure and reaction kinetics of radical addition reactions by clearly observing the spectra of chain-initiating radicals in polymerization systems of various monomers. It is also possible to obtain information on the direction of addition of monomers with asymmetric structures and to study which monomer is added preferentially in copolymerization systems. Conventionally, obtaining such information from ESR spectra during radical polymerization has been very difficult, sometimes even impossible. Significantly, observing monomers containing nitrogen posed a notable challenge. To overcome this difficulty, an apparatus capable of temperature-variable flow measurement developed, enabling the observation of the spectrum of chain-initiating radicals through time-resolved ESR in specific systems. A key advantage of time-resolved ESR is its capacity to study the formation mechanism of transient paramagnetic species. The utilization of time-resolved ESR is anticipated to propel research endeavors concerning the correlation between radical reactions and electron spin state.

Introduction

Electron spin resonance (ESR) is a magnetic resonance spectroscopy method analogous to nuclear magnetic resonance (NMR). However, the targets of observation differ significantly. In the radical polymerization reaction, the focal point of this study, radical polymerization signifies a reaction in which monomers, derived from petroleum, are sequentially added with radicals of chemical species bearing unpaired electrons as reaction-active species to yield polymers (macromolecules) interconnected by extended chains. As illustrated in **Fig. 1**, ESR and NMR play distinct roles in observing this reaction. While NMR facilitates detailed structural analysis of the raw monomer (starting material) and the product polymer (resulting material) [1], ESR offers the unique capability to observe the radicals, the active species produced during the reaction. The concentration of these active species ranges from 10^{-6} M to 10^{-7} M, which is approaching the detection limit of the ESR spectrometer. These species are transient and unstable, making the observation of their spectra challenging. However, this challenge can contribute to a more profound understanding of chemical reactions. The combination of NMR and ESR provides a comprehensive understanding of the radical polymerization reaction and facilitates the acquisition of more detailed information regarding the intermediate states of the reaction.

In the study of radical polymerization, ESR can be applied in various ways, including steady-state ESR, which primarily observes propagating radicals, high-pressure ESR, which can observe high-pressure polymerization systems, electrochemical ESR, which can measure the redox potential of radicals, and other methods that can all deeply penetrate the chemical properties of radicals [2-6]. Among these techniques, time-resolved ESR has emerged as a particularly noteworthy approach, enabling the observation of rapid radical reactions [7, 8]. This paper will primarily focus on the intricacies and applications of time-resolved ESR.

Observation of Radical Polymerization Reaction by ESR

As demonstrated in **Fig. 2**, radical polymerization reactions consist of a combination of elementary reactions, including initiation, propagation, termination, and chain transfer [9]. Radical polymerization reaction occurs when initiator, monomer, and solvent are placed in a sample tube and heated in the cavity of the ESR spectrometer or irradiated with light from the outside. Direct observation of the radical polymerization reaction in the sample tube allows the ESR spectrum of the propagating radicals to be observed. Despite the complexity of the measurement, the acquisition of high-resolution spectra at elevated sensitivity, achieved through the optimization of diverse experimental conditions, holds considerable promise. This approach promises to yield a wealth of information, including concentration, dynamic behavior, reactivity, and the detailed structure of propagating radicals. The steady-state ESR spectra of radicals produced during radical polymerization, including various propagating radicals along with their hyperfine splitting

〉〉 Takabatake-cho, Nara, 630-8528, Japan | E-mail: kajiwara@cc.nara-edu.ac.jp

Fig. 1

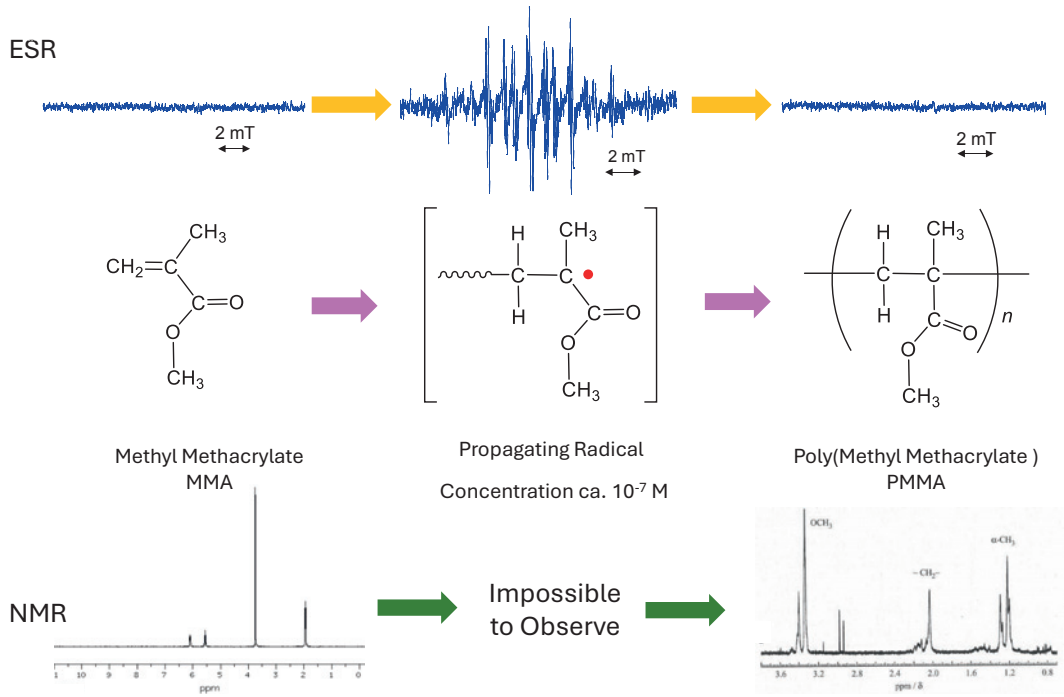

Results of ESR and NMR observations of the reaction of methyl methacrylate (MMA) radical polymerization to form poly(methyl methacrylate) (PMMA) [1]. However, the propagating radicals formed during the reaction cannot be observed without ESR.

Fig. 2 Elementary reaction process of radical polymerization.

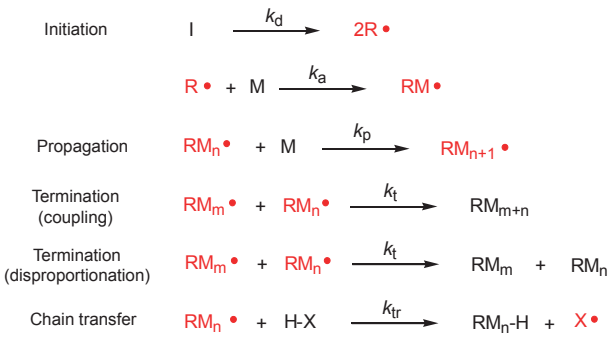

constants, have been previously reported in JEOL News [10]. The absolute value of the hyperfine splitting constant can be estimated with a high degree of accuracy, and it is proportional to the spin density, which is closely related to the electronic state, allowing for a detailed discussion of the properties of radicals. Given the preeminent role of electrons in chemical phenomena, the insights gleaned from direct electron observation are helpful in elucidating the fundamental principles of chemistry.

Experimental Section

The initiators Diphenyl (2,4,6-trimethylbenzoyl)phosphine Oxide (TMDPO) (Wako Pure Chemicals) and Phenylbis(2,4,6-trimethylbenzoyl)phosphine Oxide (PBTPO) (Tokyo Chemical Industry, TCI) were recrystallized from ethanol. Lithium Phenyl(2,4,6-trimethylbenzoyl) phosphinate (LiTPO) (TCI) was utilized in its original state. Prior to use, all monomers were subjected to a purification process. Time-resolved ESR was measured on a JEOL JES-RE2X ESR spectrometer, JES-TE200 ESR spectrometer, or JES-X320 ESR spectrometer with the wide-band preamplifier ES-WBPA2 or ES-WBPA4. Digital oscilloscopes such as Tektronix TDS 520A, TDS 540D, or MDO-3032 Mixed Domain Oscilloscope were utilized. Flow measurements were conducted using a specially designed quartz cell with a Tokyo Rika (EYELA) MP-2000 microtube pump pumping liquid at 20 mL/h. Tubes were Versilon (Fluran) (1.15 mm inner diameter × 3.2 mm outer diameter). Variable temperature measurements were obtained with the aid of a JEOL ES-DVT2 or ES-13060DVT5 variable temperature device, while the temperature within the flow cell was gauged using a 0.5 mm × 400 mm temperature sensor affixed to an Anritsu Instrument HFT-40 thermometer. Subsequent data analysis was conducted with the utilization of JEOL's CIDEP analysis program, complemented by simulations performed employing the JEOL program. The laser utilized was a Continuam Surelite-I Nd:YAG laser at the third harmonic 355 nm (10 mJ/flash at 355 nm with a 6-ns fwhm).

Time-resolved ESR

Time-resolved ESR (TR ESR) is an ESR measurement method with a time resolution of tens of nanoseconds. It is used to observe rapid radical reactions that cannot be observed by conventional ESR measurements. In the commonly used steady-state ESR (SS ESR), the signal-to-noise ratio (S/N ratio) can be improved by applying a 100 kHz magnetic field modulation, which also increases the resolution. Consequently, the spectrum becomes differential. However, it is impossible in principle to observe radical reactions faster than 100 kHz (ca. 10^{-4} sec) because of the 100 kHz magnetic field modulation. To address this limitation, a method has been developed that allows for the observation of only the radical formation by initiator cleavage and the reaction in which the formed radical adds to the first

monomer to form a chain-initiating radical, even when observing the same radical polymerization system. This approach is known as time-resolved ESR. The time-resolved ESR method necessitates the use of a pulsed laser, such as an Nd: YAG laser, a broadband preamplifier, and a digital oscilloscope. A brief diagram of the time-resolved ESR equipment is shown on **Fig. 3**. The signal is extracted directly through the broadband preamplifier without undergoing magnetic field modulation. The unpaired electrons of the radicals generated from the initiator cleaved by the laser pulse cause an anomalous electron spin polarization in a magnetic field, and the process of relaxation of the polarization into a Boltzmann distribution is observed as the ESR signal. In this case, the measurement system is generally not in thermal equilibrium, and an abnormally strong absorption (A) or emission (E) of microwaves is observed due to the spin polarization. This phenomenon is referred to as Chemically Induced Dynamic Electron spin Polarization (CIDEP), and the resulting spectrum is a time-resolved ESR spectrum. Despite the challenges in quantifying the detected radicals due to this anomalous polarization, CIDEP possesses the notable capability of detecting radicals even at low radical concentrations. This property is instrumental in facilitating the study of the structure and formation mechanism of transient paramagnetic species [11].

1. Initial Process of Radical Polymerization

1.1. Formation reaction of chain-initiating radicals and its kinetics

The time course of the radical polymerization reaction and the observation of the chain initiating and propagating radicals corresponding to the respective reaction times are summarized in **Fig. 4**. The initial stage of the radical polymerization system of *tert*-butyl methacrylate with acylphosphine oxide initiators, such as TMDPO, was observed in the time. The time-resolved ESR spectrum is displayed in three dimensions in the center of the figure, with the ESR signal intensity on the vertical axis, the magnetic field on one axis, and reaction time on the other. When the three-dimensional spectrum is sliced at a fixed time, a spectrum with the magnetic field on the horizontal axis (lower left of Fig. 4) is obtained. This spectrum is due to the chain initiating radical. From this spectrum, information on the structure and dynamic behavior of the radicals can be obtained. The structural formula is displayed in the upper left corner of the spectrum. In this particular instance, the spectral lines are all upward, indicating that microwave absorption occurs during the electron spin relaxation process. In some cases, microwave emissions occur, in which case the spectral lines appear below the baseline (see Fig. 6 and Fig. 10). While the spectrum of propagating radicals observed in steady-state ESR is in differential form, time-resolved ESR provides an upward (Absorption, A) or downward (Emission, E) integral form of the spectrum because the time resolution is enhanced by not modulating the magnetic field at 100 kHz. When sliced the three-dimensional spectrum in a constant magnetic field, the horizontal axis is time, and the generation and decay of each spectroscopic line can be observed (lower right of Fig. 4). Lines in blue and orange are shown. The blue line of the decay line is attributed to the phosphorus-centered radical, while the orange line is attributable to the signal of the chain-initiating radical that is introduced by the initial monomer. The rate constant of the radical addition reaction and the activation energy of the reaction can be estimated from the decay spectrum of the phosphorus-centered radical [12-15]. This corresponds to the second radical addition reaction from the top of the elementary reaction process in Fig. 2, in which an initiating radical adds to the first monomer to form a chain-initiating radical. Although the rate constants and activation energies of radical addition reactions have been estimated by laser flash photolysis, a feature and advantage of time-resolved ESR is that it also provides information on the structure and dynamic behavior of the active species.

Fig. 3

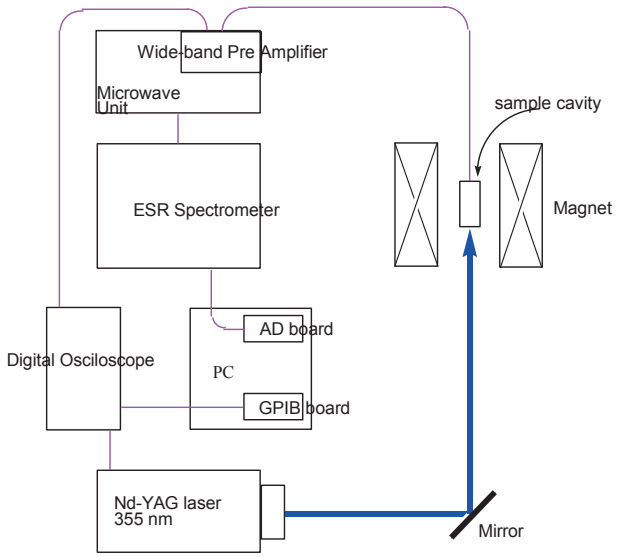

The configuration of the measurement system for time-resolved ESR, which includes an ESR spectrometer, a pulsed laser, a digital oscilloscope, a wide-band preamplifier, and other necessary components.

1.2. Observation of the second monomer addition

As previously mentioned, a salient feature of time-resolved ESR is its capacity for selective observation of the formation of chain-initiating radicals, thereby enabling estimation of the rate constants and activation energies of the reactions. In the present study, which focused on the reaction kinetics of the initial polymerization process, only two cases have been documented in which addition reactions to the second monomer and their rate constants were observed. The studies conducted by Mizuta and Kuwata [16, 17] observed a second addition step for methyl methacrylate (MMA) and isoprene, respectively. The use of acylphosphine oxide as an initiator facilitates the discernment of the spectrum of chain-initiating radicals due to the observation of substantial splitting by the phosphorus nucleus of the initiator fragment. In contrast, no splitting by the phosphorus nucleus is evident when two or more monomer units are linked together. Notably, while the measurement was presumably challenging, the result is of paramount importance for the study of reaction kinetics.

1.3. Chain Initiation Radicals of Various Monomers

Time-resolved ESR has been demonstrated to facilitate the observation of the initial stages of polymerization. In addition to this capability, it has also been shown to provide a variety of information regarding the nature of radicals, which are the active species in the polymerization process. Furthermore, time-resolved ESR has been demonstrated to be applicable not only to monomers with high polymerizability but also to monomers with various polymerizabilities. Examples of measurements are shown in **Fig. 5**, and Fig. 5a-f show monomers for which the ESR spectra of the propagating radicals can be observed

Fig. 4 The reaction is quantifiable through the use of time-resolved ESR.

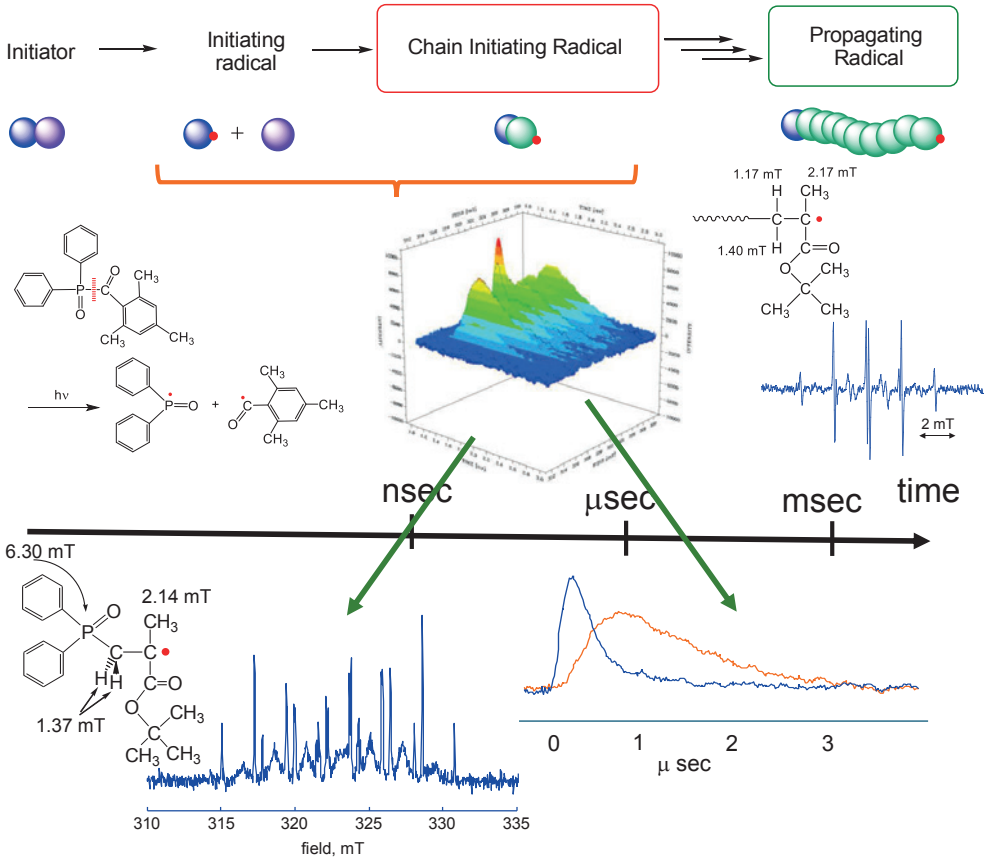

The initiator undergoes cleavage, forming a radical that subsequently adds to the first monomer, thereby generating a chain-initiating radical. In the context of an actual reaction system, polymerization persists in forming propagating radicals; however, the exclusive observation of the initial stage is possible through the implementation of time-resolved ESR. As an illustration, a three-dimensional display of the time-resolved ESR spectrum of the chain initiating radical of *tert*-butyl methacrylate is presented in the center. The vertical axis corresponds to the ESR signal intensity, while the horizontal axis represents the magnetic field and reaction time. The time dependence of the signals of the phosphorus-centered (in blue) and chain-initiating radicals (in orange, in the lower right corner), in conjunction with the spectrum of the chain-initiating radical (in the lower left corner) and the structure of the chain-initiating radical, is displayed.

by steady-state ESR. Figure 5e corresponds to the spectrum of the chain initiating radical of *N*-Vinylcarbazole, in which the splitting by the nitrogen nucleus is obscured by the line width. This observation signifies that the spin density is delocalized throughout the carbazole ring. The absence of visibility of the splitting by the nitrogen nucleus near the radical is only discernible through the observation of such a spectrum. As illustrated in Fig. 5g and 5h, the monomers exhibit suboptimal single-step polymerizability. However, the spectra of chain-initiating radicals are distinctly discernible, suggesting that the initial step of addition occurs without complications. The observed poor polymerizability is hypothesized to be attributable to subsequent steps, rather than the initial addition step. While time-resolved ESR spectra are reported to have lower resolution compared to steady-state ESR spectra, the spectra obtained in this study, demonstrate a resolution that is comparable to that of the propagating radicals observed in steady-state ESR [10, 13-15].

Furthermore, time-resolved ESR can provide information on the direction of radical addition by observing time-resolved ESR spectra of vinyl monomers with asymmetric structures. In the case of copolymerization reactions, time-resolved ESR can be measured in a system in which two or more monomers coexist to obtain information on which monomer is prioritized for addition.

2. Spin States of Radials from Photo Radical Initiators

As shown in **Fig. 6**, the time-resolved ESR spectra of various photo-radical initiators are depicted. Figure 6a and 6b are acylphosphine oxides and Fig. 6c is acylphosphinate. These are photo radical initiators generated both phosphorous centered and carbon centered radicals by cleavage of P-C bond under irradiation. In Fig. 6a-c, the time-resolved ESR spectra of acylphosphine oxide initiators, such as TMDPO, are all upward-sloping, indicating that microwave absorption (A) occurs during the electron spin relaxation process. The radicals produced by the cleavage are phosphorus-centered radicals and carbon-centered radicals. The carbon-centered radicals in Fig. 6a-c are the same radicals in these cases, but the structure of the phosphorus-centered radical is different. The hyperfine splitting constant of the phosphorus nucleus differs depending on the electronic state of the radical. Depending on the formation mechanism of the radicals, microwave emission may occur, in which case the spectral line will emit downward from the baseline. In Fig. 6d-f, some examples are shown where a downward spectrum can be observed. As demonstrated in Fig. 6d and 6e, the occurrence of isopropyl radicals is observed in both cases. Figure 6d illustrates the formation of isopropyl radicals through hydrogen abstraction from isopropyl alcohol by benzophenone, while Figure 6e shows the process involving initiator cleavage. Figure 6e depicts the observation of isopropyl

Fig. 5 Examples of time-resolved ESR spectra of various monomers with TMDPO as initiator.

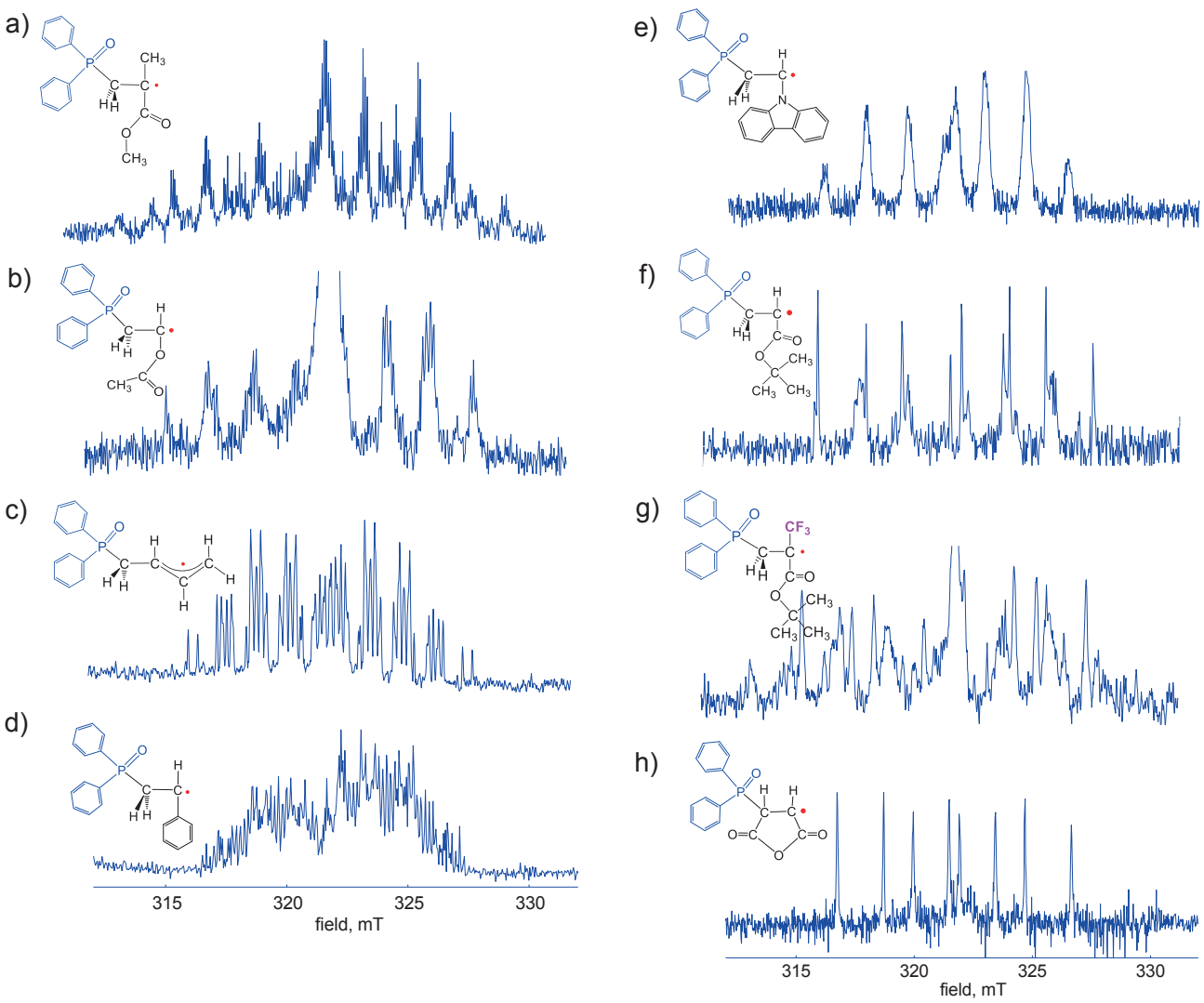

a) MMA, b) vinyl acetate, c) 1,3-butadiene, d) styrene, e) *N*-Vinylcarbazole, f) *tert*-butyl acrylate, g) CF_3 substituted *tert*-butyl methacrylate, and h) maleic anhydride.

radicals produced by covalent bond breaking in the total emission (E) type. In contrast, Fig. 6d shows the production of radicals through the abstraction of benzophenone, resulting in emission and absorption (E/A) patterns observed from the low-field side. Figure 6f presents the time-resolved ESR of radicals from 2,2'-azobis(isobutyronitrile) (AIBN), a general-purpose initiator for conventional radical polymerization. In the case of AIBN, the absorption and emission (A/E) patterns are observed from the low-field side, reflecting differences in the spin state at the time of radical formation. This phenomenon has been thoroughly investigated in the AIBN system by Murai et al. [18, 19]. It should be noted that such information cannot be obtained by steady-state ESR; however, it can be acquired by time-resolved ESR.

Improvement of Sensitivity of Time-Resolved ESR Measurement

As summarized in **Fig. 7**, the figure presents a series of time-resolved ESR spectra of chain-initiating radicals and steady-state ESR spectra of propagating radicals of various monomers that have been documented thus far. While the observation of both steady-state ESR spectra of propagating radicals and time-resolved ESR spectra of chain-initiating radicals of hydrocarbons, (meth)acrylates, dienes, and vinylesters has been documented, the observation of propagating radicals of monomers containing nitrogen atoms by steady-state ESR remains particularly challenging, with only a limited number of successful cases reported. Furthermore, the observation of time-resolved ESR spectra has been limited until recently, which may be attributed to the faster relaxation of nuclear spins by nitrogen atoms compared to carbon and oxygen atoms, resulting in increased instability of the added radicals. To enhance the sensitivity and resolution in the observation of such radicals containing nitrogen atoms, a modification of the apparatus was undertaken to enable temperature-variable flow measurements. The thermocouple component situated at the base of the L-shaped duplex quartz tube of the variable-temperature adapter underwent modification to facilitate the installation of an extended, slender, specially

Fig. 6 Time-resolved ESR spectra of radicals generated from various photo-radical initiators only.

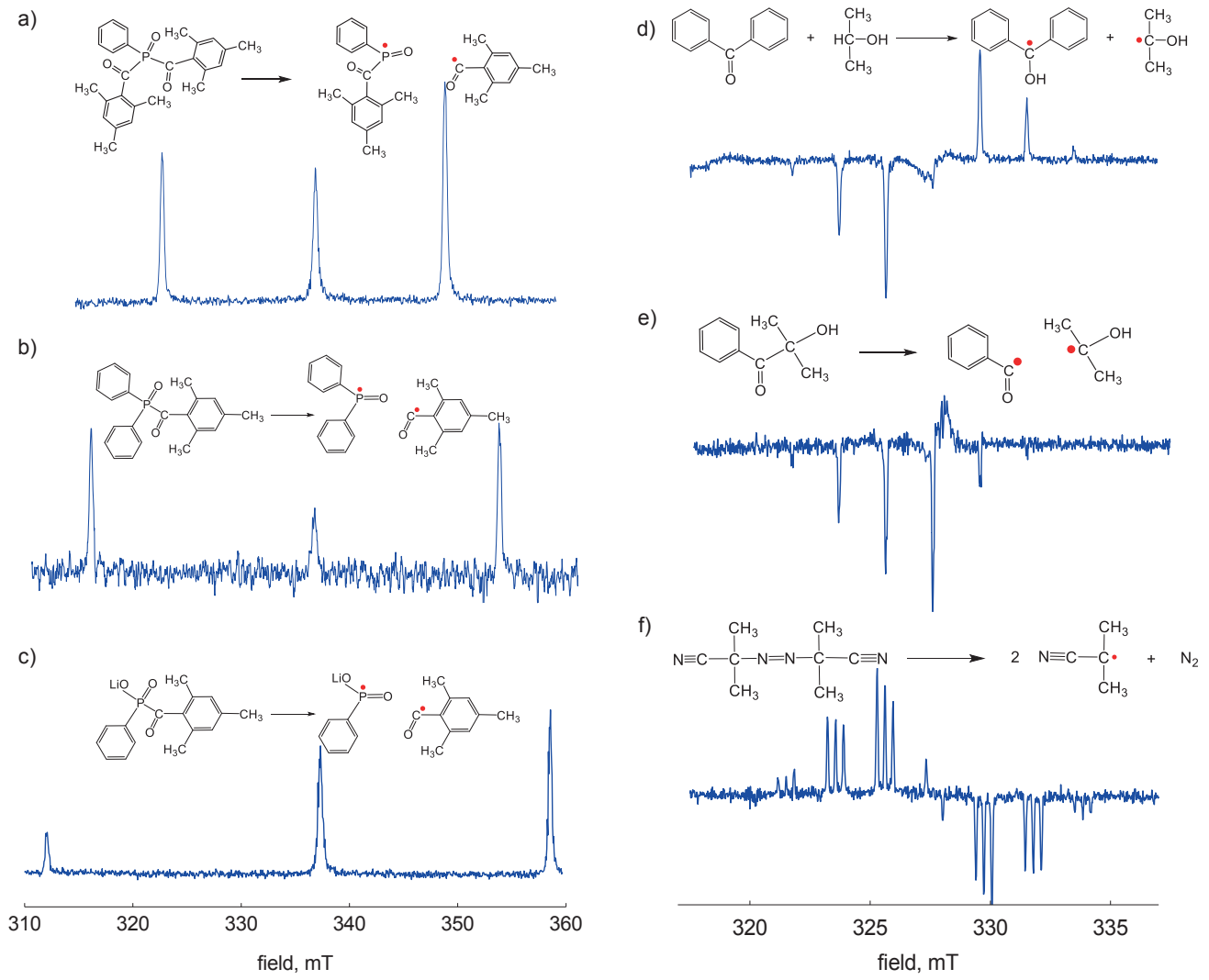

a) Phenylbis(2,4,6-trimethylbenzoyl)phosphine oxide (PBTPO) b) Diphenyl(2,4,6-trimethylbenzoyl)phosphine oxide (TMDPO)
c) Lithium phenyl(2,4,6-trimethylbenzoyl)phosphinate (LiTPO) d) Benzophenone + isopropanol e) 2-Benzoyl-2-propanol and f) 2,2'-Azobisisobutyronitrile (AIBN).

designed cell (exceeding 400 mm) by penetrating the upper and lower extremities of the tube. The custom-made cell under consideration has been crafted to resemble the JEOL aqueous solution cell, with the top and bottom portions extended to a greater extent. The central region of the cell is a flat plate cell, a configuration that facilitates the utilization of polar solvents characterized by substantial dielectric loss. The temperature of the sample solution under observation was determined by inserting a wire thermocouple (0.5 mm in diameter and 400 mm in length) into the flow tube, such that it extended toward the center of the cell. The correlation between the temperature displayed by the temperature variable and the actual temperature measured was investigated. At the lowest flow velocity, a strong correlation was observed between the temperature indicated on the temperature variable and the actual temperature. However, at higher flow rates, a discrepancy emerges between the temperatures displayed and measured. Nonetheless, this discrepancy can be effectively compensated for.

Figure 8 demonstrates the implementation of the flow method yielded enhanced outcomes. As illustrated in Fig. 8 (lower right), the results of the flow measurement revealed the initiator-derived spectrum at the beginning of the measurement in the system not subject to flow. However, subsequent to this initial observation, the spectrum became undetectable (left side of Fig. 8). On the other hand, when a sample solution of equivalent composition was employed in the flow measurement, the spectrum manifested a signal intensity so pronounced that it traversed the vertical axis. The effect of the flow measurement is evident, as new solutions flow in sequentially, reacting with the laser pulse, and generating fresh radicals. This continuous generation of radicals is believed to underpin the sensitivity of the spectra. Utilizing this method, the signals of chain-initiating radicals from other monomers containing nitrogen atoms could also be observed successively (see Fig. 9). In contrast, in other radical reaction systems, it has been observed that the observed radical species undergo changes when the flow rate is altered. Consequently, further development of this method is anticipated, including its application to reaction kinetics.

Fig. 7 List of propagating radicals and chain-initiating radicals observed to date.

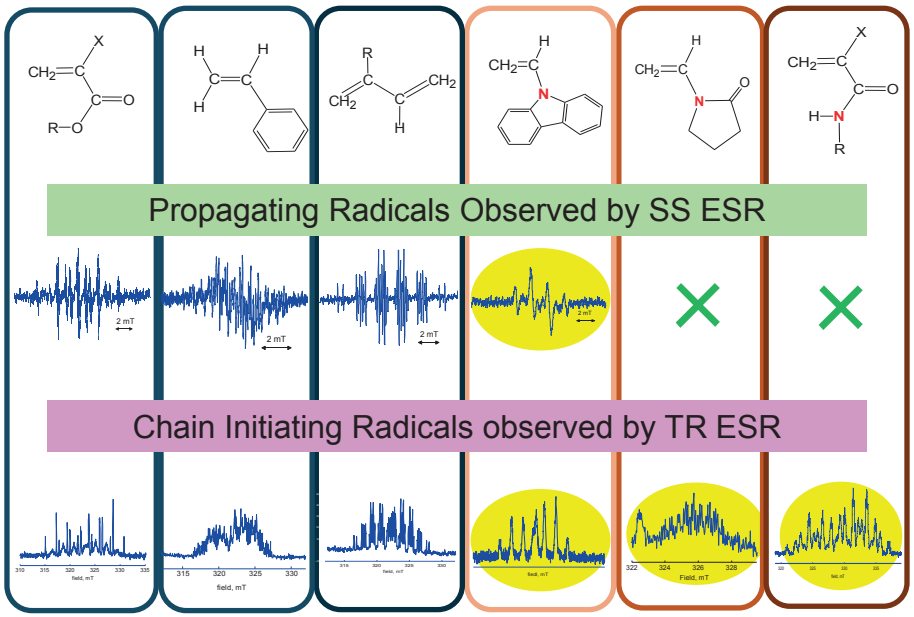

Radicals that have been measured are indicated by their spectra. Radicals that have not yet been measured are indicated with an "X". Although both propagating radicals and chain initiation radicals have been observed for hydrocarbons, dienes, (meth)acrylates, and vinyl esters, both are difficult to observe for monomers containing nitrogen. In recent years, time-resolved ESR spectra have finally become available, and propagating radicals can be observed for some of them. While significant strides have been made in the observability of time-resolved ESR spectra for certain monomers containing nitrogen, numerous others remain challenging to analyze due to the absence of discernible propagating radicals.

Fig. 8 The reaction scheme and time-resolved ESR spectra of chain-initiating radicals of *N*-vinylpyrrolidone using TMDPO as the initiator are shown.

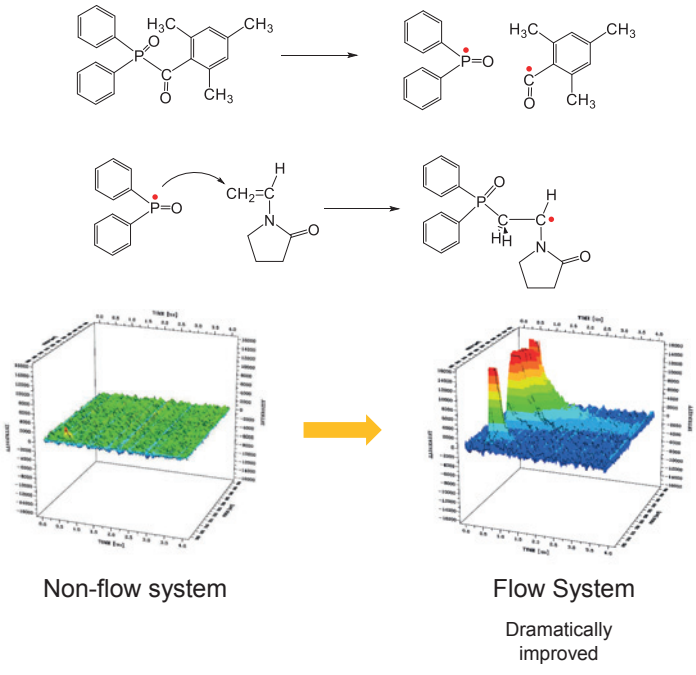

A 30-mL solution of 0.05 M initiator, 0.1 M monomer, and toluene as a solvent was prepared. The 0.4 mL of the solution was placed in a 5-mm outer-diameter sample tube (left). The static method, employing a sample tube alone, yielded negligible signal (left). Then, the same solution was pumped using Tokyo Rika (EYELA)'s MP-2000 microtube pump (right). The implementation of the flow method resulted in the observation of a signal sufficiently robust to induce overflow (right).

Various Time-Resolved ESR Spectra

The following examples illustrate the utility of new initiators and flow methods in facilitating more sensitive measurements. The observation of radical polymerization reactions in aqueous solution has posed significant challenges for both time-resolved and steady-state ESR measurements. This is due to reduced sensitivity resulting from dielectric loss caused by water in the solvent, as well as the scarcity of effective water-soluble initiators. However, recent advancements in the field have led to the commercial availability of water-soluble acylphosphinates, which has significantly impacted this area of research. **Figure 9** presents a time-resolved ESR spectrum of chain-initiating radicals of methacrylamide, demonstrating the efficacy of the flow method employing water-soluble acylphosphinates (LiTPO) as initiators in producing a high-resolution spectrum. This method has been shown to offer enhanced sensitivity compared to traditional techniques and initiators. Similar observations have been made

Fig. 9

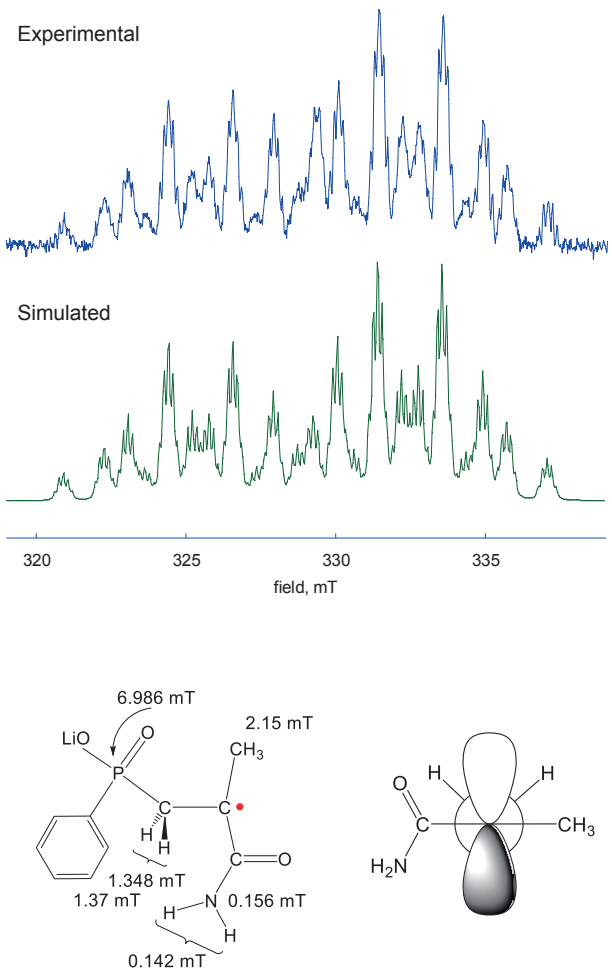

The time-resolved ESR spectra of chain-initiating radicals of methacrylamide in an aqueous solution with water-soluble acylphosphinate (LiTPO) as initiator are presented. The experimental spectra (top in blue) and the simulated spectra (bottom in green) at 20 °C using the flow method are shown. The structural formula of the observed radicals, along with their hyperfine coupling constants, is presented at the bottom of Fig. 9.

in aqueous acrylamide solution systems, further validating the effectiveness of this approach. As illustrated in **Fig. 10**, two characteristic instances of chain-initiating radicals have been measured by time-resolved ESR utilizing photo-radical initiators. As demonstrated in Fig. 10, two distinctive instances of chain-initiating radicals have been measured by time-resolved ESR utilizing photo-radical initiators. Figure 10a presents the overlapped time-resolved ESR spectra of both initiating and chain-initiating radicals of *tert*-butyl methacrylate with PBTPO as initiator. Figure 10b presents the overlapped time-resolved ESR spectra of *tert*-butyl acrylate with 2-benzoyl-2-propanol as initiator. The flow method is also more sensitive for these measurements. As illustrated in Figure 10a, the initiator signal demonstrated an absorptive (A) type, while the chain-initiating radical signal also exhibited an absorptive spectrum. Conversely, when the initiator signal manifested an emissive (E) type (Fig. 10b), the signal of the chain-initiating radicals exhibited an emissive (E) type. This outcome signifies the transfer of the electron spin polarization of the initiator radicals to the chain-initiating radicals.

Conclusion

The present study describes the time-resolved ESR method as a means of observing rapid radical reactions. The spectra of chain-initiating radicals can be clearly observed in polymerization systems of various monomers. In addition to obtaining detailed structural information, the reaction kinetics of radical addition reactions can also be studied. As shown in Fig. 6, the spectrum of the photo-radical polymerization initiator solution also reflects the spin state of the radical. Another salient feature of this technique is its capacity to provide experimental evidence for spin states that have been conventionally postulated in the domains of photochemistry and radical chemistry. It is anticipated that this information will serve as a foundational basis for further research endeavors investigating the relationship between the spin state of unpaired electrons in radicals and the chemical reactions of radicals, a subject that has received scant attention in extant research.

Acknowledgements

The author would like to express his sincere gratitude to Professor Emeritus Mikiharu Kamachi of Osaka University for his invaluable contributions to the field, particularly in the realm of research guidance. Dr. Masahiro Kohno, who was formerly working for JEOL, offered pivotal insights and assistance with experimental techniques for the direct detection of propagating radicals by ESR. Professor Krzysztof Matyjaszewski of Carnegie Mellon University provided invaluable insights into general research discussions. Professor Emeritus Yotaro Morishima of Osaka University graciously imparted his comprehensive guidance on laser techniques for time-resolved ESR measurements. Professor Emeritus Jun Yamauchi of Kyoto University offered insightful commentary on various aspects of ESR spectroscopic interpretation, Professor Emeritus Hisao Murai of Shizuoka University provided invaluable guidance, especially on the interpretation of time-resolved ESR spectra, Professor Emeritus Keiji Kuwata of Osaka University offered encouragement and guidance on various aspects of ESR research, and Professor Hiroyuki Aota of Kansai University provided practical advice on variable temperature flow measurements. Dr. Yukio Mizuta and the entire JEOL team provided invaluable guidance on a wide range of topics, including the operation of the ESR spectrometer and the execution of measurements. The author extends his profound gratitude to them.

References

[1] ^{1}H NMR of MMA monomer: SDBS: https://sdbs.db.aist.go.jp/, National Institute of Advanced Industrial Science and Technology, 26 Jan. 2025. ^{1}H NMR of PMMA: Hatada, K., Kitayama, T., *NMR Spectroscopy of Polymers*, Springer (2004).
[2] Yamauchi, J., *Magnetic Resonance –ESR, Science Publishers*, Tokyo, JAPAN (2006).
[3] Society of Electron Spin Science and Technology (SEST) ed., *Introduction to Electron Spin Science & Technology*, Yoneda Publications, Chiba, JAPAN (2010).
[4] Ohba, H., Yamauchi, S., *Electron Spin Resonance Spectroscopy*, Kyoritsu Publishers, Tokyo, JAPAN (2017).
[5] Weil, J. A., Bolton, J. R., *Electron Paramagnetic Resonance, Elementary Theory and Practical Applications*, 2nd ed. John Wiley & Sons, Inc.: Hoboken, New Jersey, pp. 345-348 (2007).
[6] Kamachi, M., *Adv. Polym. Sci*., **82**, 207-275 (1987).

Fig. 10

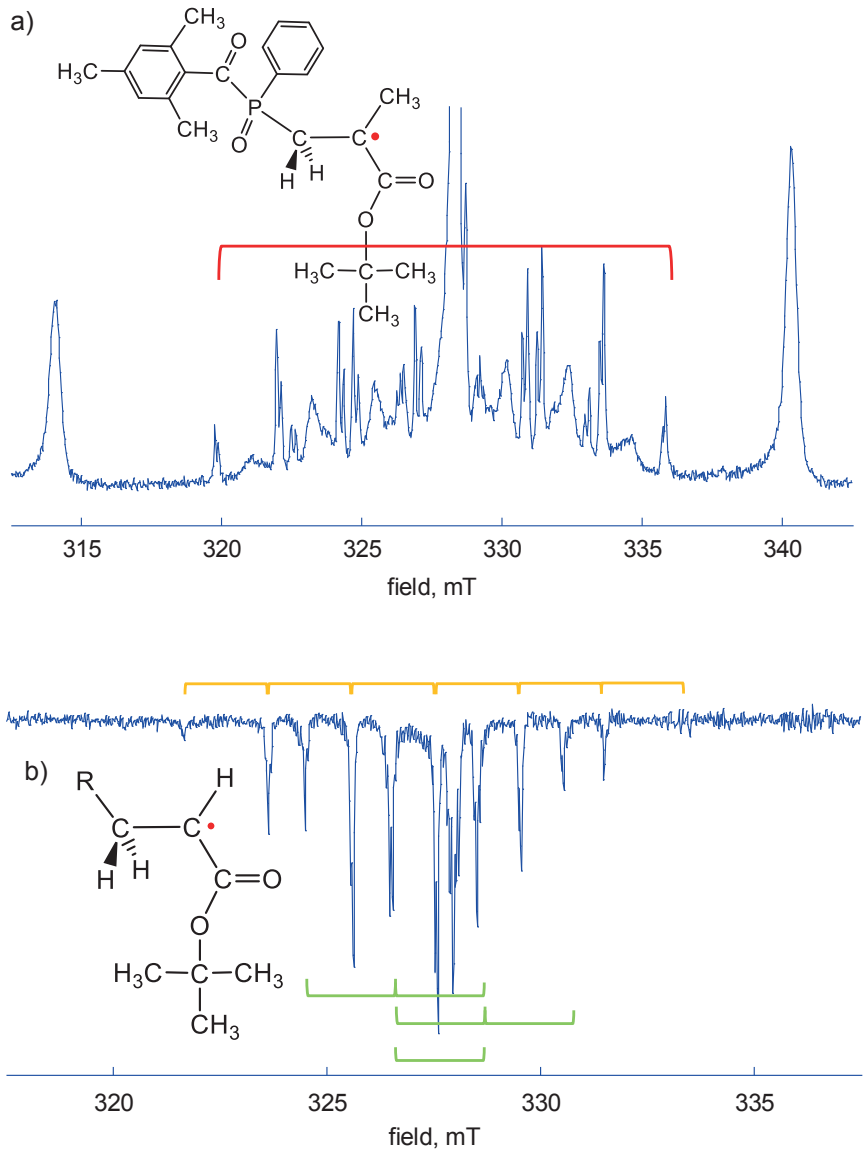

a) Time-resolved ESR spectra of chain-initiating radicals of *tert*-butyl methacrylate along with phosphynoyl and carbon centered radicals generated from initiator, PBTPO, were observed. It was noted that all spectra were of the absorption type (A). b) The time-resolved ESR spectra of *tert*-butyl acrylate chain initiating radical initiated by 2-benzoyl-2-propanol as initiator, along with isopropyl radical generated from the initiator, are shown. It is noted that all of the emission type (E) spectra are observed, including the initiator-derived radical (Fig. 6e). It is further observed that R, as indicated in the structural formula, corresponds to the benzoyl or isopropanol radical depicted in Fig. 6e.

[7] Muus, L. T., Atkins, P. W., McLauchlan, K. A., Pedersen, J. B. Eds., *Chemically Induced Magnetic Polarization*, D. Reidal Publishing Company, Dordtrecht-Holland/Boston USA (1977).

[8] Kevan, L., Schwartz, R. N., eds., *Time Domain Electron Spin Resonance*, Wiley Interscience Publications, John Wiley & Sons (1979).

[9] Flory, P. J., *Principles of Polymer Chemistry*, Cornell Univ. Press (1953).

[10] Kajiwara, A., *JEOL News* (Japanese ver.), **40**, 34-45. Kajiwara A (2008), *JEOL News*, **43**, 39-49 (2008).

[11] Kamachi, M., Kajiwara, A., Saegusa, K., Morishima, Y., *Macromolecules*, **26**, 7369-7371 (1993).

[12] Kajiwara, A., Konishi, Y., Morishima, Y., Schnabel, W., Kuwata, K., Kamachi, M., *Macromolecules*, **26**, 1656-1658 (1993).

[13] Kajiwara, A., *Macromol. Rapid. Commn*., **30** 1975-1980 (2009).

[14] Kajiwara A., *Pure & Appl. Chem*. **90**, 1237-1254 (2018).

[15] Kajiwara, A., *Polymer*, **72**, 253-263 (2015).

[16] Mizuta, Y., Morishita, N., Kuwata, K., *Chem. Lett*., **28**, 311-312 (1999).

[17] Mizuta, Y., Morishita, N., Kuwata, K., *Appl Mag. Res*., **19**, 93-110 (2000).

[18] Takemura, T., Ohara, K., Murai, H., Kuwata, K., *Chem. Lett*., 1635-1638 (1990).

[19] Fouassier, J. P., Rabek, J. F. eds, *Radiation Curing in Polymer Science and Technology, Vol. II, Photoinitiating Systems*, Elsevier Science Publishers LTD., England, UK, Chapter 2, pp.63-154 (1993).

JEM-120i, a 120 kV Transmission Electron Microscope with Compact Appearance and Ease of Use –Its Features and Applications–

Haruka Aoki EM Business Unit, JEOL Ltd.

We developed the JEM-120i based on the main concepts of "Compact", "Easy to Use" and "Expandable". A totally new external appearance and compact size of this innovative transmission electron microscope (TEM) fits any installation location and can support users from beginner to expert with easy-to-use operations. This article presents the features and some application examples (for biological tissues and polymer materials) of the JEM-120i.

Introduction

The TEM, which illuminates a thin specimen with an electron beam, forms an image using transmitted and scattered electrons passing through the specimen. The TEM image shows any structure difference in the specimen with high resolution. Transmission of the electron beam through the specimen requires high accelerating voltage. For thick specimens, 1,000 kV is needed for image observation. To generate a highly accelerated electron beam, a high voltage tank is required. In addition, to deflect the electron beam using electro-magnetic lenses, a strong magnetic field is needed. Therefore, TEMs are typically large, thus necessitating preparation of a dedicated room for installation of the microscope.

However, increasing attention on nanostructures such as high functionality materials, gives rise to the importance of easy-to-use instrumentation.

With this in mind, in order to offer a user-friendly microscope, the JEM-120i was developed. Based on several innovative concepts, the JEM-120i streamlines the usage of TEM from installation and normal use to maintenance. This compact TEM is highly expandable and is adaptable to a variety of applications; designed to be used by a broad range of users.

1. Features of the JEM-120i

1.1 Compact design

The JEM-120i was developed as a successor model to the highly reputed JEM-1400 series, which was mainly used for biological studies. Compared to the JEM-1400Flash, a dramatic decrease in the size of the JEM-120i results in about a 30% reduction of height, about a 60% reduction of width, and about a 20% reduction of depth (**Fig. 1**). This innovative compact design gives flexibility to the choice of the installation room, since the room requires only 1.8 m^2. With the greatly reduced height of the microscope main unit, the specimen holder insertion position is also lower, enabling a user to replace the specimen holder while sitting in the chair near the instrument. An LED light, which is located surrounding the holder insertion port, changes its color depending on the state of the TEM instrument. This capability allows the user to intuitively insert and retract the holder (**Fig. 2**). In addition, easy filament replacement

Fig. 1 External appearance of the JEM-120i and a comparison with a conventional TEM model.

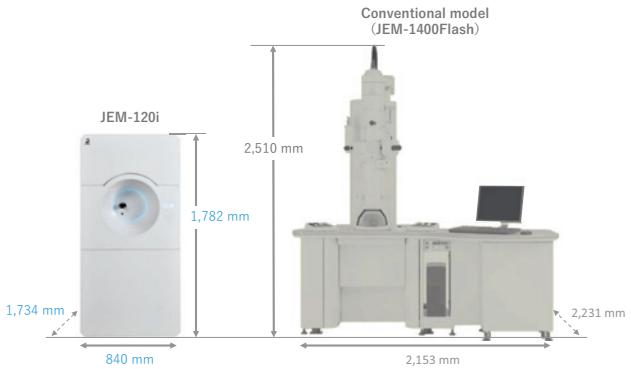

Fig. 2 LED light displaying the state of the microscope, located surrounding the sample exchange port (specimen holder insertion port).

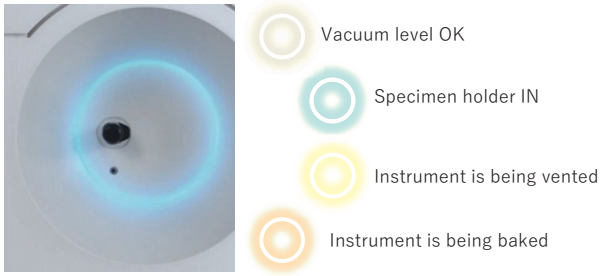

The LED light turns from blinking to lit during the process of holder exchange depending on the vacuum level; therefore, the user can easily determine when the microscope is ready for holder insertion.

〉〉 3-1-2, Musashino, Akishima, Tokyo,196-8558, Japan | E-mail: haoki@jeol.co.jp

is possible. This is due to both a lower filament replacement position and to a newly developed cartridge-type filament unit, allowing any user to exchange the filament (**Fig. 3**).

1.2 Simple operation

With simply a mouse click, the new TEM control software for the JEM-120i provides automatic operations needed for image observation. **Figure 4** shows the operation graphical user interface (GUI) of the JEM-120i. Clicking the Start button (Step 1) automatically performs a vacuum check and turns on the lenses. Then the voltage increases to the preset accelerating voltage. When the voltage has reached this value, the beam emission is turned on and the default electron optics conditions are set. Next, the standard camera "NeoView" for the JEM-120i automatically captures a wide area image. With the JEM-120i, conventional manual operations done by the user are eliminated. Instead, simply clicking the Start button initiates automatic operations necessary for observation preparation.

This acquired wide area image is displayed on "Nanospace Map Mini" on the monitor screen (Step 2 in Fig. 4). Double-clicking on the target position on the wide area image performs automatic stage movement to the target field-of-view. This capability allows the user to observe the target field-of-view while viewing the stored image of the entire grid, and also easily observe a different area of interest on the wide area image without needing to lower the magnification.

When the field-of-view for observation is determined, the instrument is ready to capture an image (Step 3 in Fig. 4). The JEM-120i comes with Butler mode incorporated in FEMTUS™ that controls the detectors for the TEM. Butler mode assists in acquisition, so even an inexperienced operator can capture an image easily. By simply clicking three buttons in "Auto Adjustment" (Step 3) in Butler mode, beam alignment, stage Z (height) adjustment, and focusing are automatically executed. After that, clicking the Capture button completes the acquisition and saves the image.

When image capture is completed, clicking the Sample Exchange button (Step 4) closes the beam valve and the stage moves automatically to the sample exchange position. After this final step, the holder can be smoothly exchanged.

1.3 Expandability

With various optional attachments, the JEM-120i can expand its applications for a wide range of samples (**Fig. 5**). The microscope can configure not only the standard camera "NeoView", but also a JEOL manufactured high resolution camera "SightSKY™" with 19 mega pixels. The SightSKY™ has a high-sensitivity, low-noise CMOS sensor as well as a high frame rate of up to 58 fps. This enables both easy capture of high-definition images with detailed structures and smooth searching for the field-of-view.

Electron Tomography on the JEM-120i is provided by TEMography, manufactured by System In Frontier (SIF). This software provides easy-to-use components for TEM tomography, including acquisition of tilt series of TEM images, 3D reconstruction from the acquired images, and visualization of the reconstructed image. Thus, the internal structure of the specimen can clearly be determined in 3D.

Furthermore, the addition of Shot Meister, manufactured by SIF for the JEM-120i uses "Limitless Panorama" (LLP) for ultra-wide field-of-view montaging. LLP combines beam shift and stage scan functions, enabling automatic image capture over a very wide area on the order of a millimeter. With LLP, a high-definition image from any desired area can automatically be captured and automatically aligned. LLP covers low-magnification, overall-view imaging to high-magnification, fine-structure imaging of the target area.

LLP exploits this capability effectively when used with the SiN Window Chip. The Chip is a specimen supporting plate that uses a high-strength silicon nitride (SiN) film. The Chip has no grid bars and enables wide field-of-view observation over 1 mm × 2 mm,

Fig. 3 Filament replacement port.

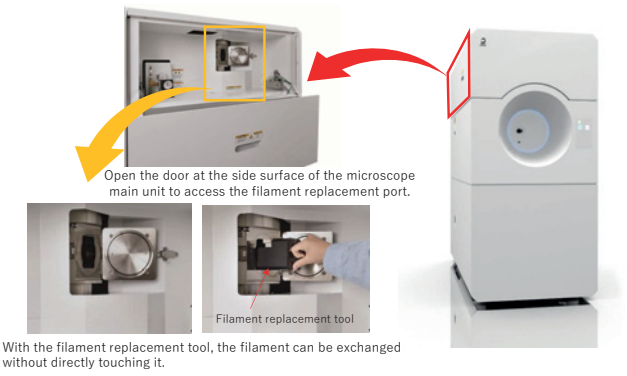

Fig. 4 Operation GUI and observation flow.

the same area as with a single hole grid [1]. With no grid bars, the SiN Chip can be used with LLP to provide wide-area montaging. SiN, used as a specimen supporting film, provides higher strength than the formvar film typically used for a single hole grid. The SiN film is resistant to wear and its surface is flat. As a result, prepared and collected sections have few wrinkles. LLP combined with the SiN Window Chip facilitates observation of a wide area and of serial sections (see Section 2.1).

The JEM-120i is also suited to retrofitting, including STEM (scanning transmission electron microscopy). To meet a customer's needs, STEM can be added after the purchase and installation of the microscope.

2. Application Examples

Figure 6 shows an application example of the JEM-120i using the NeoView camera. The four TEM images demonstrate that fine structures of biological tissues and polymer materials composed mainly of light elements are imaged with high contrast. In addition, the drift correction function incorporated into the JEM-120i suppresses specimen drift to the utmost extent, even when observing very fine structures of proteins. This feature allows for stable image observation.

2.1 Serial Section TEM (ssTEM) for 3D structural analysis

We present examples of the three-dimensional (3D) structure of plant cells by Serial Section TEM (ssTEM) using a SiN Window Chip.

・ssTEM

ssTEM is a 3D structure reconstruction method that prepares serial sections (thickness: several tens of nm each) using a ultramicrotome, captures serial cross section TEM images of the target position in each section and then reconstructs the 3D structure. TEM provides high resolution images [3], however expert techniques are essential for specimen preparation because a single hole grid with no grid bars must be used to prevent cutoff of the field-of-view. To overcome this difficulty, this ssTEM measurement used a SiN Window Chip that has a higher strength than the single hole grid described above (**Fig. 7**).

Fig. 5 Examples of optional attachments.

(a) JEOL's CMOS camera
SightSKY™

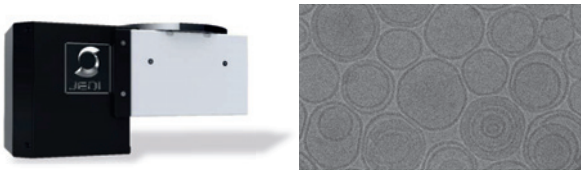

Specimen: Liposome (ice embedding) — 100 nm

(b) 3D structure observation using TEMography

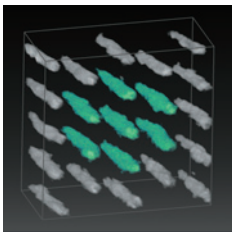

Specimen:
Cylinder structure
(en bloc staining in osmium tetroxide)
Tilt angle:
−70° to +70° (1° step)
Specimen image:
Courtesy of Professor Hiroshi Jinnai,
Institute of Multidisciplinary Research for
Advanced Materials (IMRAM),Tohoku University

(c) Ultra-wide field of view montage system
Limitless Panorama

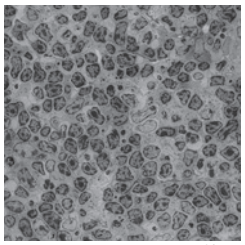

— 10 μm

Specimen: Spleen of mouse
Magnification: ×8,000
Number of images: 25 × 25

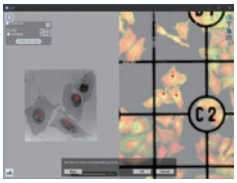

Specimen: Hela cell

With a link function with optical microscope images, CLEM is available.

(d) Specimen plate with supporting film for large area observation
SiN Window Chip

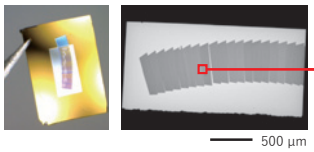

— 500 μm

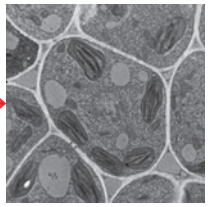

Specimen: Carrot leaf — 2 μm

Fig. 6 Application examples.

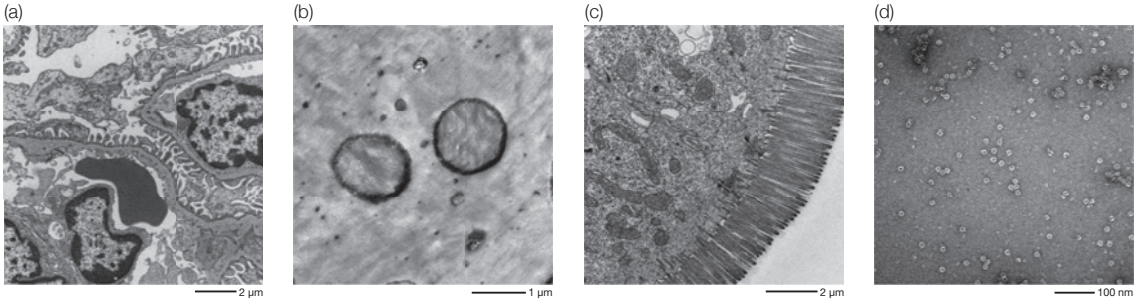

(a) Kidney of rat, (b) Polyethylene/Polypropylene, (c) Small intestine of rat, (d) Ferritin (negative staining)

· Preparation and observation of serial sections

From carrot leaves approximately 250 serial sections (thickness: 70 nm each) were prepared and collected onto a total of five SiN Window Chips. In advance of this preparation process, "chemical fixation" and successive "*en bloc staining*" using uranyl acetate were carried out; therefore staining of the sections was omitted.

Figure 8 shows TEM images of 177 serial sections from one mesophyll cell. The TEM images demonstrate that one cell is clearly observed with almost no wrinkles and contaminants. As a result, the organelle structure and its internal membrane structure are elucidated with high contrast.

Fig. 7 Appearance and structure of the SiN Window Chip.

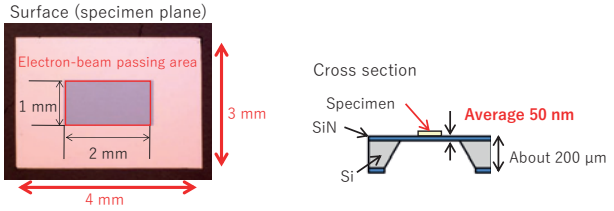

The area where the electron beam passes through is covered by SiN (with no bar); therefore, a wide area can be observed without field-of-view cutoff as is the case with a single hole grid.

· Segmentation and 3D structure reconstruction

From serial section images of one cell, segmentation was performed for chloroplasts and cell walls. This segmentation used U-Net, which is a convoluted neural network [2]. The use of U-Net enabled automatic acquisition of 177-image segmentation results from little training data, and the segmentation process was efficiently completed.

Based on those segmentation results, 3D reconstruction was executed for a cell body and chloroplasts. **Figure 9** shows a reconstructed 3D image. This reconstruction demonstrates the visualization of the morphology of a cell and chloroplasts and the distribution of chloroplasts within the cell. Furthermore, it was found that the existence ratio of chloroplasts in the cell was about 22%.

Summary

The JEM-120i, based on the main concepts of "Compact", "Easy to Use" and "Expandable" was developed, with the microscope fitting any installation location and enabling any user to use via simple operation. The JEM-120i provides high contrast observation of nanostructures in biological tissues and polymer materials. In addition, this innovative TEM is equipped with a variety of optional attachments for wide-area observation and 3D structure analysis. Not only experts, but also beginners can smoothly operate the JEM-120i and it will be used by a wide range of researchers and engineers.

Fig. 8 Serial sections obtained from one cell and a partially enlarged image.

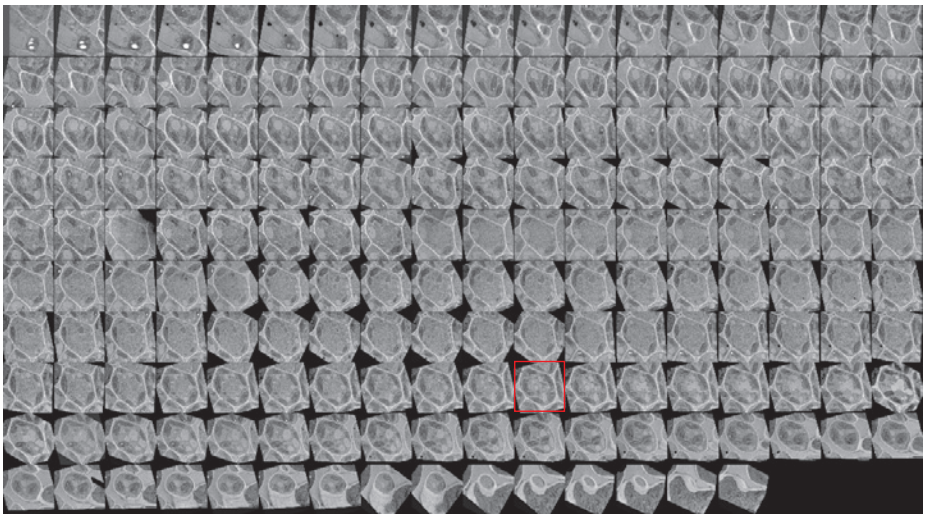

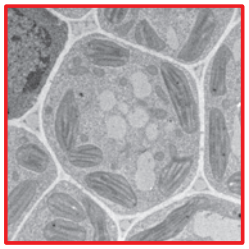

[Conditions]
Accelerating voltage: 120 kV
Total images: 177
(SiN Window Chip: 5)

[Image processing]
Positional alignment: Fiji
(Linear stack Alignment with SIFT)

Fig. 9 3D reconstruction image of a cell body (blue) and chloroplasts (green).

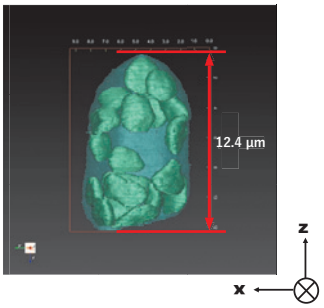

References

[1] Konyuba et al., *Mycroscopy* **67**, 367-370 (2018) .
[2] K. Konishi et al., *Microscopy*, **70**, 526-535 (2021) .
[3] C. J. Peddie et al., *Nature Reviews Methods Primers*, 2:51, 1-23 (2022).

Progressing From Easy to Automatic – Overcoming Challenges of Automation with the Latest FE-SEM JSM-IT810 –

Hironobu Niimi, Tatsuro Nagoshi, Noriyuki Inoue EP Business Unit, JEOL Ltd.

We have developed "Neo Action," a function that automates SEM image observation, EDS analysis, and report generation by enhancing the precision of basic adjustment functions of focus/alignment adjustment, astigmatism correction. In addition, an automatic maintenance function has been developed to periodically check and readjust the alignment conditions, astigmatism correction, magnification accuracy, and EDS energy calibration to ensure stable operation of the instrument.

This paper presents specific application examples using these functions.

Introduction

In recent years, there has been a growing demand for automated measurement technology to simplify the operation of measuring instruments and make better use of machine time; SEM is no exception. SEM is essential for detailed observation and analysis of fine structures that cannot be seen with an optical microscope. However, to obtain a clear image, advanced adjustments such as focusing/alignment and astigmatism correction are necessary. Automating these tasks is essential to simplify SEM operation and achieve efficient observation and analysis.

Recent advances in image analysis technology have greatly improved the automation of SEM adjustment tasks. JEOL's FE-SEM is equipped with advanced electron lens control technology, the next-generation electron optical system New Electron Optical Engine or "Neo Engine". The Neo Engine performs optimal adjustments for each electron lens in real time. In addition, the "Zeromag" feature seamlessly links optical and SEM images, making it easy to determine the desired sample position. The integration of SEM and EDS allows EDS analysis to be performed with just three clicks from SEM image observation [1].

With the previous JSM-IT800, the integration of Neo Engine, Zeromag, and EDS integration made it simple to observe and analyze samples quickly. The latest model, the JSM-IT810, inherits this easy operability cultivated up to now while evolving the automatic functions to realize fully automated observation and analysis.

1. Automatic Observation and Analysis Function "Neo Action"

Neo Action is a feature that continuously acquires SEM images and EDS analyses of specified fields of view and automatically generates reports of the acquired data. This feature enables routine SEM measurements and overnight operation for long-term measurements. As with the EDS integration, Neo Action comes standard with the SEM control software (commonly known as SEM Center) and provides an easy-to-use graphical user interface (GUI). As shown in **Fig. 1**, all the information required for automatic measurement is contained in a single software package, greatly improving ease of use.

In Neo Action, you can create a workflow for continuous measurements by arranging action icons associated with measurement content. Each action icon is associated with a measurement position and measurement conditions. The measurement position is displayed on the optical or SEM image of the Zeromag in the Measurement Position area, and the details of the SEM observation and EDS analysis conditions can be set in the Condition area. In addition, the "Report Area" displays the report generated based on the configured workflow (see Fig. 1).

Once the continuous measurement is started, the measurement data is automatically included in the report as the data acquisition progresses, and the report is automatically generated when the measurement is completed. In this way, automatic measurement from data acquisition to report generation can be performed without complicated operations.

1.1 Multi-field observation and analysis examples for defect analysis of electronic components

The following is an application example of Neo Action for SEM image acquisition and EDS map analysis of repetitive structures as failure analysis of electronic components. The sample was an IC chip pre-processed by the CROSS SECTION POLISHER™. Backscattered electron images of 10 bonding areas indicated by red frames in **Fig. 2** were acquired, and EDS map analyses were also performed in these areas.

To set up Neo Action, select the field of view to be measured (a), set the observation conditions such as detector and scan speed (b) and the equipment conditions such as field of view magnification and stage position (c), and choose the EDS map analysis conditions (d), as shown in **Fig. 3**. **Figure 4** shows a screen set up to acquire SEM images and EDS maps of 10 bonding sections using autofocus and automatic astigmatism correction. In parallel with the automatic measurement, a report

〉〉 3-1-2, Musashino, Akishima, Tokyo,196-8558, Japan | E-mail: hniimi@jeol.co.jp

Fig. 1 GUI screen of Neo Action, an automatic observation and analysis function.

Fig. 2 SEM image and optical image of IC chip cross section, which was processed by the CROSS SECTION POLISHER™.

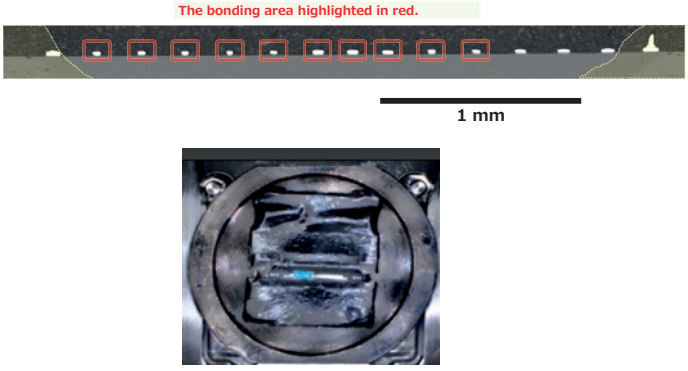

The yellow area in the SEM image of the IC chip cross-section shows the area where the ion beam processing has not been completed, and the red frames show the bonding areas of interest. The SEM image of the cross section of an IC chip is the result of an automatic montage of eight images.

Fig. 3 GUI screen for setting measurement conditions assigned to the function flow.

(a) Measurement Field Settings and Action Icons

(b) Observation Condition Settings

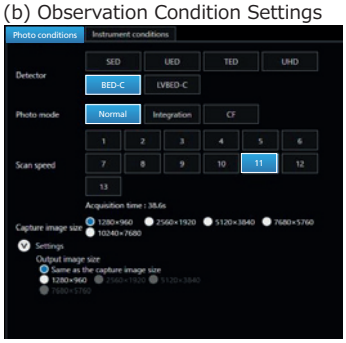

(c) Instrument Condition Settings

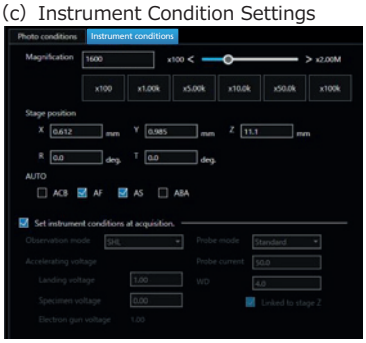

(d) Analysis Condition Settings

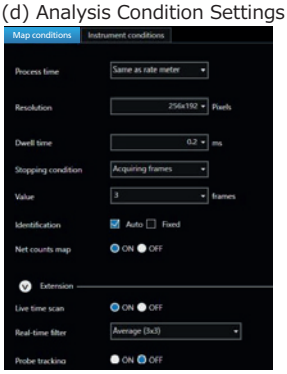

(a) Measurement field of view setting and action icons, (b) Observation condition setting items, (c) Instrument condition setting items, (d) Analysis condition setting items.

is automatically generated (see **Fig. 5**). From the backscattered electron image and EDS map in this report, it is possible to determine the location of defects in each bonding area.

The automatically generated report can be checked and analyzed with the data management software SMILE VIEW™ Lab (see **Fig. 6**) and can also be reworked into a different style report if desired.

The ability to continuously observe and analyze multiple fields of view automates time-consuming tasks that could previously only be performed manually, making it possible to use time more effectively.

1.2 Example of using Neo Action for an analysis that requires conditional search

1.2.1 Example of searching for accelerating voltage to obtain charging-reduced conditions

Charging is a problem in SEM observation of non-conductive samples. The appearance of charging varies depending on the accelerating voltage setting for each sample, and the optimum accelerating voltage value is sometimes unknown. Therefore, Neo Action can be set to acquire SEM images at several accelerating voltage values, and the optimum accelerating voltage value can be extracted after the measurement is completed. In this article, we introduce an example using Neo Action to search for the condition that reduces charging the most by changing the accelerating voltage to 0.6, 0.8, 1.0, 1.2, and 1.4 (kV). The sample is cerium oxide powder, which is used as an abrasive and catalyst. As shown in **Fig. 7**, the accelerating voltage of 1.2 kV was found to remove the most charging.

1.2.2 Example of searching for the ideal working distance (WD) to obtain composition contrast or to reduce topographic artifacts

It is known that the composition contrast and the artifacts from topography change with WD for the upper electron detector (UED) and the upper hybrid detector (UHD) of the JSM-IT810 (SHL) [2]. Therefore, we set Neo Action to acquire UED and UHD SEM images at several WDs and extracted the optimal WD after the measurement was completed.

The sample is carbon nanotubes with iron particles dispersed on them. Images were acquired using Neo Action with WDs of 2, 4, 6, and 8 (mm). The results are shown in **Fig. 8**, and the appearance of the SEM image changes depending on the WD. As shown in **Fig. 9**, the image with WD 2 mm has a better signal-to-noise ratio of composition contrast of iron particles than the image with WD 6 mm for UED. On the other hand, in the case of UHD, WD 6 mm has a deeper depth of focus and produces an image with a more balanced signal throughout.

Fig. 4 GUI screen after setting the measurement position and conditions in Neo Action.

The measurement position is the orange frame part in Fig. 4, and the conditions are accelerating voltage 7 kV and WD 7 mm.

Fig. 5 GUI screen during report display in Neo Action.

Fig. 6 Data management software SMILE VIEW™ Lab.

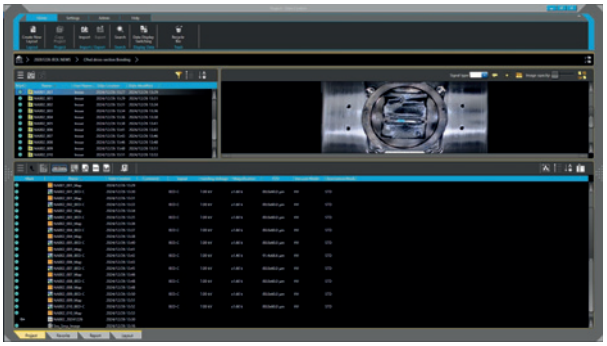

Completed measurement results can be immediately checked and analyzed in SMILE VIEW™ Lab, and the results can also be reworked into a different style report if desired.

Fig. 7 Result of searching accelerating voltage to obtain charge relaxation conditions.

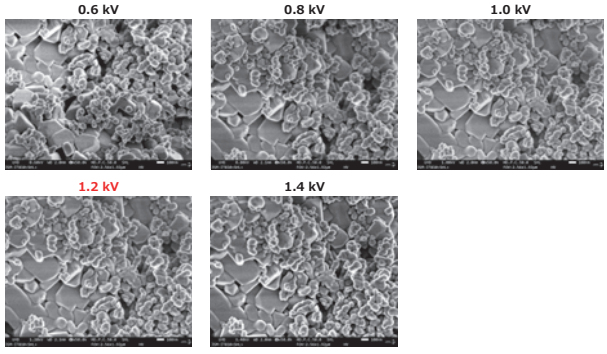

The sample is cerium oxide powder.

2. Automatic Maintenance

Since SEM is also used as an inspection system in the quality assurance department, it is sometimes required to check the length measurement accuracy and EDS energy position accuracy at certain intervals in the year, not to mention the stable operation of the system.

As shown in **Fig. 10**, the automatic maintenance function consists of three automatic maintenance functions: beam alignment (optical axis and astigmatism adjustment), confirmation and adjustment of magnification accuracy, and EDS energy calibration, as well as a dedicated sample holder used to perform these functions. The dedicated sample holder consists of a tin ball sample for beam alignment, a mesh sample for magnification accuracy, and a Cu/Al sample for EDS energy calibration. The flow of use is shown in **Fig. 11**, and it is assumed that the equipment manager sets up the dedicated sample holder in advance after work, and that it is run automatically overnight.

Next, the details of each of the three maintenance functions are described.

2.1 Beam alignment and astigmatism adjustment

This function adjusts the axis and astigmatism according to the desired observation conditions. As shown in **Fig. 12**, frequently used observation conditions can be preset. By pre-adjusting the observation conditions used in Neo Action, stable automatic measurements can be achieved.

2.2 Magnification confirmation and adjustment

This function checks the length measurement accuracy for the desired observation conditions and adjusts if necessary. The length measurement accuracy is calculated as the magnification

Fig. 8 Result of WD search to obtain the most compositional contrast and topographic information.

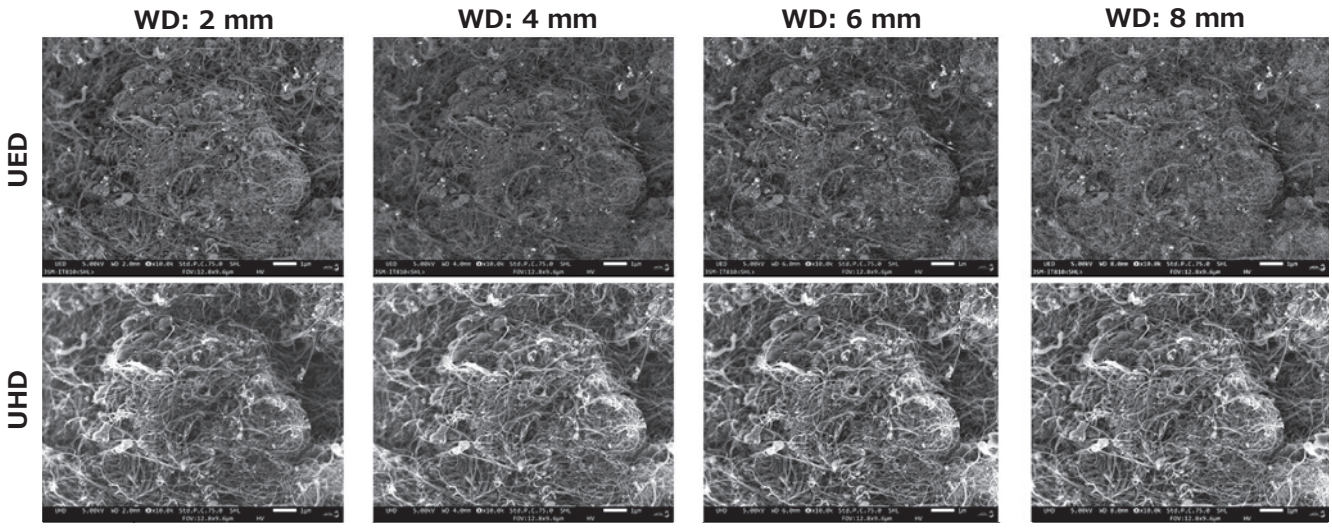

The sample is Fe/CNT.

Fig. 9 Optimal WD and detector for composition contrast and for reducing topographic artifacts.

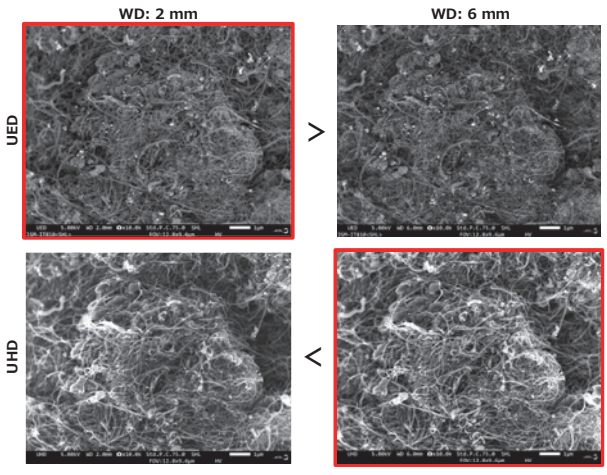

Fig. 10 Automatic maintenance function items and dedicated sample holder.

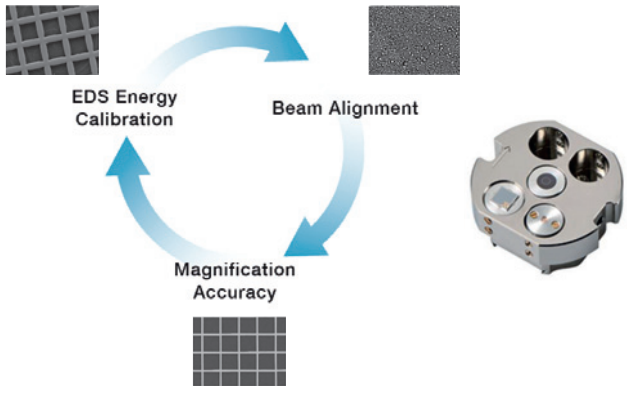

Fig. 11 Flow of using the automatic maintenance function.

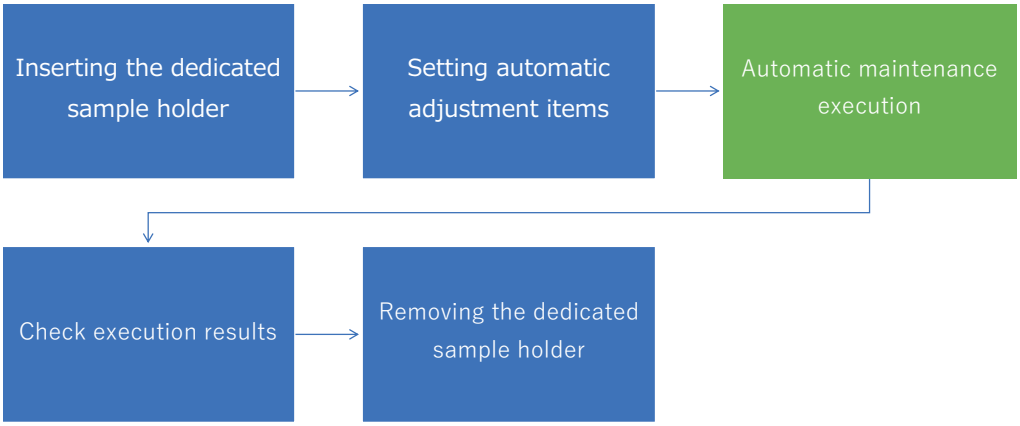

Blue parts are manual, and green parts are automatic.

Fig. 12 Dialog box for registering the observation conditions to be adjusted in the automatic maintenance function.

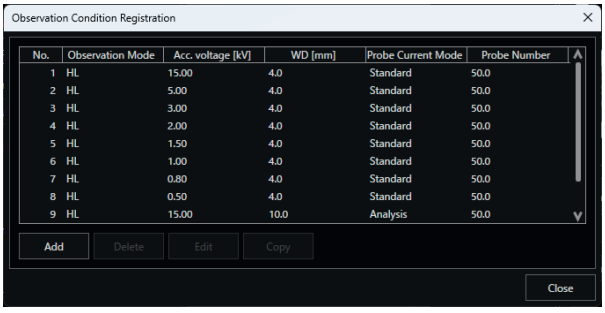

Fig. 13 Dialog for displaying the results of the automatic maintenance function.

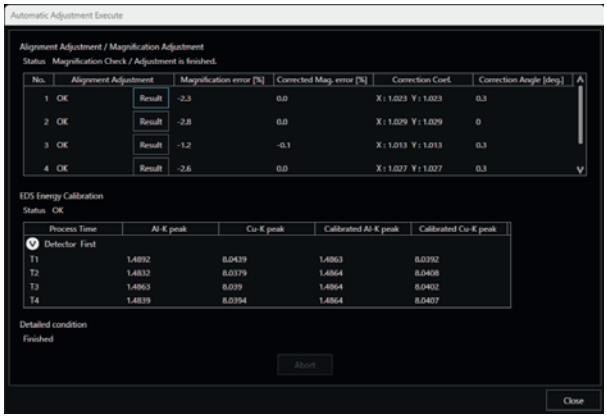

error [%] from the SEM image of a reference size mesh.

This function allows the user to select either "Magnification check," which only confirms the magnification error, or "Magnification adjustment," which adjusts the magnification so that the error becomes 0%. As shown in **Fig. 13**, the column labeled "Magnification error [%]" shows the result before adjustment, and "Corrected Mag. error [%]" shows the result after adjustment, indicating that the magnification error of 1 to 3% was reduced to almost 0% by magnification adjustment. As shown above, length measurement can be performed with higher accuracy than ever before.

2.3 EDS energy calibration

The EDS energy position, which is directly related to the accuracy of elemental identification, is calibrated by the energy position of the K-line of Al and the K-line of Cu.

Conclusion

JEOL's latest FE-SEM, JSM-IT810, is equipped with an automatic observation and analysis function, Neo Action, and an automatic maintenance function. This functionality enables automation of routine tasks and long measurements and reduces the amount of manpower and machine time required to operate the SEM. The automatic maintenance function automatically performs axis/astigmatism adjustment, confirmation and adjustment of magnification accuracy, and EDS energy calibration under frequently used conditions and is shown to improve the stable operation and reliability of the system.

AI technology is expected to further develop SEM automation technologies, such as autonomous control of SEM measurement, automatic analysis of SEM images, and EDS analysis. By further simplifying the use of SEM, SEM users are expected to be able to use SEMs in a broad range of fields of R&D and quality control. JEOL will continue to actively incorporate technological advances to further improve SEM automation technology.

References

[1] O. Suzuki et. al., "Various Analyses of Fine Structures using Multipurpose High Throughput Analytical FE-SEM: JSM-IT800", *JEOL NEWS*, Vol.**55**, No.1, P49-P55, (2020).

[2] T. Nagoshi et. al., "New Detection System of High-end FE SEM JSM-IT800 Super Hybrid Lens <SHL>", *JEOL NEWS*, Vol.**53**, No.1, pp30-36, (2021).

Development of a Large Solid-Angle Windowless EDS Detector "Gather-X" Used with a Field Emission Scanning Electron Microscope (FE-SEM)

Kota Yanagihara EX Business Unit, JEOL Ltd.

The Gather-X (JED series DrySD™ Gather-X), a windowless-type EDS, is a flagship model of JEOL EDS series. This innovative Gather-X allows for detection of characteristic X-rays from lithium, which was difficult to detect with the currently used standard EDS detectors. In addition, with the Gather-X, high-throughput and high spatial resolution EDS mapping are achieved by making the X-ray sensor closer to the specimen. This article presents the development status, features and application examples of the Gather-X.

Introduction

Energy Dispersive X-ray Spectroscopy (EDS or EDX), which is incorporated in various analysis instruments (TEM, SEM, EPMA, Auger, XRF, etc.), is an analytical method which detects characteristic X-rays generated from a specimen by irradiation of an electron beam or X-rays onto the specimen and acquires characteristic X-ray spectra. Energies and intensities of the spectra are analyzed to perform qualitative and quantitative analyses of observation areas of the specimen. **Figure 1** shows three types of JEOL EDS (JED series).

Wavelength Dispersive X-ray Spectroscopy (WDS or WDX) is another analytical method using characteristic X-rays, which is installed in the Electron Probe Microanalyzer (EPMA). WDS provides high energy-resolution and high peak-to-background ratio (P/B ratio); therefore, the lower detection limit and quantification accuracy are superior to EDS. Thus, EPMA makes it possible to perform high-accuracy quantitative analysis of trace elements in the specimen. On the other hand, EDS provides a higher detection efficiency than WDS owing to its hardware configuration and, also with EDS, multiple elements can be analyzed simultaneously. Thus, EDS is installed in a variety of models of electron microscopes, and is used as a useful tool that quickly and easily acquires qualitative and quantitative analysis results of element-distributed sites using elemental mapping and line analysis of a local area of the specimen.

EDS Analyzer for Use with SEM-EDS ~Standard EDS Detector~

The SEM specimen chamber is not always kept at high vacuum because when observing and analyzing insulating materials, the chamber is under a low-vacuum (LV)

Fig. 1 EDS detectors: JED series.

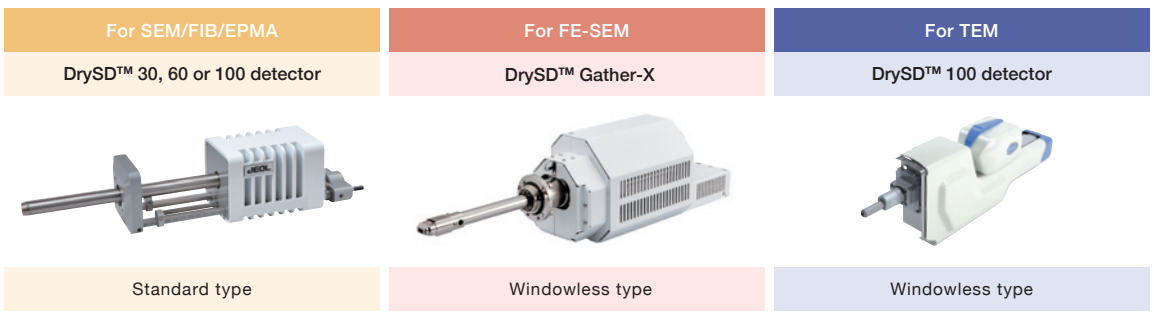

〉〉 3-1-2, Musashino, Akishima, Tokyo, 196-8558, Japan | E-mail: kyanagih@jeol.co.jp

environment and when exchanging a specimen, an airlock is used and the chamber is vented (draw-out system). An EDS detector attached to the chamber is subjected to various environments.

A Peltier element, generally used as the X-ray sensor (semiconductor detector) for the EDS detector, is cooled down to –30 °C to –40 °C for reducing noise. This cooling temperature must be kept under the above-described several environments because the reproducibility of analysis results should be maintained without noise fluctuations. Another issue is that if a trace volume of water, oil and/or hydrogen exists in the chamber and the X-ray sensor is exposed to them, the absorption of those materials to the sensor can break the sensor. To avoid such problems, the currently used EDS detectors have a protection system that vacuum-seals the X-ray sensor. This capability isolates in-vacuum specimens from the outside environments of the chamber. To detect characteristic X-rays in the vacuum-sealed condition, an X-ray transmission window is also attached in front of the sensor.

However, characteristic X-rays with energies below 1 keV are partially absorbed through the window. These X-rays below 1 keV correspond to the K lines of the first period of light elements (Li to F), the L lines of the second period elements (Na to Cl) and of the first transition metals (Sc to Cu), and the M lines of the second transition metals (Y to Ag). The absorption ratio of characteristic X-rats to the window is different depending on the window type (composition and thickness) and the energy of characteristic X-rays.

EDS Analyzer for Use with SEM-EDS ~Windowless EDS Detector~

Figure 2 shows an example of SEM-EDS analysis of a beryllium copper (BeCu) where a few % of Be is doped into Cu for increasing the hardness of a Cu material. Since Be is localized in this material, EDS mapping with high magnification and high spatial resolution is required. To achieve this, it is required to suppress diffusion of an incident electron beam in the depth direction and lateral direction within a specimen, by setting a low accelerating voltage. However, the Be-K line has low energy and is absorbed through the window; thus decreasing the detection efficiency. But when attempting to increase the probe current for obtaining the Be-K line with a sufficiently high count rate, the probe size becomes large and this disturbs improvement of the spatial resolution.

The windowless EDS detector is a solution to suppress absorption of low-energy X-rays through a window. In addition, by positioning the X-ray sensor closer to the specimen for increasing the detection sold angle, the collection efficiency of characteristic X-rays is greatly improved. As shown in Fig. 2, high spatial resolution EDS mapping can be obtained even at low accelerating voltage and low probe current.

With a windowless EDS detector, it becomes possible to collect Li-K (54 eV) which was difficult to detect with the standard EDS detectors. This benefit will serve to respond for analytical needs of Li compounds whose applications cover a wide variety of fields, including battery materials, aerospace materials, semiconductor materials, glasses and catalysts.

Features and Technologies of Windowless EDS "Gather-X"

The Gather-X, a windowless EDS detector, improves not only the detection efficiency of low-energy characteristic X-rays (below 1 keV) but also the collection efficiency greatly for all energy regions (below 30 keV) owing to large solid angles achieved by a unique detector geometry. With these benefits, the Gather-X is a flag ship model of JEOL EDSs, which is specially used for a JEOL JSM-IT810 Field Emission (FE) SEM (higher-version model of JSM-IT800). The Gather-X has three main features, to be described in detail.

Fig. 2 High spatial resolution EDS mapping of beryllium copper (BeCu) acquired using Gather-X.

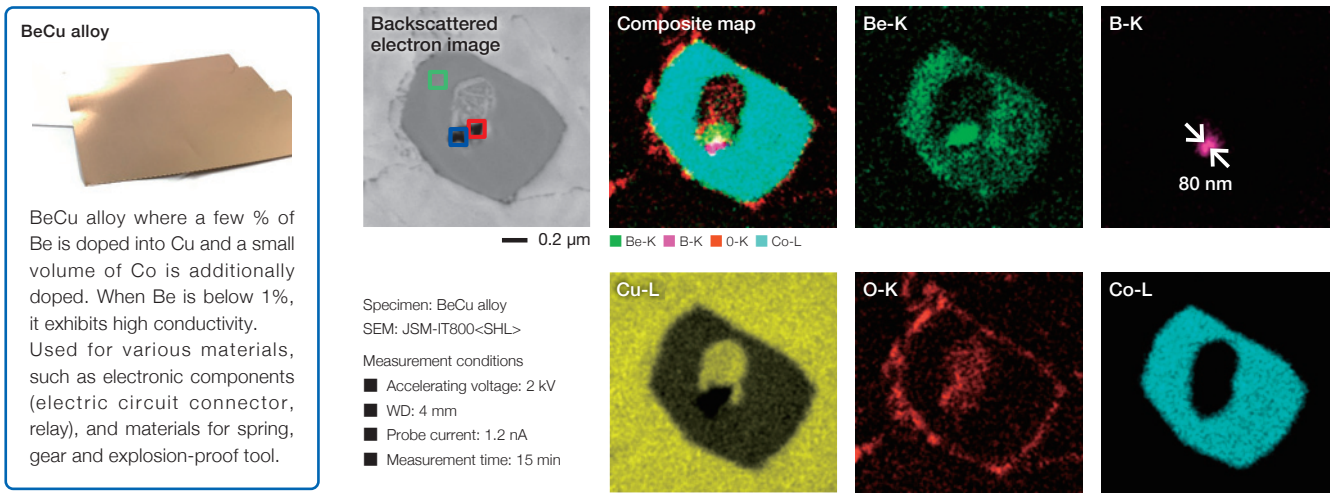

- Use of low accelerating voltage (2 kV) with Gather-X reduces the characteristic X-ray generation region, efficiently collecting low-energy characteristic X-rays.
- High spatial resolution elemental maps are obtained from light elements of Be, B and O contained in a BeCu alloy.
- High spatial resolution EDS mapping is effective to visualize distribution of small-sized elements.

1. High sensitivity analysis for all energy regions
2. High spatial resolution EDS mapping
3. High usability and safety operation

1. High sensitivity analysis for all energy regions

X-ray absorption through a window

JEOL standard EDS detectors have thin polymer windows (thickness: a few 100 nm), and the windows absorb low-energy characteristic X-ray signals, especially at energies below 1 keV (**Fig. 3**). Among these characteristic X-rays, the X-rays with energies lower than 100 eV have almost 0% transmittance, mainly due to the thickness of the polymer window. These X-rays include Mg-L (49 eV), Li-K (54 eV), Al-L (70 eV) and Si-L (90 eV). This causes significant difficulty in detecting such X-rays. For characteristic X-rays with energies higher than 100 eV, for example, the transmittance is as follows: Be-K (110 eV) is 8%, B-K (183 eV) is 26% and N-K (392 eV) is 25%. These results indicate that the absorption ratio (transmittance) is different depending on the characteristic X-ray energies affected indirectly by the absorption edge of the constituent elements of the window. Although, for characteristic X-rays with energies higher than 1 keV, the X-rays are partially absorbed through the window. For example, Al-K (1.486 keV) has 74% transmittance to the window.

The Gather-X does not have a window on the detector, thus making it possible to collect characteristic X-rays with energies below 100 eV, which was difficult to collect with conventional EDS detectors. Such a windowless EDS detector greatly improves the collection efficiency of characteristic X-rays with energies higher than 100 eV, leading to high throughput analysis. This improved collection efficiency contributes to sufficient X-ray signals to be acquired even at low probe currents, enabling analysis for a specimen susceptible to electron beam damage.

Windowless EDS technologies

The Gather-X is a windowless EDS detector, but the operator does not have to worry about damage of the detector. The Gather-X provides safety operation owing to the following three reasons.

- The JSM-IT810, a flagship model of JEOL FE-SEMs, is equipped with a high vacuum specimen chamber.
- The JSM-IT810 uses a dry nitrogen gas as the circulating gas in low vacuum (LV) mode. Thus, the volume of impurity gases introduced into the specimen chamber is extremely small, maintaining a high vacuum of the specimen chamber (mentioned above).
- The Gather-X has a safety system linked with the JSM-IT810, thus enabling cooling of the X-ray sensor only at high vacuum operated with the JSM-IT810. There is no possibility of exposure of the cooled X-ray sensor to air when venting the chamber.

Large solid angle

The sold angle (Ω), which is an indicator for detection efficiency, is approximated by the following equation 1, using the X-ray sensor size S and the distance between the X-ray sensor and the specimen L.

$$\Omega = \frac{S}{L^2} \qquad \text{equation 1}$$

That is, the requirements for large solid angle are that the X-ray sensor size is large and the sensor is close to the specimen. The Gather-X has a large X-ray sensor size of 100 mm^2. In addition, unlike a circular shape of the standard X-ray sensor, the Gather-X adopts a racetrack-shaped X-ray sensor; therefore, the Gather-X's X-ray sensor can move closer to the specimen without interference with the objective lens of the JSM-IT810 (**Fig. 4**).

Electron trap system (electron energies below 30 keV)

The X-ray sensor counts not only characteristic X-rays but also the continuous energies of electrons incident on the sensor. These electron energies give rise to the background for EDS spectra and the lower detection limit of the characteristic X-rays is deteriorated. In addition, the incident electrons can cause direct damage to the X-ray sensor for disrupting proper measurement of the X-ray energies by the sensor. Thus, the electron trap is required to prevent the electrons from entering into the X-ray sensor. It is noted that the standard EDS detector is also fitted with an electron trap system, which deflects the path of the incident electron beam using a magnetic field, thus preventing entering of the incident electrons into the X-ray sensor.

The electron trap system of the Gather-X (**Fig. 5**) makes it possible to not only deflect the incident electrons with energies up to 30 keV, but also to allow the system to be moved closer to the specimen by minimizing its size, thus contributing to the improvement of the X-ray collection efficiency. Furthermore, this trap system for the Gather-X was specifically designed

Fig. 3 Graph showing the transmittance of characteristic X-rays from different elements, through the window.

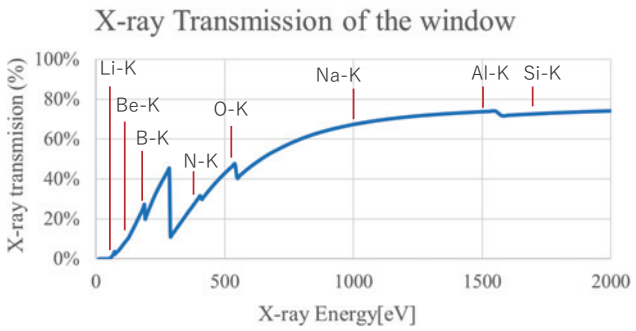

Fig. 4 Large solid angle of Gather-X.

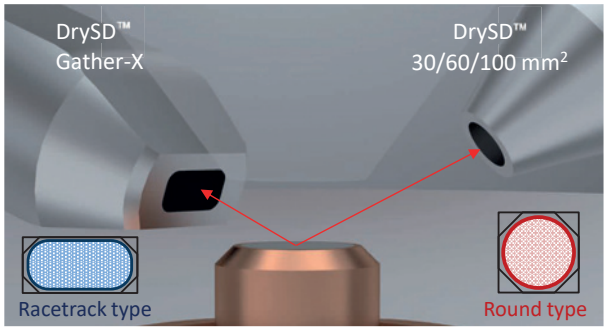

to suppress any magnetic field leaking from the system. This design enables the JSM-IT810 equipped with the Gather-X to maintain high quality of a SEM image by reducing any adverse effect of the primary incident beam onto the specimen during the insertion of the detector, as shown in Fig. 5.

As described above, the three combined technologies of "Windowless EDS", "Large solid angle" and "Electron trap system (below 30 keV)" have improved the X-ray detection sensitivity. Compared to a standard EDS detector (model: EX-74710U1L4Q, X-ray sensor size 60 mm^2) installed in a JEOL JSM-IT810(SHL) FE-SEM, the detection efficiency of the Gather-X has improved. For example; B-K (183 eV): 12.5 times, N-K (392 eV): 13.9 times, Al-K (1.486 keV): 7.5 times and Ti-K (4.509 keV): 7.1 times. The Gather-X provides high sensitivity analysis for all energy regions (**Fig. 6**).

2. High spatial resolution EDS mapping

Adaptable to short working distance (WD) analysis

High spatial resolution EDS mapping requires various analytical conditions, such as short working distance (WD), low accelerating voltage, and low probe currents. However, when performing quantitative analysis with the standard EDS detector, a WD of 10 mm is required. Although, for high resolution SEM imaging, typically a WD of shorter than 10 mm is used. In addition, a large solid angle is not achieved at a WD of 10 mm. These disadvantages can cause issues where the optimum measurement conditions become inevitably different between SEM observation and EDS analysis of the same specimen. The reason for this difference is that, X-ray signals acquired from the specimen must be increased for proper EDS analysis; therefore, typically EDS requires higher probe currents than SEM.

The Gather-X adopts several innovative designs to overcome this problem. The WD during quantitative analysis is achieved to be 7 mm, 3 mm shorter than the standard EDS (at installation of WDS port on JSM-IT810). The collimator for the X-ray detector is innovatively designed to decrease the WD to as short as 1 mm. These capabilities enable analysis at very short WD [1].

Adaptable to BD mode

BD mode (Beam Deceleration), which is standard on the JSM-IT810 FE-SEM, decelerates the incident electron beam before it enters the specimen by applying a bias voltage to the specimen stage. This function especially improves the spatial resolution and signal-to-noise ratio (S/N ratio) at low accelerating voltage. Therefore, with analysis using BD mode, EDS mapping with higher spatial resolution can be achieved. However in this case, if the bias voltage is applied under a condition where the electrically-conductive head of the Gather-X detector comes close to the specimen, discharge may occur.

To avoid this possibility, a safety system (limiting stage movement) has been developed using magnetic-field analysis to obtain the proper conditions which do not cause discharge. As a result, the Gather-X includes a safety system that gives appropriate clearance between the Gather-X and the specimen.

Fig. 5 Electron trap system.

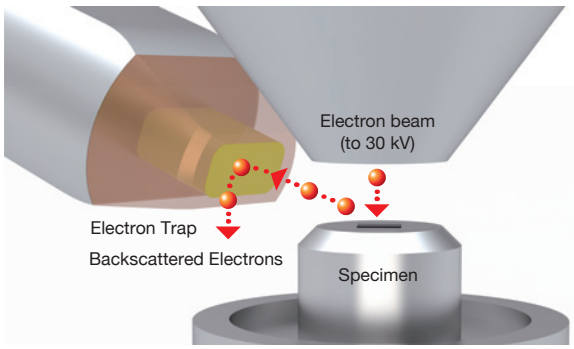

Fig. 6 Comparison of characteristic X-ray detection efficiency between Gather-X and Standard EDS (sensor size: 60 mm^2, 100 mm^2).

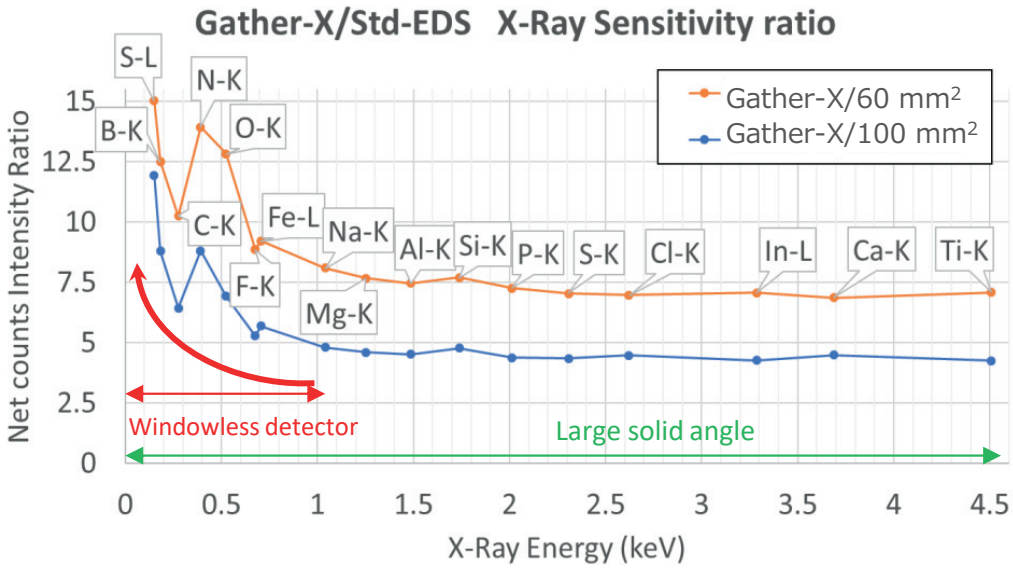

This achievement enables analysis in BD mode (**Fig. 7**).

"Adaptable to short WD analysis" and "Adaptable to BD mode" described in this Chapter, as well as detection-efficiency improvement, and X-ray collection at low accelerating voltage and low probe current explained before, have greatly contributed to the achievement of high spatial resolution elemental mapping using the Gather-X.

3. High usability and safety operation

EDS integration

JEOL EDS systems, including the Gather-X, are fully integrated into the JEOL SEM control software. This integration enables seamless operations and data acquisition from SEM observation to EDS analysis within the same user interface. Reacquisition of a SEM image for EDS analysis is not required, thus achieving quick and smooth SEM-EDS measurement.

JEOL's Live Analysis function makes it possible to display an EDS spectrum or EDS maps in real-time during image observation. This real-time display improves measurement throughput as EDS analysis starts immediately after clicking the target position on the live image on the monitor screen. Then, elemental analysis results can smoothly be obtained.

The SMILE VIEW™ Lab, a JEOL dedicated data management system, links the optical image, SEM images and EDS analysis results. The acquired observation data and analysis data are stored and are linked to each other, allowing for smooth data management. Since the SMILE VIEW™ Lab has a report generation function, a report can be customized and then, a single click of the report can export and output the report to Microsoft® Word® and Microsoft® PowerPoint®. [2].

The operation GUI of the Gather-X is also embedded in the SEM control software. Simply clicking on the screen allows for cooling and moving the X-ray sensor. The motor drive system of the Gather-X makes it possible to quickly insert (or retract) the X-ray sensor to the specified stop positions, with no sound and high accuracy of stop position.

(Note: Microsoft® Word® and Microsoft® PowerPoint® are the product names of Microsoft Corp. in the U.S.)

Interlock systems linked with the SEM main instrument

The Gather-X is equipped with interlock systems designed specifically for use with the JSM-IT810. These include an X-ray sensor protection system to prevent damage to the cooled X-ray sensor during the exposure of the sensor to air, as well as a collision prevention system which avoids the collision of the detector with various specimen holders by leaving a clearance between the detector and the holders. In addition, another collision prevention system for various optional attachments (backscattered electron detector, LV system, STEM, EBSD, specimen exchange rod, etc.) is available.

All of these interlock systems lead to safe operations even by SEM-EDS beginners.

Application Examples

1. Chemical state analysis of soft X-ray regions with SEM / Gather-X / SXES

The JSM-IT810 allows for simultaneous installation of a Gather-X and a soft X-ray emission spectrometer (SXES) which provides chemical state analysis of the soft-X-ray energy region below 1 keV. Since the Gather-X can perform fast elemental analysis including the soft X-ray region, the use of Gather-X as an X-ray screening system for SXES makes it possible to improve the throughput of SXES chemical state analysis and the electron-beam damage to the specimen is significantly suppressed owing to a short acquisition time.

Analysis of solid-state lithium-ion battery

Figure 8 presents an analysis example of a silicon anode of an 84% charged solid-state lithium-ion battery using Gather-X and SXES. A cross-section specimen was prepared from the silicon anode using a JEOL CROSS SECTION POLISHER™ (CP) under an air-isolated environment. From a backscattered electron image of the charged silicon anode, the contrast difference in the anode particles was identified. EDS maps created by the Gather-X revealed the distribution of Li-K (54 eV) and Si-L (90 eV). The peak-top difference between Li-K and Si-L is very small (40 eV); therefore, peak deconvolution was applied to the overlapped peaks using the net map function, and then elemental mapping was performed.

The acquired EDS maps show low intensity of Li-K whereas high intensity of Si-L on the top part of the anode material, indicating that lithium is not sufficiently absorbed in some area of the top part of the anode. Analysis results of SXES for Area 1 (marked with a blue frame) and Area 2 (marked with a red frame) show the difference of the Li-K peak position between lithium in the anode (53.4 eV) and metallic lithium (54.3 eV). The results suggest that the SXES spectra acquired from both Areas 1 and 2 reflect the chemical state of a Li-Si alloy. In addition, the difference in half-width and peak shape of the Si-L emission suggests that the crystal structure of the Li-Si alloy is different between Area 1 and Area 2.

2. High spatial resolution map analysis by short WD and BD mode

The Gather-X enables acquisition of high spatial resolution EDS maps at a low accelerating voltage. This is achieved by a combined use of a shorter WD (7 mm) than the standard WD for qualitative analysis and BD mode, which applies a bias voltage onto the specimen stage.

Analysis of silver nanoparticles (photocatalyst) on titanium oxide

Figure 9 shows EDS maps of silver (Ag) nanoparticles on titanium oxide (size: approximately 18 nm), obtained at a WD of 4 mm and a magnification of ×200,000. High spatial resolution EDS maps are effective for analysis of fine particles, such as catalyst particles.

Fig. 7 Adaptable to short WD and BD mode.

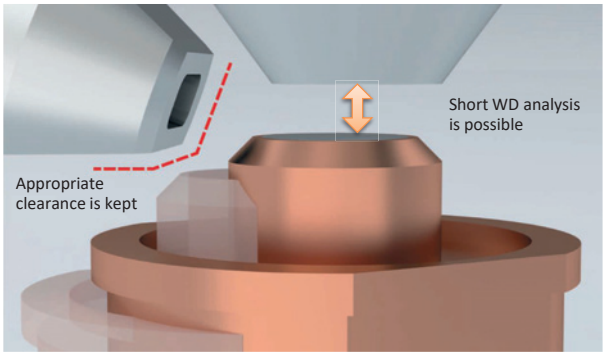

In BD mode, appropriate clearance is kept to suppress discharge.

3. Analysis using multiple detectors

Multiple Gather-X detectors, up to 3 units, can be installed on the JSM-IT810. This configuration achieves faster analysis and is well-suited to specimens which are sensitive to electron beam damage. Analysis using multiple detector units allows for reducing the effects of specimen topography.

Analysis of multi-layers on an IC chip cross section

Using multiple Gather-X detectors is effective for even faster analysis in the semiconductor fields, for the use of quality control and product inspection. Even when multiple Gather-X detectors are configured, the dimensions of each detector (insertion distance, take-off angle and standard WD) are the same and thus, the detection efficiency of the respective detectors is equal. In addition, quantitative analysis can be performed by adding up the X-ray intensities (elemental concentrations) acquired with each detector.

Figure 10 shows an EDS map of each layer on a cross section of an IC chip. When two Gather-X detectors are used, the X-ray sensitivity is doubled. This advantage provides mapping of a 30 nm tantalum (Ta) layer only in minutes. Multiple Gather-X detectors provide another benefit. When using one EDS detector, X-ray maps may show shadow artifacts due to specimen topography. The shadow artifacts are minimized by using two Gather-X EDS detectors positioned at opposite angles.

Fig. 8 Analysis example of solid-state lithium-ion battery.

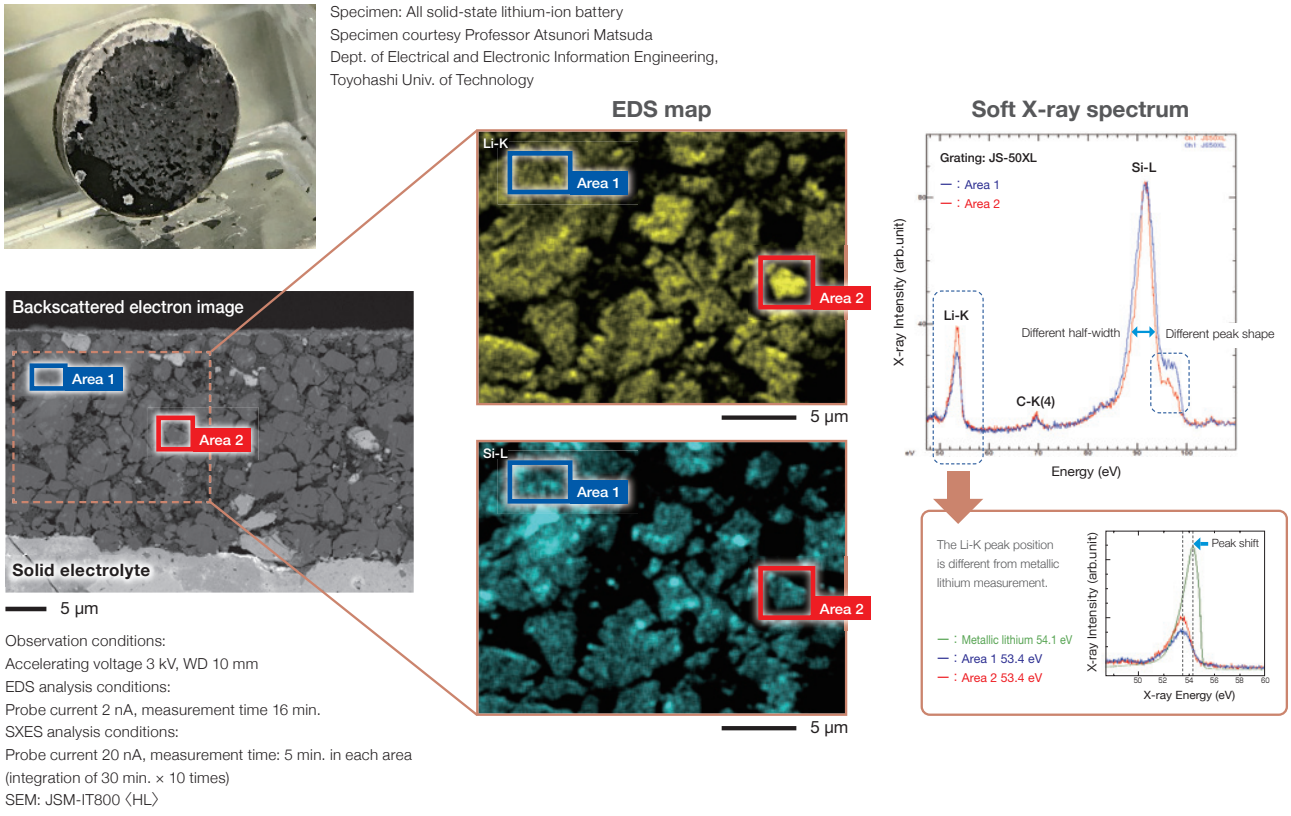

Fig. 9 Analysis example of silver (Ag) nanoparticles (photocatalyst) on titanium oxide.

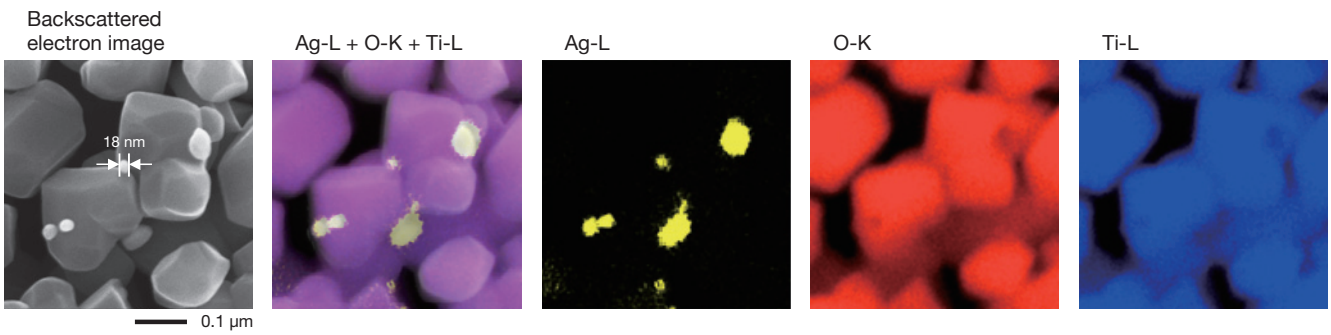

Specimen: Ag nanoparticles on titanium oxide
SEM: JSM-IT800<SHL>
Analysis conditions: Accelerating voltage 5 kV, BD mode (bias to specimen) –5 kV, WD 4 mm, Probe current 1 nA, Measurement time: 9 min.

Analysis of cellulose containing inorganic materials

The use of multiple Gather-X detectors improves detection efficiency, allowing for fast EDS analysis at low probe currents. Thus, electron beam damage to a beam sensitive specimen (organic material, etc.) is suppressed. **Figure 11** shows EDS maps of cellulose containing inorganic materials acquired using one detector and three detectors. In EDS analysis using one detector, it was confirmed that the surface of a specimen was damaged by irradiation of an electron beam after analysis. But with three Gather-X detectors, the probe current was reduced by one third while maintaining the same input count rate as one detector, demonstrating a suppressed electron beam damage to the specimen during EDS analysis.

Conclusion

This article has presented the development status, features and analysis examples of the Gather-X. This Gather-X is an innovative EDS instrument, allowing greater capabilities and is not a simple higher-end model of JEOL EDSs. With its capability of high sensitivity analysis for all energy regions of characteristic X-rays, high spatial resolution elemental mapping, and high usability and safety operation, the Gather-X is expected to be used for even wider applications, including detection of characteristic X-rays from lithium which is not possible to analyze with most EDS detectors.

Furthermore, as a screening analysis tool for other analytical attachments, such as WDS, SXES, CL (cathodoluminescence) and EBSD, the Gather-X will serve as part of essential technical tool to perform more sophisticated analyses.

Acknowledgments

We are grateful to the efforts of the project members to develop the Gather-X and all other people involved. We would like to extend our sincere gratitude to Professor Atsunori Matsuda and Dr. Reiko Matsuda at Toyohashi University of Technology for generously providing the samples of solid-state lithium-ion battery.

References

[1] N. Inoue, *Microscopy TODAY* **32** (2024) https://doi.org/10.1093/mictod/qaae026

[2] Yoshikazu Nemoto, Yohei Kojima, “New models of JEOL general-purpose SEMs –Advancement of user experience provided by high operability–”, *Nihondenshi News* (2024) **56**(1) 39-46 (in Japanese).

Fig. 10 Analysis example of multi-layers on an IC chip cross section.

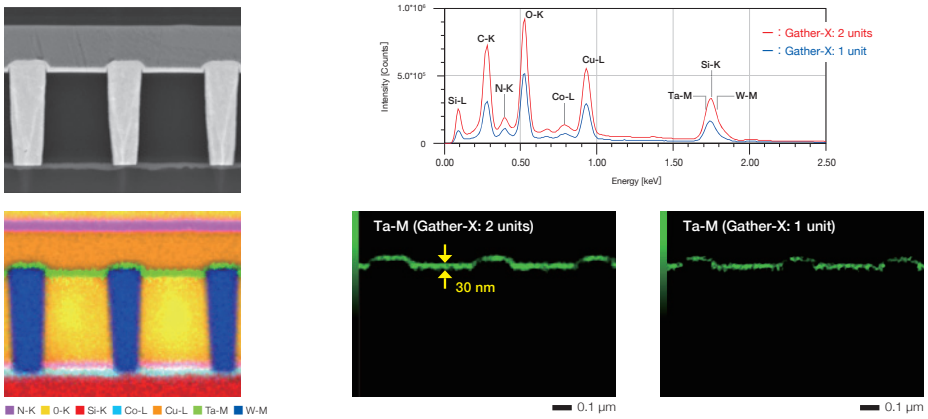

Specimen: IC chip cross section (prepared using CP)
SEM: JSM-IT800<is>

Analysis conditions: Accelerating voltage 3.5 kV (maximum specimen bias voltage: –2 kV)
WD 8 mm, probe current 0.9 nA, measurement time 8 min.

Fig. 11 Analysis example of cellulose containing inorganic materials.

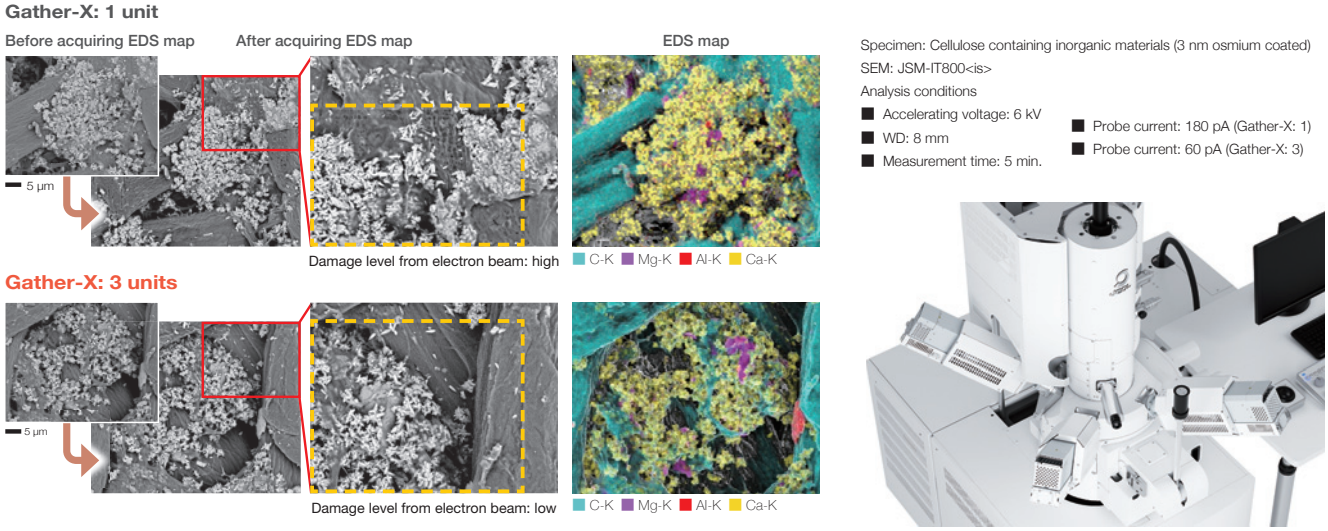

Specimen: Cellulose containing inorganic materials (3 nm osmium coated)
SEM: JSM-IT800<is>
Analysis conditions
- Accelerating voltage: 6 kV
- WD: 8 mm
- Measurement time: 5 min.
- Probe current: 180 pA (Gather-X: 1)
- Probe current: 60 pA (Gather-X: 3)

BSE images showing an alteration phase in a Haversian canal (a) and in bone cavities (b).

Introduction of the New Cryo-FIB-SEM "CryoLameller"

Rintaro Kawano[1], Wataru Shigeyama[2], Hideki Matsushima[1], Naoki Hosogi[3], Chikako Nakayama[4], Katsuyuki Suzuki[4], Noriaki Mizuno[1]

[1] EP Business Unit, JEOL Ltd. [2] JEOL USA, Inc. [3] EM Business Unit, JEOL Ltd. [4] Solution Development Center, JEOL Ltd.

This paper introduces the newly developed Cryo-FIB-SEM system "CryoLameller," designed to enhance the efficiency of milling cryo-hydrated samples into lamellae and subsequent Cryo-Electron Tomography. CryoLameller features stable sample transport to prevent temperature rise and frost formation, a highly stable cryo-stage to minimize thermal drift, and seamless integration with optical microscopes and TEM. These capabilities ensure efficient data acquisition while preserving sample quality. Additionally, CryoLameller supports various sample preparation techniques, accommodating diverse research needs and enabling advanced cryo-electron microscopy analyses.

Introduction

The Cryo-Transmission Electron Microscope (Cryo-TEM) is used to observe frozen samples at ultra-low temperatures. Its ability to maintain the frozen state even in a vacuum environment makes it ideal for the structural analysis of biological samples containing water and polymer materials sensitive to electron beams and heat. By freezing the samples, the need for chemical fixation, commonly used for soft materials, is eliminated, preventing sample denaturation due to chemical reactions and allowing observation in a state close to the original structure.

For three-dimensional (3D) structural analysis using Cryo-TEM, two main methods are utilized: Single Particle Analysis (SPA) and Cryo-Electron Tomography (Cryo-ET). SPA handles purified samples such as proteins, nucleic acids, and viruses. It collects numerous two-dimensional projection images of uniform samples preserved in thin ice films to reconstruct 3D structures. Cryo-ET, on the other hand, obtains 3D structures by reconstructing multiple images taken at different angles of the frozen sample (**Fig. 1**). This method is applicable to heterogeneous samples such as tissues, intracellular structures, and polymer materials.

In both methods, due to the inherent characteristics of TEM, the electron beam must penetrate the sample. At an accelerating voltage of 300 kV, the sample thickness is limited to a maximum of approximately 300 nm. SPA targets samples in aqueous solutions, making it easy to prepare samples with thin film thickness. However, biological tissues and cells targeted by Cryo-ET often exceed 300 nm, limiting measurements to thin regions such as the periphery of cultured cells [1].

The advancement of Cryo-Focused Ion Beam-Scanning Electron Microscope (Cryo-FIB-SEM) technology, which allows precise microfabrication while maintaining the frozen state, has enabled the preparation of various sample lamellae [2]. This has rapidly expanded the applicability of Cryo-ET.

This paper introduces the features of the latest Cryo-FIB-SEM system, "CryoLameller," and presents application examples of intracellular structure and polymer material analysis obtained using this device.

Fig. 1 Overview of electron tomography.

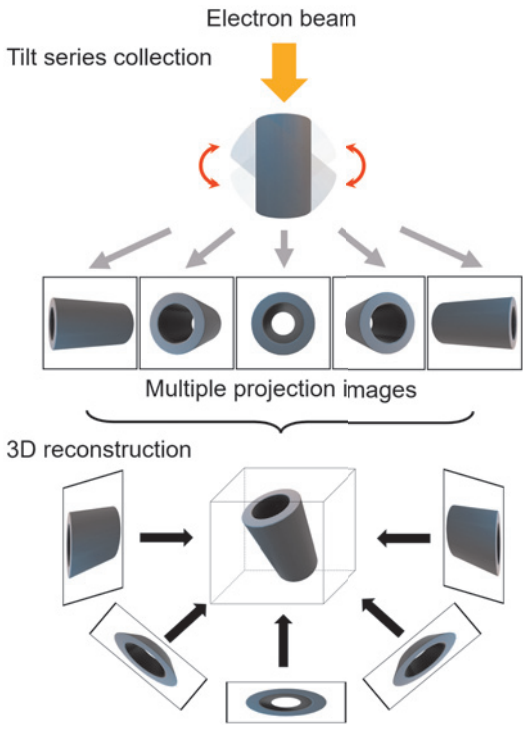

By tilting the sample within the electron microscope and capturing images from different angles, projection images are acquired. These images are then back-projected to reconstruct a 3D image.

〉〉 3-1-2, Musashino, Akishima, Tokyo, 196-8558, Japan | E-mail: rkawano@jeol.co.jp

Development Concept of CryoLameller

CryoLameller was developed to streamline the workflow from lamella preparation using FIB to observation using TEM. It is designed to be highly compatible with the CRYO ARM™ system, specifically for Cryo-TEM. The system operates by mounting the sample-loaded grid onto a dedicated cartridge (**Fig. 2**).

This cartridge is designed to meet the needs of Cryo-TEM methods, such as SPA, which require large-scale data acquisition. In the CRYO ARM™ system, this cartridge enables automatic sample loading and continuous data collection from multiple grids.

CryoLameller uses the same cartridge as the CRYO ARM™, facilitating the integration of FIB processing and TEM observation. Additionally, by allowing the same cartridge to be used with a cryo-stage for optical microscope observation, it enables seamless integration between the optical microscope, CryoLameller, and CRYO ARM™. Thus, CryoLameller was developed with the concept of integrating the entire cryo-workflow around the cartridge and significantly improving the operational efficiency of cryo-electron microscopy.

Features of CryoLameller

1. Operation using Cartridges

The use of cartridges offers several advantages. Firstly, it significantly simplifies handling in liquid nitrogen. The samples are frozen on 3 mm diameter copper grids. In the traditional method, handling these grids directly with tweezers makes them prone to deformation. However, securing the grids within a cartridge effectively prevents the deformation. Additionally, the cartridge's shape makes it easy to handle with tweezers, allowing for quick operation and reducing the risk of frost formation during handling.

Furthermore, the cartridge has narrow and flat shape, allowing the transfer of samples processed by FIB to TEM without changing their orientation. This design ensures that lamellae prepared by FIB always face the optimal direction for Cryo-ET, making sample alignment in Cryo-TEM easier. Additionally, the cartridge's sufficient thermal capacity helps maintain a stable temperature during transfer, preserving sample quality. These features enable a simple and efficient cryo-workflow from sample handling to data acquisition.

2. Highly stable cooling stage

CryoLameller has high stage stability at cooled state by adopting a cooling method based on thermal conduction rather than gas flow. This design minimizes sample drift at cooled state, achieving stage stability comparable to that at room temperature, thus enabling high-magnification observations.

Additionally, its excellent thermal insulation reduces liquid nitrogen consumption, enabling overnight operation and long-duration automated processing, thereby reducing the operational burden. Despite using thermal conduction, it is equipped with a rotation mechanism, allowing for the extraction of block samples and preparation of lamellae in any orientation using the Cryo Lift-out method described later.

3. Anti-contamination device inside the column

Generally, in cryo-SEM, a cooling shield is placed inside the sample chamber to prevent ice contamination on the sample. In addition to this, our company has confirmed that placing an anti-contamination device (ACD) inside the SEM column achieves even higher effectiveness. The typically challenging installation of an ACD in the column was made possible through our in-house development. This innovative design has successfully minimized ice contamination to an extremely low level.

4. Minimizing ice contamination with an integrated coating device

Samples embedded in ice have poor electrical conductivity, necessitating conductive coating before SEM observation. CryoLameller is equipped with a sub-chamber that includes a sputter coating device, eliminating the need to transfer samples to a dedicated coating device. Reducing the number of sample transfers minimizes the risk of ice contamination, thereby improving sample quality.

CryoLameller Workflow

A standard cryo-workflow is shown in **Fig. 3**. After rapidly freezing the sample, it is mounted onto a cartridge. The cartridge is then transferred to an optical microscope, CryoLameller, or CRYO ARM™. The sample is attached to the cartridge using the CRYO ARM™ Workstation, and the installation and removal of the cartridge to and from the cryo transfer holder are

Fig. 2 Concept of operation using CRYO ARM™ cartridge.

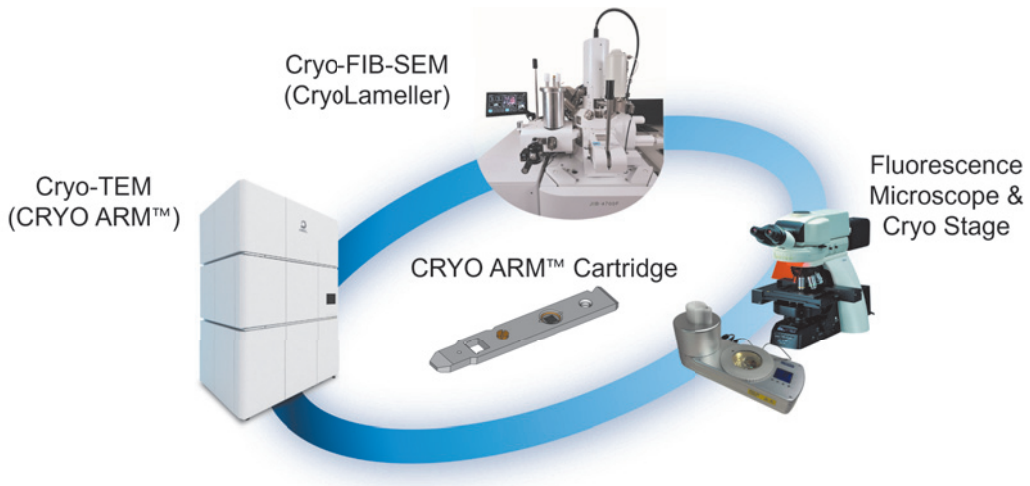

The process of sample transfer and observation using the dedicated CRYO ARM™ cartridge.

performed using the Holder Workstation.

The cryo transfer holder used for sample transportation can also function as a TEM holder. Therefore, when observing lamellae prepared by CryoLameller with a general-purpose Cryo-TEM other than CRYO ARM™, it is possible to observe the sample in a cooled state while it remains mounted on the holder.

Enhanced Target Identification in Cryo-CLEM

Cryo-TEM samples are embedded in amorphous thin-film ice, and the biological or polymer samples to be measured are mostly composed of light elements. Therefore, it is often difficult to identify target areas using only SEM images that show surface topography or compositional differences. Thus, it is necessary to pre-identify the location using an optical microscope [3]. By mounting the cartridge on an optical microscope cryo stage (manufactured by Linkam Scientific Instruments), it is possible to perform Correlative Light-Electron Microscopy (CLEM) under cryogenic conditions. The optical microscope cryo stage, CryoLameller, and CRYO ARM™ can share stage position information, allowing the identification of fluorescently labeled targets with the optical microscope, followed by thin sectioning with FIB and observation with TEM.

Figure 4 overlays the fluorescence image and SEM image of a fluorescently labeled nucleus in HeLa cells.

Various Processing Methods

CryoLameller supports a variety of processing and observation techniques, enabling it to handle samples of various sizes and shapes.

1. Lamella preparation on grid

This method is primarily applied to plunge-frozen samples and other thin samples with a thickness of less than 50 µm [4].

Fig. 3 Standard cryo workflow using CRYO ARM™ cartridge.

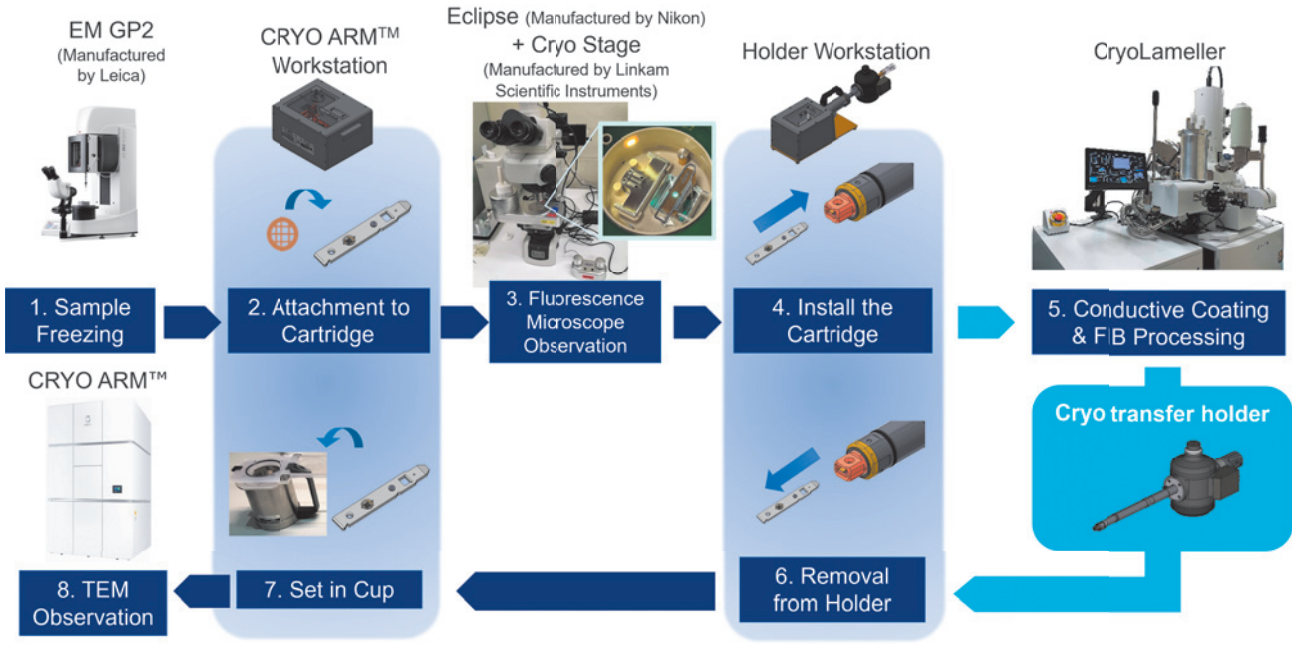

1. Rapidly freeze the sample.
2. Attach the grid with the sample into the dedicated CRYO ARM™ cartridge.
3. Observe the sample using a fluorescence microscope with a cryo stage.
4. Install the cartridge into the cryo transfer holder, store it inside to prevent frost formation, and transport it.
5. Insert the sample into the CryoLameller for coating, observation, and processing.
6. Remove the processed sample from the CryoLameller with the cryo transfer holder, and uninstall the cartridge.
7. Transport the processed sample using the CRYO ARM™ transport cup.
8. Observe the sample with the CRYO ARM™.

Fig. 4 Correlative observation with fluorescence microscopy and SEM.

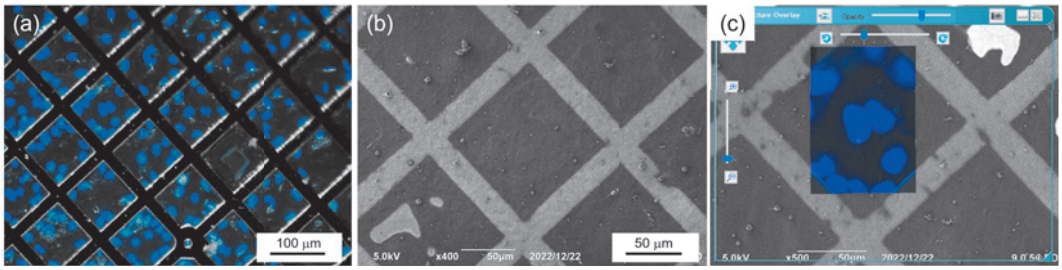

(a) Fluorescence microscope image of HeLa cells cultured on a grid. The nuclei are stained blue (Hoechst staining). (b) SEM image of the same grid. (c) Overlay of images (a) and (b).

By tilting the sample and directing the ion beam at a shallow angle of approximately 70° from the normal to the grid surface, a lamella is created by milling both the top and bottom to open a "window" (**Fig. 5**a, b). The lamella is supported by bulk material on the sides, allowing direct observation with Cryo-TEM. Figure 5c shows the results of 3D reconstruction of ink-based materials using this method.

Ink-based materials have high viscosity, making it difficult to apply them thinly on a grid. Reducing the viscosity with a solvent changes the composition ratio of the material, making it impossible to measure the 3D distribution. On the other hand, by using the CryoLameller, it is possible to create lamellae while maintaining the 3D distribution of the material. This allows the analysis of the 3D distribution of carbon black and resin emulsion in liquid using Cryo-ET.

2. Cryo lift-out

This method is applied to thick samples such as high-pressure frozen samples [5]. First, the desired observation area is cut out from the bulk sample into a block using FIB and extracted with a cryo-manipulator (Fig. 5d). The extracted block is then attached to a FIB grid and thinned (Fig. 5e). The prepared lamella can be observed with Cryo-TEM.

Using this method, high-pressure frozen yeast was observed, as shown in Fig. 5f. Cryo-TEM observation was possible at any desired location within the thick sample. The stable stage made it easy to pick up the sample.

3. Slice & View with FIB-SEM

This method involves repeatedly alternating between cutting cross-sections with FIB and observing them with SEM to perform 3D reconstruction (Fig. 5g, h) [6]. It is suitable for reconstructing large volumes, and Fig. 5i shows the result of reconstructing a single yeast cell.

Although it is not possible to observe entire yeast cells with a thickness greater than 3 µm using TEM, this method allows for the elucidation of the 3D structure of the entire cell. The sizes and distributions of mitochondria, nuclei, and lipid droplets were analyzed in detail. Additionally, the high stage stability of the CryoLameller enabled long-duration measurements without any issues.

Conclusion

The CryoLameller is an innovative Cryo-FIB-SEM system designed for more convenient and efficient Cryo-TEM observation. This is achieved through the use of dedicated cartridges for easy sample transfer, a cooling stage with excellent stability, and unique anti-contamination technology to reduce ice contamination on the samples. Additionally, it supports various sample processing methods and CLEM, making it applicable to a wide range of samples.

The handling of frozen samples has become significantly simplified, enabling efficient data acquisition. We hope that this Cryo-FIB-SEM system will contribute to advancements in research across various fields, including biology and materials science.

References

[1] Medalia, O., Weber, I., Frangakis, A.S., Nicastro, D., Gerisch, G. & Baumeister, W. *Science* **298**, 1209–1213 (2002).

[2] Marko, M., Hsieh, C., Schalek, R., Frank, J. & Mannella, C. *Nat. Methods* **4**, 215–217 (2007).

[3] Scher, N., Rechav, K., Paul-Gilloteaux, P., & Avinoam, O. *iScience* **24**, 102714 (2021).

[4] Rigort, A., Bäuerlein, F.J., Villa, E., Eibauer, M., Laugks, T., Baumeister, W., & Plitzko, J.M. *Proc. Natl. Acad. Sci. U.S.A*. **109**, 4449–4454 (2012).

[5] Schaffer, M., Pfeffer, S., Mahamid, J., Kleindiek, S., Laugks, T., Albert, S., Engel, B.D., Rummel, A., Smith, A.J., Baumeister, W. & Plitzko, J.M. *Nat. Methods* **16**, 757–762 (2019).

[6] Schertel, A., Snaidero, N., Han, H., Ruhwedel, T., Laue, M., Grabenbauer, M. & Möbius, W. *J. Struct. Biol*. **184**, 355–360 (2013).

Fig. 5 Various processing techniques and results.

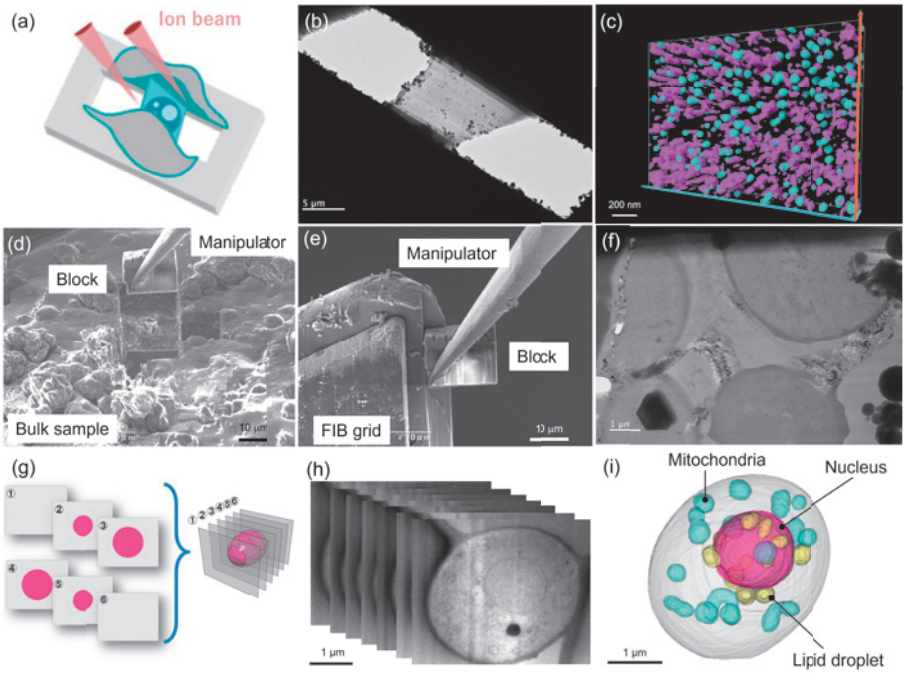

(a) Schematic of lamella preparation on a grid.
(b) TEM image of ink-based material.
(c) 3D reconstruction of ink-based material by Cryo-ET, showing carbon black (pink) and resin emulsion (light blue).
(d) Block cut from high-pressure frozen yeast and attached using a cryo-manipulator.
(e) Block attached to a FIB grid.
(f) TEM image after thinning (e).
(g) Schematic of the Slice & View method using FIB-SEM.
(h) Serial sections of yeast.
(i) 3D reconstruction of yeast by Slice & View, showing mitochondria (light blue), nucleus (pink), and lipid droplets (yellow).

Advancement of Technological Development of an Electron Beam Metal 3D Printer JAM-5200EBM

Masahiko Iida, Ayumi Miyakita, Kozo Koiwa,
Nari Tsutagawa, Yohei Daino, Satoshi Ono, Takashi Sato
IS Business Unit, JEOL Ltd.

We have succeeded in developing a new electron beam metal (EBM) 3D printer JAM-5200EBM and began the sales of this machine in March 2021. We contributed a paper for JEOL News 2022 issue to introduce the features and functions of the JAM-5200EBM, and simple application examples using our EBM machine.

Since then, the additive manufacturing industry has changed and advanced over time. This paper presents our recent development progress of the 3D printing technology using the JAM-5200EBM, including hardware development, compliance with an industry material standard, and application examples for various metal materials built by our 3D printer.

Introduction

In recent years as a new manufacturing technology, practical use of additive manufacturing has been progressing, especially in USA and Europe. In particular, the Powder Bed Fusion (PBF) method, in which thermal energy selectively fuses regions of a powder bed to manufacture, can print 3D structure parts having excellent mechanical properties compared to traditionally manufactured materials. Furthermore, the PBF method makes it possible to print parts from materials that are difficult to manufacture with conventional methods. Thus, practical applications using this method have been utilized widely in the industries of aerospace and medical device field.

The PBF method is classified into two types according to the difference in the heat source: LB (Laser Beam)-PBF and EB (Electron Beam)-PBF. **Table 1** compares two methods with the same printing area. The beam output of the electron source in the EB-PBF system is up to 6 kW, indicating that the maximum output is 6 times higher than that obtained with the conventional LB-PBF system (laser source: 1 kW maximum). With regards to the beam deflection speed, LB-PBF has a few m/s but EB-PBF achieves a greatly high speed of a few 1,000 m/s. This is because

Table 1 Comparison between EB-PBF and LB-PBF (single beam).

	EB-PBF (JAM-5200EBM)	LB-PBF
Preheat	Essential (small residual stress)	None or Auxiliary (large residual stress, support essential)
Max. beam output	6 kW	0.4 to 1 kW
Beam deflection	Electromagnetic deflection	Mechanical deflection (by Galvanometer mirror)
Beam scan speed	Max: a few 1,000 m/s	Max: a few m/s
Heat input efficiency	80% or more for most metal materials	Largely differs depending on metal material and laser type. 5 to 40% for generally used fiber lasers
Build speed	a few 10 to 100 cc/h	about 10 cc/h
Build atmos.	Vacuum	Inert gas
Roughness of build object	Sa: 20 to 40 um	Sa: 10 um
Powder charging	With charging (preheat needed to suppress charging)	No charging
Powder removal	Blasting needed to remove pre-sintered body (difficult to create water pipe & complex shape)	Easy to remove powders (possible to create water pipe & complex shape)

〉〉 3-1-2, Musashino, Akishima, Tokyo, 196-8558, Japan | E-mail: masiida@jeol.co.jp

LB-PBF uses mechanical control using a Galvanometer mirror to deflect laser beams, whereas EB-PBF adopts electromagnetic deflection to deflect electron beams.

Comparing the heat conversion efficiency between two methods, EB-PBF has higher efficiency than LB-PBF. Laser is an electromagnetic wave that possesses monochromaticity, directivity and coherency (phase/wavelength/direction aligned), and laser irradiation onto an object causes absorption, transmission and reflection of laser energy on the object surface. Therefore, the laser wavelength (~1,000 nm) used for the general LB-PBF system gives rise to large energy reflection on the metal surface. For example, the heat conversion efficiency for iron (Fe), nickel (Ni) and tungsten (W) is 30 to 40%, and for aluminum (Al) and copper (Cu), the efficiency is as low as 10% or below [1]. Such a low heat conversion efficiency is a disadvantage of LB-PBF and another problem is the efficiency is largely different depending on the material type. On the other hand, EB-PBF has the following advantages. An electron beam is formed by convergence of electrons and has masses and an electric charge. The electrons irradiated on an object interact with the object. Among these electrons, about 1% electrons result in the emission of X-rays and secondary electrons; however most of the electrons is used to heat the object and to generate (emit) backscattered electrons (BSE). As the atomic number is larger, BSE emission becomes larger. The heat conversion efficiency by electron beam irradiation is as high as 70 to 80% for generally used metals (atomic number being relatively small), and also 60% even for heavy metals such as tungsten [2]. Another advantage of EB-PBF compared to LB-PBF is that the efficiency is similar depending on the material type, in combination with an overall high efficiency.

As described, since EB-PBF provides high heat conversion efficiency, this method has started to be used for research & development and practical-use development in printing high melting-point materials (exceeding 3,000 °C) and materials difficult to melt by laser beam due to high reflectivity. Under this circumstance, hardware which enables efficient and speedy development of material and recipe, is significantly needed from the viewpoint of researchers.

In industries where high performance parts are built using EB-PBF, the standardization of productivity, stability and reproducibility in additive manufacturing has been progressing. This has resulted in the development of standards in which conformance is required in order to certify products complying with industry requirements. Furthermore, not only are required standards growing but an increased demand for in-process monitoring systems to omit inspection steps after the printing process.

In the next Chapters, this paper introduces our development of new hardware units adaptable to the above-mentioned needs (A. small-scale production option unit, B. backscattered electron (BSE) image monitoring & defect detection system), compliance with the AMS7032 Operational Qualification standards by Ti-6Al-4V alloy, and the development status for several metals using the JAM-5200EBM (1. pure copper, 2. Ni718 alloy, 3. pure tungsten).

Development of New Hardware Units

A. Small-scale production option unit

The standard unit on the JAM-5200EBM is configured for industry use, and requires a large volume of powder due to the large build area of 250 mm in diameter. But in the development of new materials for research use, it is recommended to use a small volume of powder. To meet this need, we developed a small-scale production option unit which is configured by attaching a small build tank to the JAM-5200EBM. This small option unit can print a build with a small volume of powder, enabling reduction of the build area to 60 mm in diameter. **Figure 1**(a) shows the newly developed small-scale production option unit (left) and the standard unit (right). When building a product with the same height, the use of the small option unit allows for building with a smaller volume of powder, 20 to 30% lower than the powder volume with the standard unit.

In addition, some specifications for this small option unit were modified, that is, addition of heat resistant property to a heat shield and a build tank, thus making it possible for the JAM-5200EBM with the option unit to build a Ni718 alloy and high melting-point materials (e.g. tungsten) that require a preheat temperature exceeding 1,600 °C. Currently, we are proceeding with the process development of these materials. Figure 1(b) shows an example of a part built by the modified small-scale production option unit.

B. Backscattered electron (BSE) image monitoring & defect detection system

In the PBF method, there is a theoretical possibility that, defects originating from low powder filling-rate (50 to 60%) and inside-powder are formed, and depending on the molten state, the defects may extend to 400 μm or larger in size. It has been determined that those size-oriented defects adversely affect the mechanical property of the built material even after hot isostatic pressing (HIP) is applied after 3D printing. These defects can be first confirmed by non-destructive inspection after the printing, allowing for judgement of whether the defect is acceptable or non-conforming. However, with one of non-destructive methods of X-ray CT, there is a limitation on inspection. That is, as the mass of the element contained in the material is heavier, it is difficult

Fig. 1 Comparison between the small-scale production unit and the standard unit.

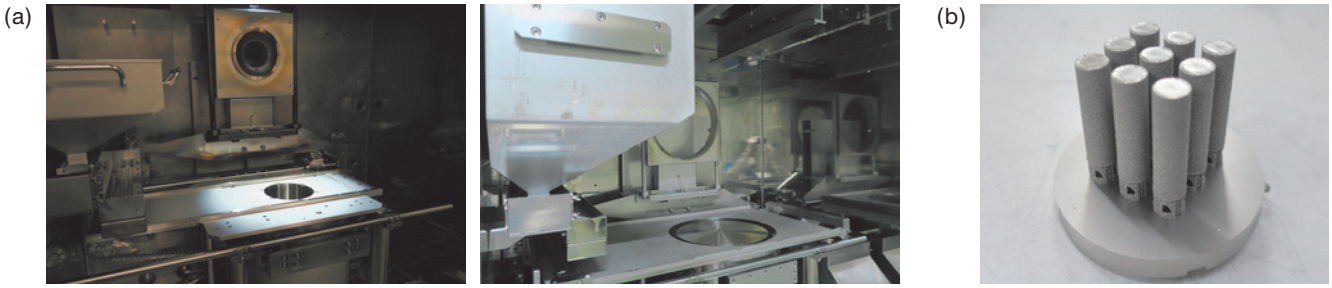

(a) Small-scale production option unit (left) and Standard unit (right), (b) Example of a build object (Ni718 alloy-based cylinder: 10 mm dia. × 50 mm).

to transmit X-rays into the material. Due to this limitation, the printed builds of pure copper, Ni alloy, tungsten, etc., for which EB-PBF can efficiently build (LB-PBF has difficulties with these materials), cannot be subjected to inspection after the printing. It has been a demand for developing a quality control system that automatically detects such internal defects. For example, if cross-sectional topographic images of the melt process where each layer is acquired for defect detection, this system will become very effective for the materials which were difficult to inspect their internal defects.

Since JEOL has been developing and manufacturing electron microscopes (transmission type, scanning type and other types) over many years, surface observation technique using the electron beam is the core technology of JEOL. We have made efforts to apply this electron beam technology to develop a BSE image monitoring & defect detection system. The new system utilizes an electron source incorporated in the JAM-5200EBM for acquiring BSE cross-sectional images for all layers in the build. Figure 2(a) shows the photo of the newly developed BSE image monitoring & defect detection system and Fig. 2(b) to (d) show an application example of the system, by comparison with X-ray CT application. BSE signals are detected using four electrodes placed surrounding the build area (**Fig. 2**(a)), then a topographic-enhanced BSE image is acquired (Fig. 2(b)), finally defect candidates are automatically detected from the image (Fig. 2(c)). When comparing the BSE image with an image obtained by X-ray CT from the same field of view (Fig. 2(d)), the defect sites are in good agreement between two images.

Currently, an upgraded version of this monitoring & defect detection system is under final testing for commercialization. When this system is released and installed into a JAM-5200EBM, the following capabilities will be accessible: By acquiring cross-sectional BSE images from all layers in the 3D printing process, it will become possible to control the quality of the build parts simultaneously with controlling the build process, thus making the printing process of the EB-PBF techniques highly efficient. In the future, the new product will quickly melt again and restore a defect site detected in the printing process, thus largely contributing to the improvement in manufacturing yield using EB-PBF printing.

Compliance with AMS7032 Operational Qualification by Ti-6Al-4V Alloy

Upon establishing the USA demonstration center for the JAM-5200EBM [3], we performed Operational Qualification (OQ) testing for AMS7032 [4], one of material standards of Aerospace Material Specifications (AMS), for which SAE International (USA) stipulates in order to comply with specifications in the industrial standard for aerospace parts that are 3D-printed using the PBF system. It should be noted that AMS7032 is the main international standard for additive manufacturing. The JAM-5200EBM was subjected to OQ testing to evaluate the quality and repeatability of printed parts with a Ti-6Al-4V alloy. The JAM-5200EBM was verified to fully meet the AMS7032 requirements, using AMS7011 minimum material properties for the Ti-6Al-4V alloy.

We describe the details of the OQ procedure which was performed in verifying the compliance with the AMS7032 OQ standards for the JAM-5200EBM.

(1) Ti-6Al-4V alloy (Grade 5) was prepared as the material (powders).
(2) AMS7032 OQ test build was prepared by placing specimens (coupons) throughout the maximum build area (250 mm dia. × 400 mm) (**Fig. 3**a).
(3) Using the test build in (2) above, the OQ test was conducted several times to evaluate the repeatability of the build (Fig. 3b, test specimens).
(4) For the build test specimens, tests of tensile strength, elemental analysis and density measurement were conducted, then the AMS7011 material requirements [5] were used to evaluate compliance.

In this OQ testing, multiple test specimens (coupons) were built all at once in the same build. Among those specimens, tensile tests were conducted in three directions of X/Y/Z by extracting 10 specimens per test. **Table 2** lists the OQ test result according to AMS7032. All of the test specimens subjected to tensile tests were verified to meet the AMS7011 material requirements for tensile strength.

Ti-6Al-4V, the material leading to compliance with the OQ procedures listed in AMS7032, has high specific strength and high corrosion resistance; therefore it is utilized in the additive manufacturing field for producing aerospace parts and medical implants. Although the Ti-6Al-4V alloy causes remarkable deformation due to thermal distortion, EB-PBF provided by the JAM-5200EBM is equipped with an efficient preheat function and can suppress thermal distortion based deformation. Owing to these capabilities, as shown in **Fig. 4**, even when multiple parts (artificial hip joint) are stacked, high dimensional accuracy and high quality are maintained. Compared to LB-PBF, EB-PBF is advantageous for volume 3D printing.

Figure. 5(a) shows part of the artificial hip joint (in Fig. 4) which was printed using the JAM-5200EBM. Each printed part from a Ti-6Al-4V alloy using our 3D printer achieves a surface roughness (Sa) lower than 30 μm at its side surface. Figure 5(b)

Fig. 2 Backscattered electron (BSE) image monitoring & defect detection system.

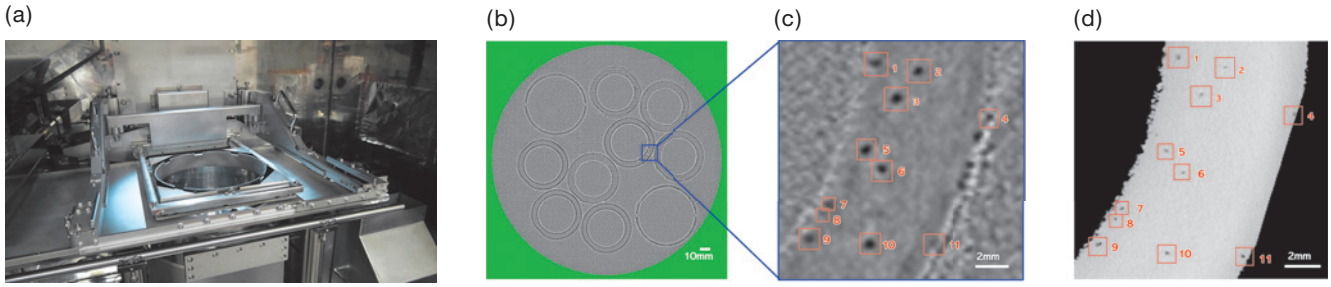

(a) Photo of electrodes surrounding the build area at the center, (b) BSE image (topographic-enhanced image), (c) Enlarged BSE image of the defect sites, (d) X-ray CT image of the defect sites.

shows a SEM image of a mesh-structured object (width: 0.5 mm) located on the top of the hip joint shown in Fig. 5(a). Since the bone tissues are fixed by naturally growing in the mesh structure, the mesh-structured object is an important part in the artificial hip joint. It is confirmed that the JAM-5200EBM has a sufficient performance to build such a precise object, that is, a mesh structure with a size smaller than 1 mm (Fig. 5(b)).

Development Status for Several Metal Materials

1. Pure copper

Pure copper has physical characteristics of high thermal conductivity and high electrical conductivity. Therefore, pure copper is used in fields such as heat exchangers and electrical wiring where its physical properties are utilized. In the field of additive manufacturing, design optimizations are being implemented to make these physical structures more efficient. For example, extremely high heat exchange rates will be expected by designing a heat exchanger with a sophisticated shape, which is difficult to manufacture using conventional methods. Also for products like EV motor and high frequency induction heating coil, it is expected that by optimizing the design and using the advantages of EB-PBF system, the resulting parts will further optimize the physical characteristics of pure copper.

On the other hand, there are challenges in 3D printing of pure copper. That is, a crack can occur due to hydrogen embrittlement, and sintered powder is encapsulated inside the part when building a hollow structure. In the initial development of our electron beam metal 3D printer, grain boundary cracking occurred due to hydrogen embrittlement (**Fig. 6**b left). At that time, IACS (International Annealed Copper Standard) conductivity, one of characteristics of pure copper, did not reach 100%, resulting in insufficient physical performance. We analyzed that this cracking was originated from the oxygen concentration of the material powder, and we made efforts to choose appropriate material powders and to develop an optimal melting process of those powders. As a result, we developed a process for a printing crack-free part (Fig. 6b right). Then, we made a success in obtaining 100% IACS conductivity when creating test pieces.

Figure 7 shows photos of a high-frequency induction heating coil built by the JAM-5200EBM and the durability test result for the built coil. Conventionally, the high-frequency induction heating coil is created by the process of brazing and bending. The challenge for this process is the durability of the created product (coil). There is a possibility of cracking in the part of brazing and bending, resulting in damage of the part. On the other hand, when building the product (coil) by additive manufacturing, there is no need for brazing and bending, leading to an improved durability of the product. We executed durability testing of the coil which was built by the JAM-5200EBM. The test conditions were heating of 1.5 seconds and cooling of 3 seconds defined to be one cycle

Fig. 3 AMS7032 OQ test build and the built test specimens.

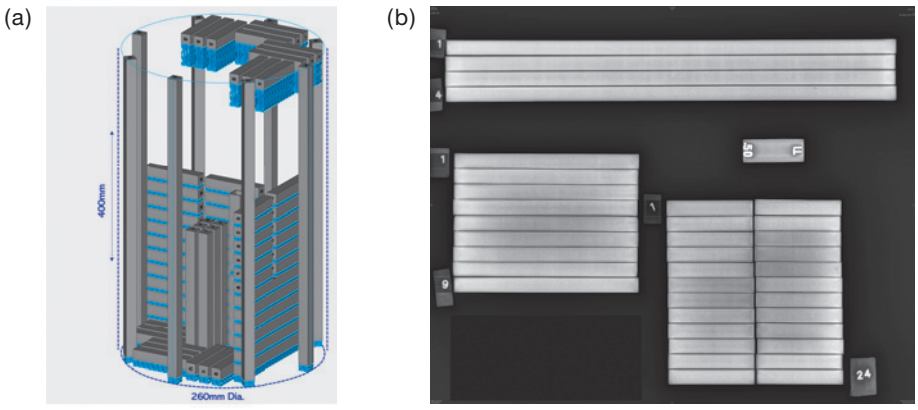

(a) AMS7032 OQ test build,
(b) Test specimens (coupons) built at the OQ test.

Table 2 OQ test (tensile test) result according to AMS7032 OQ standards.

(X/Y Direction)	Ultimate Strength [MPa]	0.2% Yield Strength [MPa]	Elongation [%]
Number of specimen	60		
Maximum	1007	917	19
Minimum	958	821	14
Mean	981	859	17
AMS7011 required	896	772	9

(Z Direction)	Ultimate Strength [MPa]	0.2% Yield Strength [MPa]	Elongation [%]
Number of specimen	30		
Maximum	986	876	21
Minimum	952	834	17
Mean	971	850	19
AMS7011 required	917	827	10

and this cycle was repeated 600 times [6]. The fluctuation of the inner diameter of the coil was only 0.1% or less, demonstrating durability higher than the conventional products.

In the future, we plan to execute measures, for example, remove powders encapsulated in a hollow structure and develop a recipe to print complexed shapes, with an aim of applying the additive manufacturing process to practical-use parts (products).

Fig. 4 Parts of the artificial hip joint stacked and built using Ti-6Al-4V.

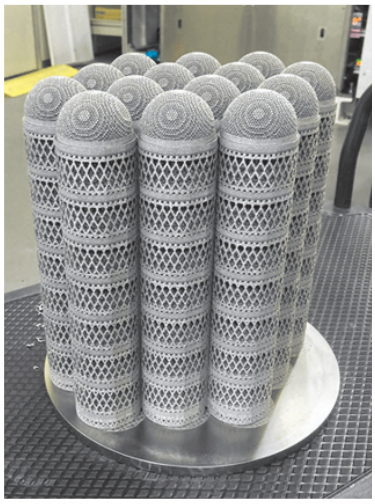

Number of parts: 14 parts × 8 stages = 112

Fig. 5 Parts of the built artificial hip joint laminated using Ti-6Al-4V.

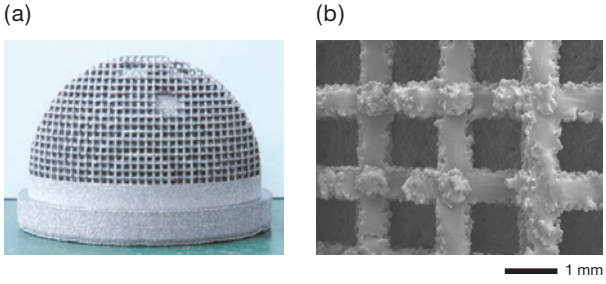

(a) External view, (b) SEM image of a mesh-structured object.

2. Ni718 alloy

Ni718 alloy is most widely used among Ni-based alloys. The alloy has superior high-temperature strength and high creep property; thus in many cases, the alloy is used in high-temperature environments in the fields of aerospace and energy. On the other hand, machining is difficult in manufacturing objects from the Ni718 alloy. In recent years, the use of additive manufacturing technology (EB-PBF) enables design freedom when manufacturing parts, and it is expected that the technology will be applied to the 3D printing of heat resistant materials. Another advantage of the printed products from a Ni718 alloy is that a columnar crystalline grain or an equiaxed crystalline grain can be built while independently demonstrating different mechanical properties depending on the build conditions. For example, we applied creep testing to Ni718 parts in both equiaxed crystalline grain and columnar crystalline grain structures at 650 °C/550 MPa. The creep test result indicated that the creep lifetime for both products were respectively about 400 hours for the equiaxed crystalline grain and 4000 hours for the columnar crystalline grain. A difference in the creep lifetime became as large as 10 times between the two microstructures.

The JAM-5200EBM, with an aim of developing new materials, has a function to set any melting parameters (beam power, beam diameter, beam residence time, scan pitch, etc.). Utilizing this function to print the Ni718 alloy, characteristic metallurgical structures can be obtained selectively. **Figure 8** shows an example of cross sections of microstructure of the printed parts from the Ni718 alloy using the EB-PBF method with the JAM-5200EBM. It is noted that the melting parameters in this 3D printing were changed from "low current/low speed/high pitch (condition A)" to "high current/high speed/low pitch (condition B)" at a build height of 5 mm (half of the total build height of 10 mm). In the bottom section of the printed part using the condition A (shown in Fig. 8 bottom), it was confirmed that a columnar crystalline grain was selectively built while orienting in the [100] direction analyzed by EBSD (electron backscatter diffraction) measurement. In the top section of the printed part using the condition B (shown in Fig. 8 top), it was confirmed that an equiaxed crystalline grain was built while randomly orienting, analyzed by EBSD measurement. These results demonstrate that the desired metallurgical structures can be obtained from the selected areas in the same part by changing the melting conditions during the 3D printing.

As described until now, the EB-PBF technology can control microstructure, and this capability would add mechanical properties adaptable to the purpose of use for the printed parts. Thus, this capability will allow EB-PBF technology to succeed in a variety of 3D printing fields.

Fig. 6 Test cube of pure copper and its microstructures.

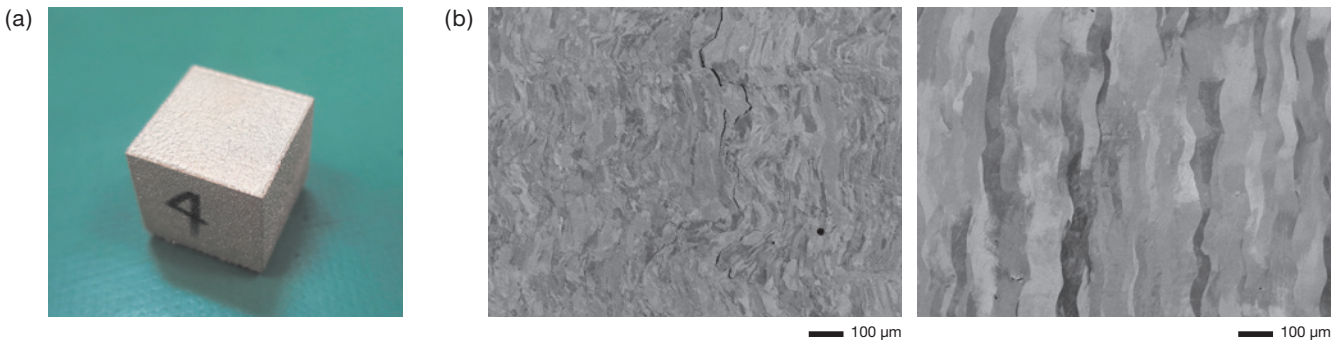

(a) Test cube of pure copper, (b) Its microstructures: (Left) With crack, (Right) With no crack.

3. Pure tungsten

Pure tungsten, as an industrial material with a long history over 100 years, has a wide range of physical characteristics including; high melting point, high hardness, low thermal expansion coefficient, high electrical resistance, abrasion resistance, and radiation shielding ability. Utilizing those characteristics, pure tungsten is used for a variety of materials in a broad range of fields (industries). The materials that are manufactured from pure tungsten include a filament for an incandescent light bulb, parts for a high temperature furnace, a sputtering target, a welding electrode, a cutting tool, a medical catheter, and a collimator for a CT scanner. While the fields to be used include lighting equipment, high temperature furnace, semiconductor, production tool, and medicine. In recent years, pure tungsten is also getting attention as a strong candidate of a diverter plasma facing material in the nuclear fusion field. On the other hand,

Fig. 7 Pure copper-based high-frequency induction heating coil.

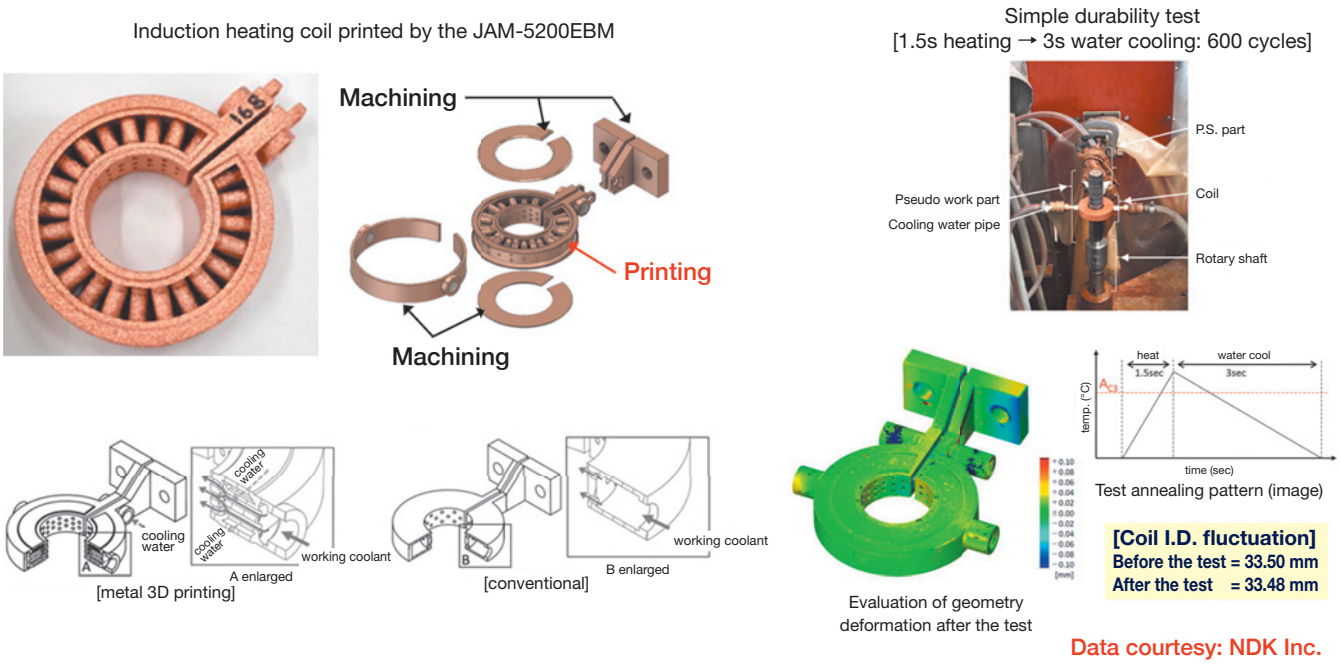

Fig. 8 Microstructures of Ni718 alloy built using the JAM-5200EBM.

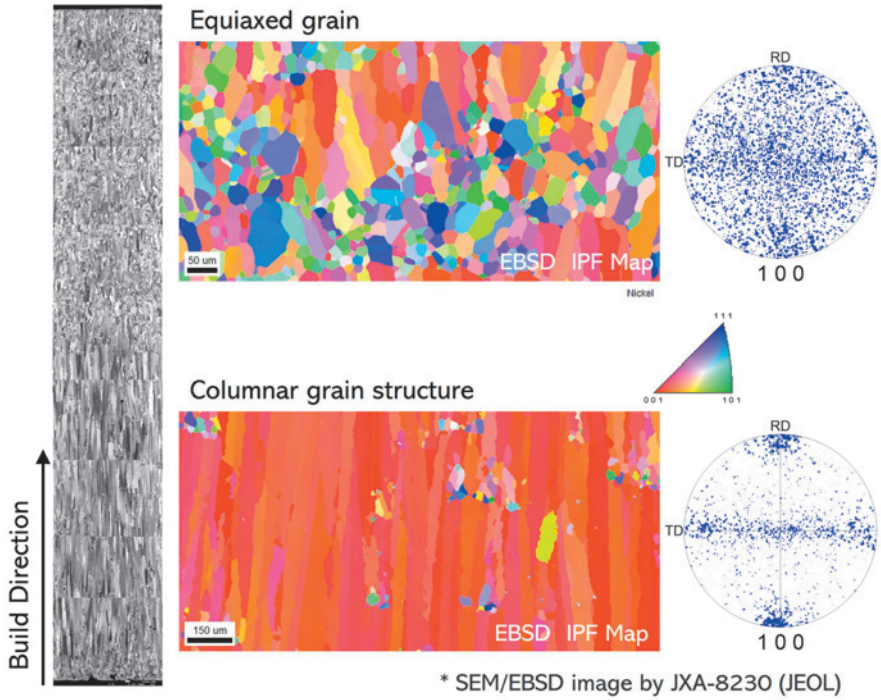

(Top) Equiaxed crystalline grain, (Bottom) Columnar crystalline grain.

there are disadvantages of manufacturing using pure tungsten. That is, tungsten, possessing a body-centered cubic structure, exhibits ductile deformation at high temperature but suffers brittle fracture at a certain low temperature (ductile-brittle transition). Since the temperature for brittle fracture is relatively high, tungsten is broken in a brittle manner even at a few 100 °C; thus conventionally, it is difficult to process tungsten. With powder metallurgy, one of conventional manufacturing methods, simple geometries can only be made successfully. The additive manufacturing technology can build a complex shape with easy processing compared to conventional methods.

However even in additive manufacturing, the LB-PBF and DED (directed energy deposition) methods do not have efficient preheat system; therefore, there are challenges for cracking that occurs due to thermal distortion at coagulation shrinkage of materials and for a difficulty in refining materials. The EB-PBF method is a strong solution. That is, EB-PBF has great characteristics of a hot process and high power beam, leading to a big advantage for 3D printing of pure tungsten.

Figures 9 and **10** show examples of printing practical-use parts from pure tungsten at the maximum preheat temperature higher than 1,600 °C, using the small-scale production option unit for the JAM-5200EBM. With EB-PBF, not only can complicated part designs be printed (Fig. 9) which are difficult to create using conventional processes, but also a lattice structure with a wire diameter of 1 mm and a set of flow paths with a pipe diameter of 5 mm (possible to remove powders in the flow path) (shown in Fig. 10). **Figure 11** shows a cross-sectional photo of a build cube of 10 mm square. The cross section exhibits a columnar structure, demonstrating that EB-PBF enables printing of a part with high density (19.26 g/cm3) and no cracking.

Fig. 9 Examples of tungsten-based printed parts.

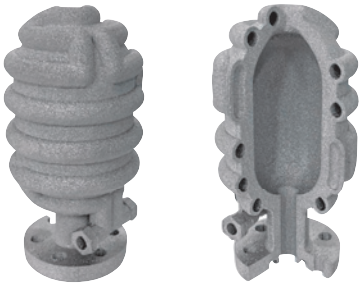

Demonstration parts: 65 mm dia. × 123 mm.

Fig. 10 Examples of tungsten-based printed parts.

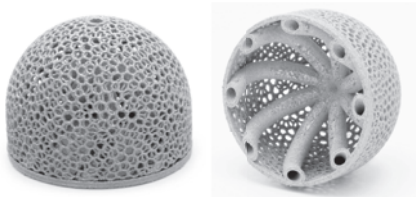

Demonstration parts: lattice structure.

Fig. 11 Cross-sectional photo of a tungsten printed parts.

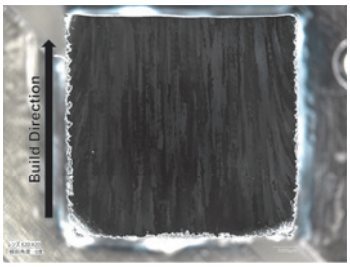

10 mm square cube.

Conclusion

Utilizing the electron beam control technologies which we have cultivated over many years, the JAM-5200EBM enables additive manufacturing with high quality and high reproducibility. The use of our innovative 3D printer makes it possible to merge part designs, reduce manufacturing facility costs, improve manufacturing output, and shortened development periods by applying this 3D printer for building parts for various industries. While LB-PBF has been getting attention in additive manufacturing, EB-PBF has a high possibility to become a "Game Changer" because the electron source provides high speed scanning, high power beam and hot process. Aimed at expanding the application fields of EB-PBF, the challenges are to establish superiority of the technology, ensure profitability, and to strengthen performance and stability in quality through the enhancement of the EB-PBF technology. To proactively tackle these challenges, we are now under aggressive development of the electron beam metal 3D printing product by the pursuit of our long-year cultivated technologies of electron beam scanning and high-resolution imaging. Our development efforts will be incorporated into an initiative for melt scanning and in-process monitoring, as well as introduction of AI technology into the EB-PBF system. Through such efforts, we are determined to continue the evolution of the JAM-5200EBM EB-PBF system.

Acknowledgments

The development of "BSE image monitoring technology" was supported by the accomplishments of "Basic Technology Development Project for Metal Additive Manufacturing Parts" commissioned by NEDO (New Energy and Industrial Technology Development Organization), Japan, from fiscal years 2019 to 2023.

References

[1] E. Spisz, A. Weigund, R. Bowmun, J. Juck: Nasa Technical Report D-5353(1969).
[2] J. Ishikawa: Charged Particle Beam Engineering, CORONA PUBLISHING CO., LTD. (2001), p143-145 (in Japanese).
[3] JEOL Ltd.: https://www.jeol.com/news/pr/20231023.10656.php *In 2024, we established a demonstration center at Technische Universität München, as a European hub.
[4] AMS7032: Machine Qualification for Fusion-Based Metal Additive Manufacturing.
[5] AMS7011: EB-PBF Produced Preforms and Part, Ti-6Al-4V, Hot Isostatic Pressed.
[6] I. Onuma, Y. Koiso: Heat Treatment, 64, 6 (2024) p309-314. (in Japanese).

Introduction of JEOL Products

Schottky Field Emission Scanning Electron Microscope

JSM-IT810

Versatility and high spatial resolution meet automation with the JSM-IT810 series FE-SEM. No-coding automation for imaging and EDS analysis is built-in for a streamlined and efficient workflow. New functions are available to ensure high quality data and an enhanced user experience for all SEM users. Functions include the SEM automatic adjustment package, a trapezoidal correction function (useful for EBSD measurements) and Live 3D surface reconstruction for observation of surface topography. Operating a FE SEM has never been easier with the JSM-IT810 series.

Features

Automatic Observation and Analysis Function "Neo Action"

SEM observation and EDS analysis can be automated by simply setting the analysis conditions and selecting the areas to measure.

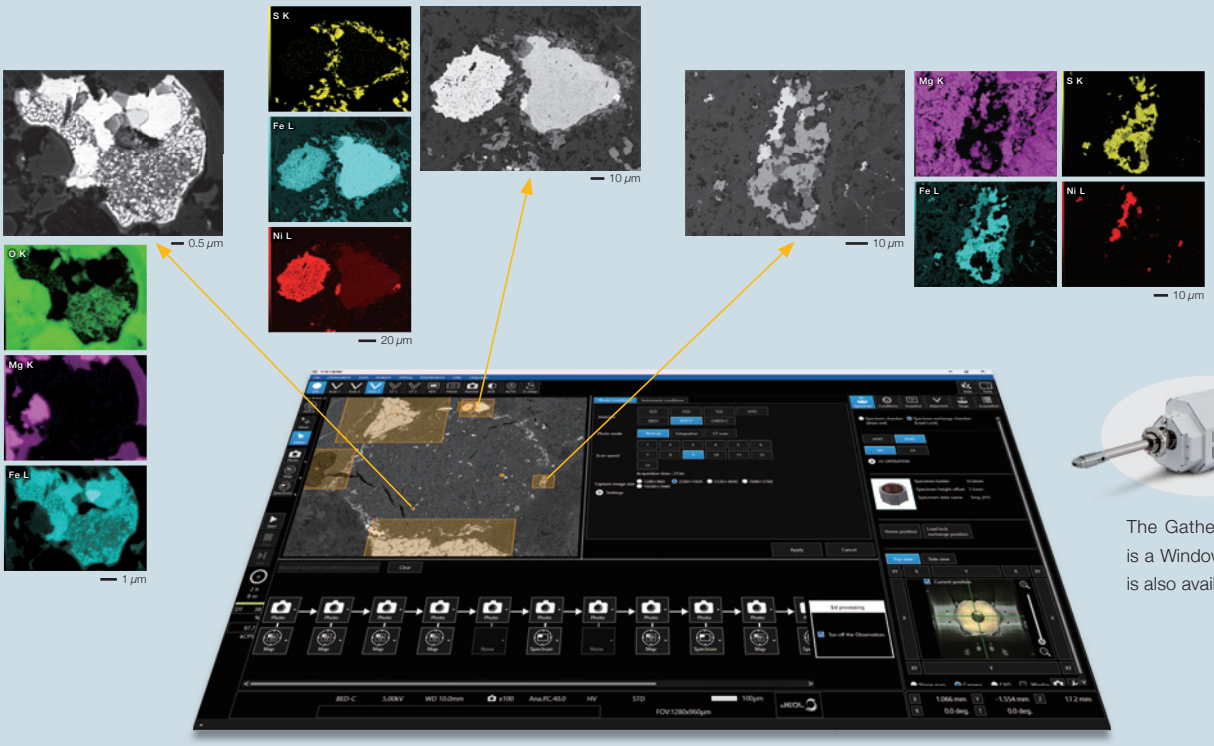

Sample: Chondrules in chondrite Julesberg (L3.6) Landing Voltage: 5 kV

The Gather-X, which is a Windowless EDS, is also available.

SEM Automatic Adjustment Package

SEM Automatic Adjustment Package (Optional): This feature uses a dedicated sample to perform magnification calibration, beam alignment, and EDS energy calibration. Regular checks ensure the equipment remains in optimal condition.

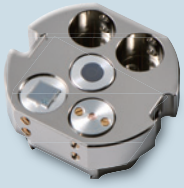

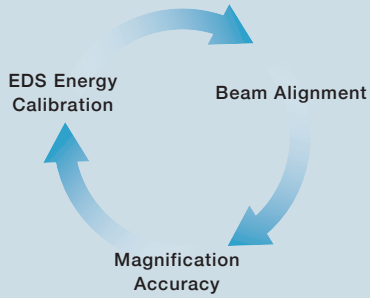

CROSS SECTION POLISHER™

IB-19540CP

COOLING CROSS SECTION POLISHER™

IB-19550CCP

– Birth of IoT CROSS SECTION POLISHER™ –

CROSS SECTION POLISHER™ (CP) is a device to prepare a cross section of a specimen for electron microscopy.Since a cross section is prepared with an ion beam, it is possible to obtain a good quality cross section in a shorter time without individual differences, compared to other methods such as polishing, which requires experience.Incorporating the new GUI and Internet of Things (IoT), operation and monitoring of milling process has become more user-friendly with the IB-19540CP/IB-19550CCP. High throughput ion source and high throughput cooling system enable rapid and smooth cross section preparation.

New GUI and Internet of Things (IoT) ~user-friendly and remote control enabled~

Incorporation of a new GUI makes the operation steps easy to understand. Easy setup is possible by following the flowchart on the control panel. Preset functions are available for saving and recalling process conditions tailored to specific applications or specimen types.

Connect to LAN for remote access and control through a web browser.Monitor and adjust the milling process over multiple CPs.

High throughput ion source

High throughput ion source is equipped as standard.The ion current density has been improved by optimizing the ion-source electrode and increasing the accelerating voltage. The standard milling rate is now 1,200 µm/h.

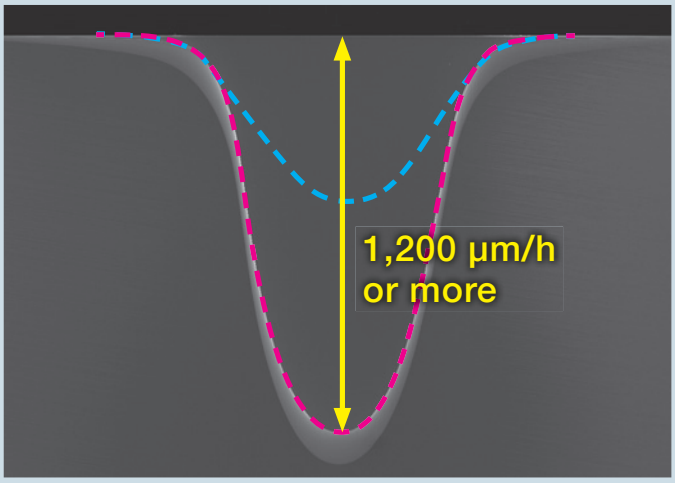

Specimen: Silicon wafer
Ion energy: 10 keV, Milling time: 1 hour

High throughput cooling system ~auto cooling and auto return to room temperature~

Cooling to return to normal temperature can be performed automatically.In addition, vacuuming around a liquid nitrogen tank is possible from the CP side to maintain cooling retention time and specimen cooling temperature.

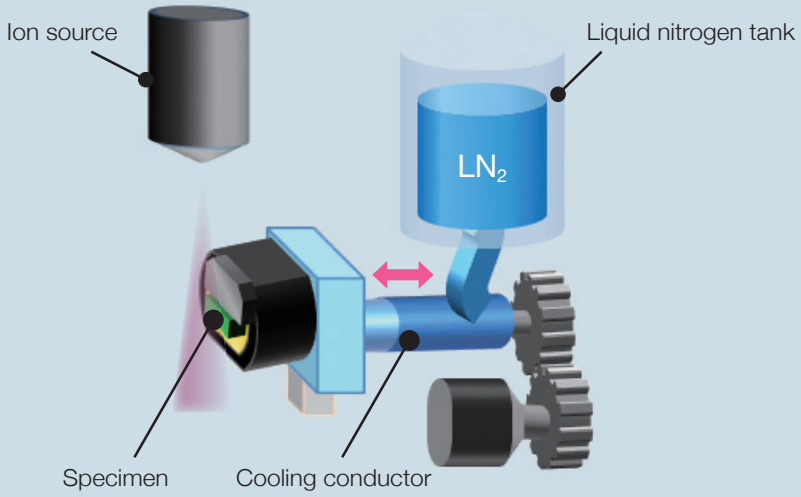

- It is possible to continuously mill for 8 hours at -120 °C
- Cooling temperature is controlled, and consumption of liquid nitrogen is reduced by repeated connection/retraction of the cooling conductor.
- Specimen exchange can be performed even when the liquid nitrogen is present.

▼ Local office

Certain products in this brochure are controlled under the "Foreign Exchange and Foreign Trade Law" of Japan in compliance with international security export control. JEOL Ltd. must provide the Japanese Government with "End-user's Statement of Assurance" and "End-use Certificate" in order to obtain the export license needed for export from Japan. If the product to be exported is in this category, the end user will be asked to fill in these certificate forms.

JEOL Ltd.

3-1-2 Musashino Akishima Tokyo 196-8558 Japan Sales Division Tel. 81-3-6262-3561 Fax. 81-3-6262-3577

www.jeol.com ISO 9001・ISO 14001 Certified

ARGENTINA
COASIN S.A.C.I.yF.
Virrey del Pino 4071,
C1430CAM-Buenos Aires
Argentina
Tel. 54-11-4552-3185
Fax. 54-11-4555-3321

AUSTRALIA & NEW ZEALAND
JEOL (AUSTRALASIA) Pty.Ltd.
Suite 1, Level 2, 18 Aquatic Drive
Frenchs Forest NSW 2086
Australia
Tel. 61-2-9451-3855
Fax. 61-2-9451-3822

AUSTRIA
JEOL (GERMANY) GmbH
Gute Aenger 30
85356 Freising, Germany
Tel. 49-8161-9845-0
Fax. 49-8161-9845-100

BANGLADESH
A.Q. CHOWDHURY SCIENCE & SYNERGY PVT. LTD.
87, Suhrwardry Avenue, Floor 2
Baridhara, Dhaka1212
Bangladesh
Tel. 880-2-2-2226-2272
Fax. 880-2-2-2226-4428

BELGIUM
JEOL (EUROPE) B.V.
Planet II, Gebouw B
Leuvensesteenweg 542,
B-1930 Zaventem
Belgium
Tel. 32-2-720-0560
Fax. 32-2-720-6134

BRAZIL
JEOL Brasil Instrumentos Cientificos Ltda.
Av. Jabaquara, 2958 5° andar conjunto 52
04046-500 Sao Paulo, SP
Brazil
Tel. 55-11-5070-4000
Fax. 55-11-5070-4010

CANADA
JEOL CANADA, INC.
3275 1ere Rue, Local #8
St-Hubert, QC J3Y-8Y6, Canada
Tel. 1-450-766-1885
Fax. 1-450-766-1887

CHINA
JEOL (BEIJING) CO., LTD.
Zhongkeziyuan Building South Tower 2F,
Zhongguancun Nansanjie Street No. 6,
Haidian District, Beijing 100190, P.R.China
Tel. 86-10-6804-6321/6322/6323
Fax. 86-10-6804-6324

JEOL (BEIJING) CO., LTD., SHANGHAI BRANCH
2F-BC Room, Building A, Mingji Business Plaza,
No.207 Songhong Road, Changning District,
Shanghai 200335, P.R.China
Tel. 86-21-6248-4487
Tel. 86-21-5836-6350
Fax. 86-21-5836-3668

JEOL (BEIJING) CO., LTD., GUANGZHOU BRANCH
Rm.3501, OnelinkCenter, 230 Tianhe Road, Tianhe District,
Guangzhou, Guangdong Prov., 510620, China
Tel. 86-20-8778-7848
Fax. 86-21-8778-4268

JEOL (BEIJING) CO., LTD., WUHAN BRANCH
R1104, Chicony Center, No.10 Luoyu Road,
Hongshan District, Wuhan, 430070, P.R.China
Tel. 86-27-8713-2567
Fax. 86-27-8713-2567

JEOL LTD. (BEIJING) CO., LTD., CHENGDU BRANCH
1807A Zongfu Building,
NO. 35 Zhongfu Road, Chengdu, Sichuan, 610016
P.R. China
Tel. 86-28-8662-2554
Fax. 86-28-8662-2564

EGYPT
JEOL SERVICE BUREAU
3rd Fl. Nile Center Bldg., Nawal Street,
Dokki, (Cairo), Egypt
Tel. 20-2-3335-7220
Fax. 20-2-3338-4186

FRANCE
JEOL (EUROPE) SAS
Espace Claude Monet, 1 Allee de Giverny
78290, Croissy-sur-Seine, France
Tel. 33-13015-3737
Fax. 33-13015-3717

GERMANY
JEOL (GERMANY) GmbH
Gute Aenger 30
85356 Freising, Germany
Tel. 49-8161-9845-0
Fax. 49-8161-9845-100

UNITED KINGDOM (UK)
JEOL(U.K.)LTD.
Silver Court, Watchmead,
Welwyn Garden City, Hertfordshire AL7 1LT, UK
Tel. 44-1707-37-7117
Fax. 44-1707-37-3254

GREECE
N. ASTERIADIS S.A.
56-58,S. Trikoupi Str. P.O. Box 26140
GR-10022, Athens, Greece
Tel. 30-1-823-5383
Fax. 30-1-823-9567

HONG KONG
FARMING LTD.
Unit No. 1009, 10/F., Prosperity
Millennia Plaza, 663 King's Road, North Point, Hong Kong
Tel. 852-2815-7299
Fax. 852-2581-4635

TechMax (Hong Kong) Company Limited
Sales & Service (NMR/ESR/MS)
16/F, 700 Nathan Road,
Mongkok, Kowloon, Hong Kong
Tel. 852-3960-7016
Fax. 852-3102-2805

INDIA
JEOL INDIA PVT. LTD.
Unit No.305, 3rd Floor,
ABW Elegance Tower,
Jasola District Centre,
New Delhi 110 025, India
Tel. 91-11-4595-8000/8005/8017

JEOL INDIA PVT. LTD. Mumbai Office
Business Suite No. S31,S32, S33
Vatika Business Centre - Unit No. G5, Ground Floor and
Unit No. 02, First Floor
Trade Centre, Bandra Kurla Complex
Bandra (East), Mumbai - 400051, INDIA
Tel. 91-76-6697-7120

JEOL INDIA PVT. LTD. Bangalore Office
Unit No.228, Regus Supreme(Jayanagar),
Supreme Overseas Exports Bldg.
44/1, 1st.& 2nd. Floor, 16th cross Jayanager 7th block(west)
KR Road, Bangalore - 560070, India
Tel. 91-93-6326-5633

JEOL INDIA PVT. LTD. Chennai Office
Door No.923, 9th Floor, Regus Olympia Platina
Plot No.33-B, South Phase, Guindy Industrial Estate,
Chennai - 600032, India
Tel. 91-99-4009-7547

JEOL INDIA PVT. LTD. Kolkata Office
Office Number (CM DALHOUSIE)
Regus, PS Arcadia, 9th Floor, 4A, Camac Street,
Abanindra Nath Thakur
Sarani, Kolkata, West Bengal- 700016, India
Tel. 91-98-3023-0484

JEOL INDIA PVT. LTD. Hyderabad Office
433, Regus Solitaire Business Centre.
1-10-39 to 44, Level 4,
Gumidelli Towers, Old Airport Road,
Begumpet, Hyderabad - 500016, India
Tel. 91-97-4111-5885

INDONESIA
PT. TEKNOLABindo Penta Perkasa
Komplek Gading Bukit Indah Blok I/11
Jl. Bukit Gading Raya Kelapa Gading Permai,
Jakarta 14240, Indonesia
Tel. 62-21-4584-7057/7058
Fax. 62-21-4584-2729

ITALY
JEOL (ITALIA) S.p.A.
Palazzo Pacinotti - Milano 3 City,
Via Ludovico il Moro, 6/A
20079 Basiglio(MI), Italy
Tel. 39-02-904-1431
Fax. 39-02-9041-4343

KOREA
JEOL KOREA LTD.
AJ Bldg. 6F,
9, Jeongui-ro 8-gil, Songpa-gu, Seoul,
5836, Korea
Tel. 82-2-511-5501
Fax. 82-2-511-2635

KUWAIT
Ashraf & CO. Ltd.
Block 2 Bldg #277, Ardiya Industrial Area,
P.O. Box 3555 13036 Safat, Kuwait
Tel. 965-2209-0750

MALAYSIA
JEOL (MALAYSIA) SDN.BHD.
508, Block A, Level 5,
Kelana Business Center,
97, Jalan SS 7/2, Kelana Jaya,
47301 Petaling Jaya, Selangor, Malaysia
Tel. 60-3-7492-7722
Fax. 60-3-7492-7723

MEXICO
JEOL DE MEXICO S.A. DE C.V.
Arkansas 11 Piso 2
Colonia Napoles
Delegacion Benito Juarez, C.P. 03810
Mexico D.F., Mexico
Tel. 52-55-5448-5900
Fax. 52-55-5211-0720

UNITED ARAB EMIRATES (UAE)
JEOL GULF FZCO
P.O. Box No. 371107
Dubai Airport Free Trade Zone West Wing 5WA No. G12,
Dubai, UAE
Tel. 971-4-609-1497
Fax. 971-4-609-1498

PAKISTAN
ANALYTICAL MEASURING SYSTEM (PVT) LTD. (AMS LTD.)
14-C Main Sehar Commercial Avenue Lane 4,
Khayaban-e-Sehar,
D.H.A-VII, Karachi-75500, Pakistan
Tel. 92-21-3534-5581/0747
Fax. 92-21-3534-5582

PANAMA
PROMED S.A.
Parque Industrial Costa del Este
Urbanizacion Costa del Este
Apartado 0816-01755, Panama
Tel. 507-303-3100
Fax. 507-303-3115

PHILIPPINES
JATEC Philippines Corporation
28 Floor, The Enterprise Center Tower 2,
Ayala Avenue corner Paseo de Roxas,
Brgy. San Lorenzo, Makati City, 1226, Philippines
Tel. 63-2-8849-3904

PORTUGAL
Izasa Portugal Lda.
Av. do Forte N6 Piso 3, Sala 2.24,
2790-072 Carnaxide, Portugal
Tel. 351-21-424-73-00
Fax. 351-21-418-60-20

QATAR
Mannai Trading Company W.L.L.
ALI Emadi Complex,
Salwa Road P.O.Box 76, Doha, Qatar
Tel. 974-4455-8216
Fax. 974-4455-8214

RUSSIA
JEOL (RUS) LLC
Office 351, floor 3, 23,
Novoslobodskaya St,
Moscow 127055, Russia
Tel. 7-495-748-7791/7792
Fax. 7-495-748-7793

SAUDI ARABIA
ABDULREHMAN ALGOSAIBI G.T.C. (Riyadh)
Algosaibi Building-Old Airport Road
P.O. Box 215, Riyadh-11411, Saudi Arabia
Tel. 966-11-272-6999
Fax. 966-1-477-1374

SWEDEN
JEOL (Nordic) AB
Hammarbacken 6A, SE-19127 Sollentuna
Sweden
Tel. 46-8-28-2800
Fax. 46-8-29-1647

SINGAPORE
JEOL ASIA PTE.LTD.
2 Corporation Road
#01-12 Corporation Place
618494, Singapore
Tel. 65-6565-9989
Fax. 65-6565-7552

SOUTH AFRICA
ANGSTROM Scientific (Pty) Ltd.
370 Angus Crescent, Northlands Business Park
29 Newmarket Road
Northriding, Randburg 2169, South Africa
Tel. 27-11-462-1347

SPAIN
IZASA, S.A.
ARAGONESES, 13, Alcobendas Poligono Industrial
28108 Alcobendas(Madrid), Spain
Tel. 34-91-663-0500
Fax. 34-91-663-0545

SWITZERLAND
JEOL (GERMANY) GmbH
Tödistrasse 60
8002 Zürich
Schweiz
Tel. 41-4428-36124
Fax. 41-4428-36123

TAIWAN
JIE DONG CO., LTD.
7F, 112, Chung Hsiao East Road,
Section 1, Taipei 10023, Taiwan
Tel. 886-2-2395-2978
Fax. 886-2-2322-4655

For NMR & Mass Spectrometer Products:
TechMax Technical Co., Ltd.
17F., No. 216, Sec. 3, New Taipei Blvd., Xinzhuang Dist.,
New Taipei City 242032, Taiwan
Tel. 886-2-8990-1779
Fax. 886-2-8990-2559

For Semiconductor Products:
JEOL TAIWAN SEMICONDUCTORS LTD.
No.198, Xingong 2nd Rd., Zhubei City,
Hsinchu County 302004, Taiwan
Tel. 886-3-571-5656
Fax. 886-3-571-5151

THAILAND
BECTHAI BANGKOK EQUIPMENT and CHEMICAL CO., Ltd.
99/9 Moo 2, Maha Sawat, Putthamonthon, Nakhon Pathom, 73170
Thailand
Tel. 66-3424-5299
Fax. 66-3424-5250

JEOL ASIA(THAILAND)CO., LTD.
87/2 CRC Tower All Seasons Place,
36 Floor, Room 31,
Wireless Road, Lumpini,
Phathumwan, Bangkok 10330
Thailand
Tel. 66-2-625-3102/3103

THE NETHERLANDS
JEOL (EUROPE) B.V.
Lireweg 4, NL-2153 PH Nieuw-Vennep,
The Netherlands
Tel. 31-252-623-500
Fax. 31-252-623-501

TURKEY
KARFO Endustriyel
Yukan Dudullu, Karfo Plaza, Şerifali Mah, Beyan Sokağı No:23,
34775 İstanbul, Turkey
Tel. 90-216-660-0315

META Analitik
Atatürk Mah. Meriç Cad. Turkuaz Plaza No:5/38 Ataşehir,
34758 Istanbul, Turkey
Tel. 90-216-580-8020

UNITED STATES OF AMERICA (USA)
JEOL USA, INC.
11 Dearborn Road, Peabody, MA 01960, USA
Tel. 1-978-535-5900
Fax. 1-978-536-2205/2206

JEOL USA, INC. WEST OFFICE
5653 Stoneridge Drive Suite #110
Pleasanton, CA 94588, USA
Tel. 1-925-737-1740
Fax. 1-925-737-1749

VENEZUELA
GOMSA Service and Supply C.A.
Urbanizacion Montalban III
Residencias Don Andres - Piso 7 - Apartomento 74
Avenida 3, entre calles 7 y 6
Montalban, Caracas, Venezuela
Tel. 58-212-443-4342
Fax. 58-212-443-4342

VIETNAM
T&N Trading and Investment Company Limited
19 Hang Thiec, Hang Gai Ward, Hoan Kiem District,
Hanoi, Vietnam
Tel. 84-98202-8728

(Ser. No. 143)

No. 9301E542C Printed in Japan, Kp